学位論文

Precision spectroscopy of deeply bound pionic states in ^{121,116}Sn

(^{121,116}Sn 中におけるπ中間子の深い束縛状態の精密分光)

平成 27年 10月 博士 (理学) 申請

東京大学大学院理学系研究科
物理学専攻

西　隆博

Abstract

An established approach for quantitative evaluation of the chiral symmetry breaking in finite density is study of pion-nucleus interaction through the experimental measurement of pionic atoms. Theories predict strength of isovector interaction between pion and nucleus, represented by a parameter b_1, is enhanced by nuclear medium effects of the strong interaction, which is related to the partial restoration of the chiral symmetry breaking. So far the value of b_1 at finite density was measured at GSI, Germany, through the spectroscopy of deeply-bound pionic atoms. From the comparison with the b_1 in vacuum, the partial restoration of chiral symmetry breaking was suggested, while the precision of the obtained b_1 is still not enough compared with that in vacuum.

For the further study of b_1, we performed precision spectroscopy of deeply bound pionic states in ^{121,116}Sn at RIKEN, RI Beam Factory in June 2014. After the fine tuning of the experimental conditions, we achieved unprecedented resolution and measured high quality excitation spectra of ^{121}Sn and ^{116}Sn near the charged pion emission threshold. In these spectra, the $1s$, $2p$ and $2s$ pionic states in ^{121,116}Sn atoms are observed. Deeply bound pionic states in a nucleus with an even mass number,^{116}Sn, are observed for the first time.

The systematic error for binding energy of $1s$ state is reduced by using $2p$ state as a reference peak in ^{121}Sn. From the obtained binding energies and width in ^{121}Sn, we evaluated optical potential parameter b_1 to be $-0.114^{+0.0049}_{-0.0045} m_\pi^{-1}$, and succeed in the most precise evaluation of b_1 in medium.

Contents

Abstract ii

Contents iii

List of Figures vii

List of Tables xi

1 Introduction 1
- 1.1 Chiral symmetry and pionic atoms . . . 1
- 1.2 Production of deeply bound pionic atoms . . . 2
  - 1.2.1 Deeply bound pionic state . . . 2
  - 1.2.2 $(d, {}^3\mathrm{He})$ reactions . . . 2
- 1.3 Experiment at GSI . . . 5
- 1.4 Pionic atom spectroscopy at RIKEN . . . 7
  - 1.4.1 Pilot experiment . . . 7
  - 1.4.2 Precision spectroscopy of pionic atoms in 2014 . . . 8
    - (i) Experimental resolution . . . 8
    - (ii) b_1 precision . . . 8
- 1.5 Expected spectra . . . 9
- 1.6 Thesis objectives and outline . . . 12

2 Experiment 13
- 2.1 Experimental overview . . . 13
- 2.2 RIKEN RI Beam Factory . . . 14
- 2.3 Beam properties . . . 15
  - 2.3.1 Intensity and beam energy . . . 16
  - 2.3.2 Emittance and momentum spread . . . 17
  - 2.3.3 Stability of the beam properties . . . 18
- 2.4 Target . . . 19
- 2.5 Spectrometer system . . . 20
  - 2.5.1 Notations of the ion optical parameters . . . 20
  - 2.5.2 Dispersion matching . . . 21
  - 2.5.3 Beam transfer line . . . 21
  - 2.5.4 Ion optics design for beam transfer line . . . 22
  - 2.5.5 Beam transfer line optimization . . . 25

2.5.6 BigRIPS . . . 26
2.5.7 Ion optics design for BigRIPS . . . 27
2.6 Detectors . . . 30
2.6.1 Low-pressure multi-wire drift chambers at F3 . . . 30
2.6.2 Multi-wire drift chambers at F5 . . . 30
2.6.3 Scintillation counter at F5 . . . 31
2.7 DAQ and trigger logic . . . 34
2.8 Run summary . . . 37

3 Data analysis **39**
3.1 Event selections for ^{3}He . . . 39
3.1.1 Time of flight between the F5 and F7 focal planes . . . 40
3.1.2 Energy loss in MWDCs at the F5 focal plane . . . 44
3.1.3 Event timing with respect to radio frequency of SRC . . . 46
3.1.4 Evaluation of contamination and efficiency of particle identification . . . 49
3.2 Tracking of ^{3}He . . . 52
3.2.1 Conversion function from drift time to drift length . . . 52
3.2.2 Fitting of particle trajectories . . . 52
3.2.3 Wire offset correction . . . 55
3.2.4 Tracking resolution . . . 56
3.2.5 Tracking efficiency . . . 58
3.2.6 Smearing of the position spectra . . . 60
3.2.7 Focal plane position and angle spectra . . . 62
3.3 Deduction of ^{3}He momenta from trajectories at F5 using transfer matrix . 63
3.3.1 $(x_{\rm F5}|a^n_{\rm F0})$, $(x_{\rm F5}|b^n_{\rm F0})$ and $(x_{\rm F5}|a_{\rm F0}b^2_{\rm F0})$ . . . 64
3.3.2 $(x_{\rm F5}|a_{\rm F0}\delta)$ and $(x_{\rm F5}|a^2_{\rm F0}\delta)$ . . . 64
3.3.3 $(x_{\rm F5}|\delta)$ and $(x_{\rm F5}|\delta^2)$ . . . 66
3.3.4 $(a_{\rm F5}|a_{\rm F0})$, $(b_{\rm F5}|b_{\rm F0})$ and an incident beam direction . . . 68
3.3.5 $(a_{\rm F5}|a_{\rm F0}\delta)$, $(b_{\rm F5}|b_{\rm F0}\delta)$ and $(b_{\rm F5}|b_{\rm F0}\delta^2)$ . . . 72
3.3.6 Summary of deduced transfer matrix . . . 72
3.4 Deduction of excitation energies . . . 73
3.4.1 Energy calibration by $p(d,{}^3\mathrm{He})\pi^0$ reaction . . . 73
3.4.2 Deduction of excitation energy . . . 74
3.5 Deduction of reaction cross section . . . 75
3.5.1 Luminosity . . . 75
3.5.2 Acceptance . . . 76
3.6 Excitation spectra of ^{121,116}Sn . . . 77
3.7 Experimental energy resolution . . . 79
3.7.1 Momentum spread and emittance of primary beam . . . 79
3.7.2 Multiple scattering at vacuum windows . . . 79
3.7.3 Reaction point distribution in the target . . . 80
3.7.4 Resolution estimation by Monte Carlo simulation . . . 80
3.7.5 Estimated experimental resolution . . . 81

4 Results and Discussion **85**
4.1 Deduction of binding energies and widths . . . 85

- 4.1.1 Fitting function . . . 86
- 4.1.2 Fitting results of ^{121}Sn excitation spectra . . . 87
- 4.1.3 Fitting results of ^{116}Sn excitation spectra . . . 89
- 4.2 Evaluation of systematic errors . . . 91
  - 4.2.1 Systematic errors of binding energies . . . 91
  - 4.2.2 Systematic errors of binding energy difference . . . 92
  - 4.2.3 Systematic errors of natural widths . . . 93
  - 4.2.4 Binding energy, natural width, and binding energy difference . . . 94
- 4.3 Deduction of formation cross section . . . 95
  - 4.3.1 Formation cross section of pionic $1s$ and $2p$ states . . . 95
  - 4.3.2 Systematic errors of double-differential cross section . . . 98
  - 4.3.3 Reaction angle dependence of pionic states . . . 99
  - 4.3.4 Relative strength of $2p$ and $2s$ states . . . 101
  - 4.3.5 Summary of the cross section analysis . . . 101
- 4.4 Deduction of optical potential parameters . . . 102
  - 4.4.1 Nuclear density distribution . . . 102
  - 4.4.2 Optical potential parameters . . . 104
  - 4.4.3 Deduction of b_1 and ImB_0 . . . 106

5 Conclusion and future outlook 109
- 5.1 Conclusion . . . 109
- 5.2 Future outlook . . . 110

A Simulation of MWDC and comb-like structures 115

B Study of simulated energy resolution 119

C Parameters for decomposition 121
- C.1 Effective number, neutron separation energy and experimental resolution of each configuration . . . 121
- C.2 Effective numbers of finite angles . . . 124

Bibliography 127

List of Figures

1.1 The density function of pionic atoms 3
1.2 Momentum transfer 4
1.3 The ^{3}He kinetic energy spectra obtained in the previous experiment at GSI 6
1.4 Theoretically calculated spectra for the formation of pionic states in ^{121}Sn 11

2.1 Schematic view of the Superconducting Ring Cyclotron (SRC) and the fragment separator BigRIPS 14
2.2 The bird's-eye view of the RIKEN-RIBF 15
2.3 The acceleration scheme 15
2.4 Relation between the count rate of the back-scattered particles at the target and beam intensity. 16
2.5 The beam profile measured at the achromatic focal plane (F3) and the dispersive focal plane (F5) 17
2.6 Attenuator 18
2.7 The measured beam envelope 19
2.8 A schematic view of the extraction and transfer beam lines from SRC to RIBF standard target position. 22
2.9 Optics of the beam transfer line 24
2.10 Color plot of x_{F0} versus δ deduced from x_{F3} and x_{F5}. 26
2.11 A schematic view of BigRIPS and the detector setup. 27
2.12 Optics of the BigRIPS 29
2.13 Schematic drawings of the detectors and their stands in the F5 chamber. . 32
2.14 A front view of sense wires in the drift chamber (top) and a top view of the X and X′ planes in the drift chamber (bottom) are displayed. 33
2.15 Schematic drawings of segmented scintillator. 34
2.16 A schematic drawing of the trigger logic 36
2.17 Trigger inefficiency evaluation 36

3.1 TDC calibration of F5 scintillators 41
3.2 Δt_{LR} and x_{F5MWDC} 42
3.3 $\mathrm{ToF}_{\mathrm{F5F7}}$ and its position dependence 42
3.4 The corrected $\mathrm{ToF}_{\mathrm{F5F7}}$ and $\Delta E_{\mathrm{SciF5}}$ 43
3.5 Time over threshold of MWDC signals 45
3.6 Number of planes detecting ^{3}He-like signals ($N^{^{3}\mathrm{He}}_{\mathrm{plane}}$) 45
3.7 A timing diagram of particles passing through the BigRIPS. 47
3.8 $\Delta t_{\mathrm{SciF5-RF}}$ and its position dependence 48
3.9 Enlarged view of $\Delta\tilde{t}_{\mathrm{SciF5-RF}}$ distribution in the production run with the ^{122}Sn target 49

3.10 Position distribution of contaminations 51
3.11 Position dependence of pID efficiency 51
3.12 (Left) The distribution of time difference between MWDC signals and the F5 scintillator signals. (Right) Conversion function from the time difference to drift length of X plane of upstream MWDC. 53
3.13 Examples of tracking by MWDC 54
3.14 Measured offset of wires in the X1 plane of the upstream MWDC 55
3.15 Residual distribution of the tracking by MWDC on X plane in upstream MWDC 56
3.16 Estimated track resolution for each MWDC plane. 57
3.17 Position (wire) dependence of the tracking resolution for the X1 plane of the upstream MWDC 58
3.18 Reduced χ^2 distribution of the fitting in a production run with ^{122}Sn target. 59
3.19 position dependence of the tracking efficiency 59
3.20 Effect of the smearing 61
3.21 The obtained position and angle spectra in a production run with the ^{122}Sn target. 62
3.22 Two dimensional plots of x_{F5} and a_{F0} in the transfer matrix measurement run using with the $^{122}(d, ^3\mathrm{He})$ reaction. 65
3.23 Spectra of the corrected x_{F5} with ^{122}Sn target in different scale of BigRIPS. 67
3.24 The fitting result for the dispersion measurement. 67
3.25 Two dimensional δ and a_{F0} plots in the experimental data and simulation with polyethylene target. 70
3.26 The χ^2 of the evaluation of beam direction and magnification (horizontal) 70
3.27 Two dimensional δ and b_{F0} plots in the experimental data and simulation with polyethylene target. 71
3.28 The χ^2 of the evaluation of beam direction and magnification (vertical) . 71
3.29 δ-reaction angle plot from the $p(d, ^3\mathrm{He})$ reaction. Left figure shows the experimental data and right figure shows the simulation data. 74
3.30 The acceptance simulated by MOCADI. 77
3.31 Excitation spectra obtained with the $^{122,117}\mathrm{Sn}(d, ^3\mathrm{He})$ reaction 78
3.32 The histogram of $E_{\mathrm{ex}} - E_{\mathrm{ex}}^{\mathrm{input}}$ 82
3.33 Experimental resolution deduced by Monte Carlo simulation 82
3.34 Experimental resolution in different conditions 83

4.1 Excitation spectrum of ^{121,116}Sn and the fitting results. 90
4.2 Excitation spectrum of ^{121}Sn and the fitting results for the different reaction angles. 96
4.3 Excitation spectrum of ^{116}Sn and the fitting results for the different reaction angles. 97
4.4 Reaction angle dependence of the differential formation cross sections of pionic states. 100
4.5 One σ contour plots of the fitting result of b_1 and ImB_0. 107

A.1 Contour plot of drift time and length, and histogram of estimated drift length in simulation. 116
A.2 Reconstructed position histogram on the first plane and estimated drift length in 3 regions. 117

B.1 The dependencies of three variables, total $1s$ peak width, the experimental resolution and the deduced $1s$ ntural widths, on the angular ranges of the analyzed data for two scaling factors of the central momenta of the spectrometer. 120

List of Tables

1.1 Binding energies and widths of pionic 1*s* states measured in the experiment at GSI. 5
1.2 Specification of GSI and RIKEN RIBF 7
1.3 Result of pilot experiments at RIKEN 8
1.4 Optical potential parameters used in the calculation 9
1.5 Theoretically calculated binding energies and widths of pionic states in ^{121,116}Sn. 9

2.1 Target list 19
2.2 Specifications of dipoles in beam transfer line. 22
2.3 Specifications of dipoles in BigRIPS. 27
2.4 Specification of quadrupoles in BigRIPS. 27
2.5 Run summary of the experiment 37

3.1 Optical transfer matrix elements 73
3.2 Summary of the factors for the cross section determination. The pID efficiency is evaluated for each position as shown in Fig. 3.19. The position dependence is also taken into account. 77

4.1 N^*_{eff} and separation energy of each neutron hole state in the contribution of 1*s* pionic states. 88
4.2 Fitting result of ^{121}Sn excitation energy spectrum in $0° < \theta < 1.5°$. 88
4.3 Fitting result of ^{116}Sn excitation energy spectrum in $0° < \theta < 1.5°$. 89
4.4 The systematic errors of binding energies of pionic states from transfer matrix elements. 93
4.5 The systematic errors of natural widths of pionic states in ^{121}Sn from uncertainties of the transfer matrix elements. 94
4.6 Summary of deduced energies, energy differences and natural widths of pionic ^{121,116}Sn. 95
4.7 Experimentally deduced differential cross sections for different reaction angle regions. 97
4.8 The systematic errors on differential cross sections from uncertainties of transfer matrix elements. 98
4.9 Experimentally deduced relative magnitudes of the differential cross sections of 2*p* and 2*s* pionic states to that of the 1*s* state for each target. . . 101
4.10 Theoretically calculated relative magnitudes of the differential cross sections of 2*p* and 2*s* pionic states to that of the 1*s* state for each target. . . 101
4.11 Radial parameters of ^{121}Sn for 2-parameter Fermi distribution. 103
4.12 The parameters in non-local part of the optical potential 104

4.13 The parameters in local part of the optical potential for pion-nucleus interaction. . . . 105
4.14 Errors of experimental values utilized for the deduction of b_1 and ImB_0. . 106
4.15 Deduced b_1 and ImB_0 in this experiment and in the preceding experiment 107

C.1 Effective number, neutron separation energy and experimental resolution of each configuration in ^{121}Sn. . . . 122
C.2 Effective number, neutron separation energy and experimental resolution of each configuration in ^{116}Sn. . . . 123
C.3 Effective number of each reaction angle and each configuration in ^{121}Sn. . 124
C.4 Effective number of each reaction angle and each configuration in ^{116}Sn. . 125

Chapter 1

Introduction

1.1 Chiral symmetry and pionic atoms

One of the most important concepts in understanding the low energy Quantum ChromoDynamics (QCD) is "chiral symmetry breaking". Spontaneous break-down of the chiral symmetry is known to be an under-lying mechanism for hadrons to acquire their masses dynamically. The chiral symmetry is expected to be partially restored in a high temperature and/or high density condition [1, 2]. The experimental evaluation of the partial restoration of chiral symmetry breaking is one of the most important subjects in modern hadron physics.

An established approach for quantitative evaluation of the chiral symmetry breaking in finite density is a study of pion-nucleus interaction through the experimental measurement of pion-nucleus bound systems, pionic atoms. Theories predict strength of isovector interaction between pion and nucleus, represented by a parameter b_1, is enhanced by nuclear medium effects of the strong interaction, which is related to the partial restoration of the chiral symmetry breaking [3–5].

The pion nucleus interaction is formulated in an optical potential of a conventional Ericson-Ericson type, and the parameter b_1 appears in the local part. The local part uses three parameters, isoscalar (b_0), isovector (b_1) and a complex parameter mainly describing the nuclear absorption (B_0) and is expressed as

$$V_s(r) = -\frac{2\pi}{\mu}[\epsilon_1\{b_0\rho(r) + b_1\delta\rho(r)\} + \epsilon_2 B_0\rho(r)^2], \tag{1.1}$$

where r denotes radius measured from the center of the nucleus, ρ nuclear density distributions, $\delta\rho$ density difference between neutron and proton distributions, μ the reduced mass of π and the nucleus. The symbols ϵ_1 and ϵ_2 are $1 + m_\pi/M_{\text{nucleon}}$ and $m_\pi/2M_{\text{nucleon}}$, respectively.

Experimentally, the b_1 parameter in vacuum is deduced from X-ray spectroscopy of $1s$ states of pionic hydrogen and deuterium [6–8] to be $b_1 = -(0.0868 \pm 0.0014)\ m_\pi^{-1}$. To evaluate the partial restoration of chiral symmetry breaking in finite density precisely, deduction of b_1 in medium and comparison with that in vacuum is essential.

1.2 Production of deeply bound pionic atoms

1.2.1 Deeply bound pionic state

In order to obtain the b_1 in medium, it is important to make spectroscopy of pionic atoms with a large overlap between the pionic orbitals and the nuclear densities to probe the effect in the finite density. However, it is known that the atomic cascade processes of pionic atoms terminate at certain orbitals known as “last orbits” where the nuclear absorption takes over the cascade. Pionic bound states in lower orbitals such as $1s$ or $2p$ in relatively heavy nuclei are known as “deeply bound pionic states” and are hidden and not produced in the cascade process.

Existence of such deeply bound states in heavy nuclei was pointed out by Friedman and Soff [9] in 1985 and by Toki and Yamazaki [10] in 1988. They predicted that the bound states exist as quasi-stable states because the repulsive pion-nucleus optical potential pushes the pionic wave function outward and the nuclear absorption for the bound pions is weakened. As a result, the deeply bound pion was expected to be localized in the surface of the nuclei. As shown in Fig. 1.1, the pion wave function in such state has a large overlap with the nuclear wave function.

1.2.2 $(d, {}^3\text{He})$ reactions

To produce deeply bound pionic atoms, a new method was suggested by Toki and Yamazaki [10] in 1988. The suggested method uses charge-exchange pion-transfer reactions, which produce the pion directly in the deep atomic orbits. In the reaction, a deuteron picks up a neutron in a target, and at the same time a π^- is transferred to the target nucleus producing pionic atoms. A ^{3}He is emitted in the reaction with the kinetic energy reflecting the pion binding energy and the separation energy of the picked-up neutron. From measurement of the momentum of the ^{3}He, we can obtain the information of the deeply bound pionic states.

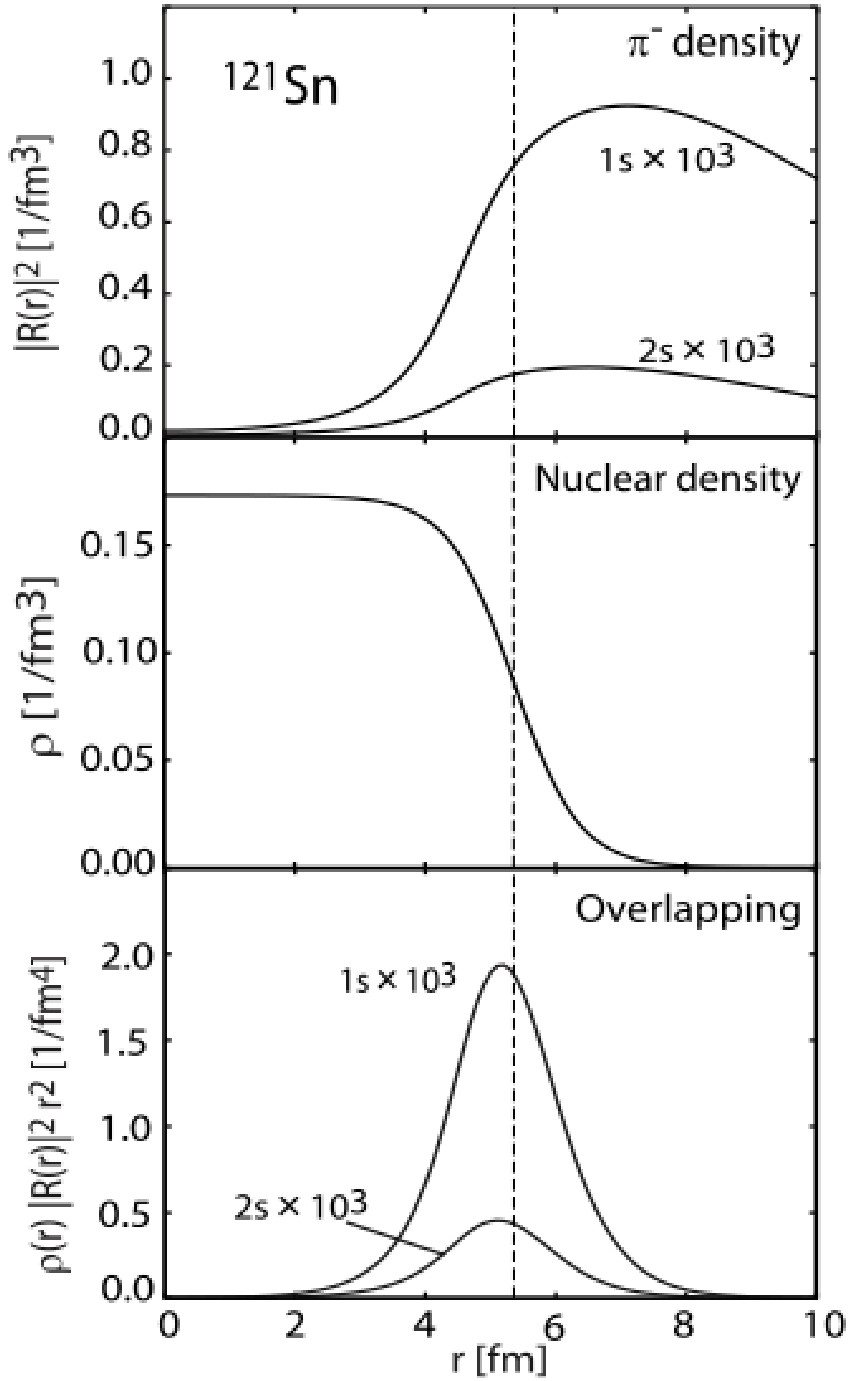

FIGURE 1.1: The density function of pions (Top), nuclear (Middle) and their overlap (Bottom) as a function of the distance from the center of the nucleus, r in pionic ^{121}Sn. The dashed line represents the half density radius of the nuclear distribution. The figure is taken from Ref. [11]

In order to enhance the formation cross section of the pionic atoms, the relative momentum between the produced pion and the recoiled target must be small. The beam energy is chosen to be $\simeq$ 500 MeV, to realize the recoilless condition where the momentum transfer q becomes zero. Figure 1.2 shows the relation between the primary beam energy and the momentum transfer for Q value $= -141.5$ MeV in ^{121}Sn $(d, {}^{3}\mathrm{He})$ reaction with reaction angles of 0°, 1°, 2° and 3°.

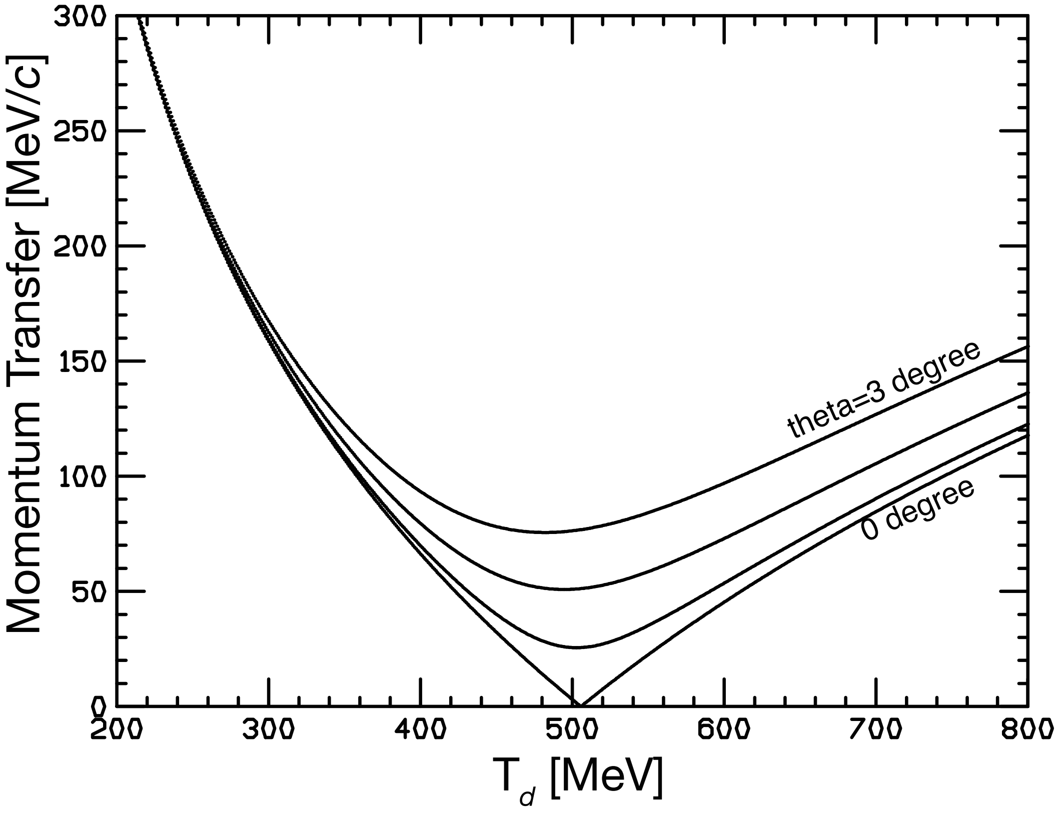

Figure 1.2: Momentum transfer of ^{121}Sn $(d, {}^{3}\mathrm{He})$ reaction as a function of deuteron kinetic energy, Td. Each solid line corresponds to the reaction angle of 0°, 1°, 2° and 3°, respectively.

Another benefit of the small momentum transfer is a resultant small angular momentum transfer in the reaction. Quasi-substitutional configurations such as $(1s)_{\pi^-} \otimes (3s_{1/2})_n^{-1}$ (the neutron in $3s_{1/2}$ is picked up and pion in $1s$ atomic orbit is produced) are populated selectively. Therefore the recoilless condition is important to determine the binding energy and width of pionic $1s$ bound state, which is most sensitive to the strong interaction.

1.3 Experiment at GSI

In 1996, a deeply bound pionic state was discovered [12–14], as the pionic $2p$ state in ^{207}Pb atom by using the ^{208}Pb$(d, ^3$He) reaction at GSI, Germany. In 1998, they also observed the $1s$ and $2p$ states in ^{205}Pb [15, 16].

As a natural continuation, spectroscopy of pionic states in ^{115,119,123}Sn was performed to investigate the isotope dependence of pionic binding energies and widths [17]. Figure 1.3 shows the obtained spectra in the experiment. In the figure the peak at the center of each spectrum corresponds to the pion in $1s$ atomic orbit and the right peak corresponds to the energy calibration by $p(d,^3\mathrm{He})\pi^0$ reaction. They determined the binding energies and widths of $1s$ states in ^{115,119,123}Sn as Table 1.1, and derived the optical potential parameters by simultaneous fitting of the binding energies and widths together with those of symmetric light nuclei, ^{16}O, ^{20}Ne and ^{28}Si. The obtained value of b_1 is $-(0.115 \pm 0.007)\ m_\pi^{-1}$, which shows more than 3 σ deviation from that in vacuum, $-(0.0868 \pm 0.0014) m_\pi^{-1}$. This deviation suggests partial restoration of the chiral symmetry at finite density.

However, the evaluated value in medium still has large errors compared with that in vacuum. The error of b_1 is in principle propagated from the error of binding energies. To improve the precision of b_1, we need to determine the binding energies of $1s$ states more precisely. Whereas further improvements of the precision is not easily expected in GSI. Within realistic conditions, significant statistical improvement requires a higher intensity beam or a larger thickness of the target. In the preceding experiments, the employed primary beam intensity of 10^{11}/spill was nearly the same as the maximum intensity of the accelerator, and deterioration of the resolution does not allow a thicker target.

pionic states $(nl)_\pi$ in ^{A}Sn	B_{nl} [MeV]	Γ_{nl} [MeV]
$1s$ in ^{115}Sn	3.906 ± 0.021(stat.)± 0.012(sys.)	0.441 ± 0.068(stat.)± 0.054(sys.)
$1s$ in ^{119}Sn	3.820 ± 0.013(stat.)± 0.012(sys.)	0.326 ± 0.047(stat.)± 0.065(sys.)
$1s$ in ^{123}Sn	3.744 ± 0.013(stat.)± 0.012(sys.)	0.341 ± 0.036(stat.)± 0.063(sys.)

Table 1.1: Binding energies and widths of pionic $1s$ states in Sn isotopes measured in the experiment at GSI [17].

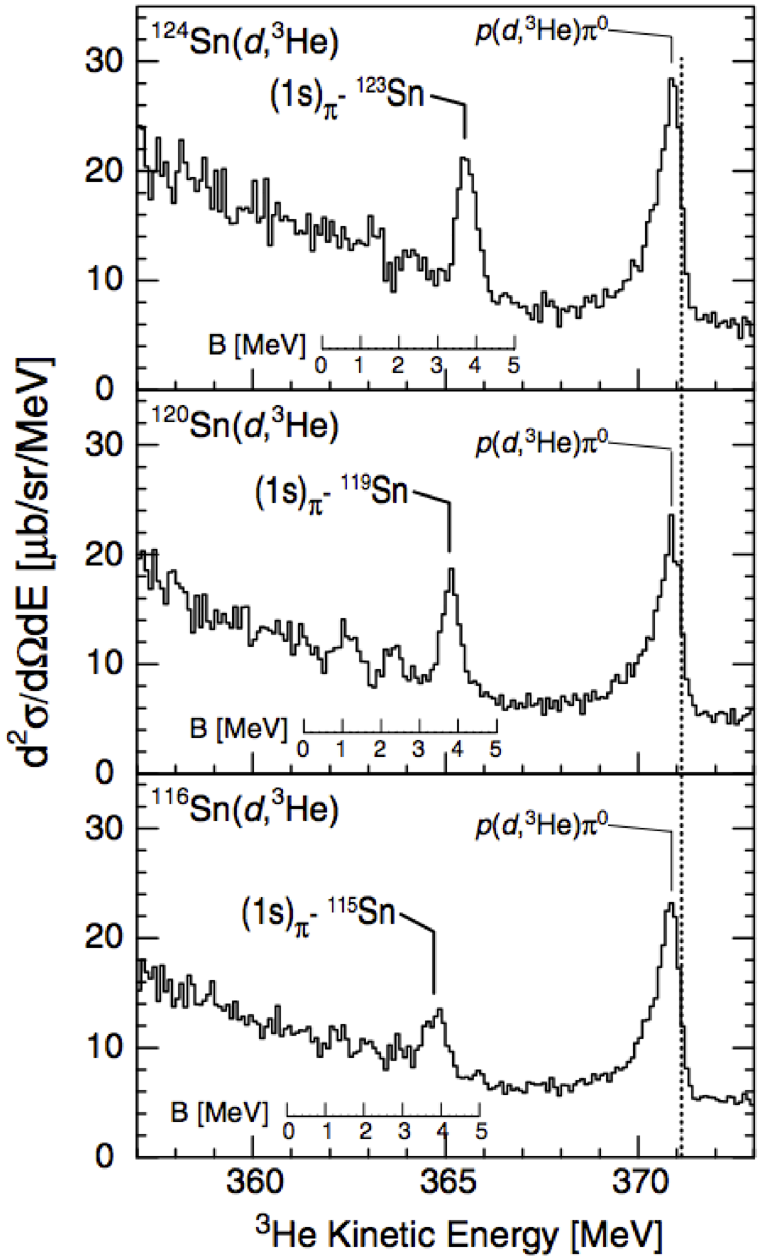

FIGURE 1.3: The ^{3}He kinetic energy spectra obtained in the experiment at GSI [17].

1.4 Pionic atom spectroscopy at RIKEN

We designed an experimental project to measure deeply bound pionic atoms systematically at a new facility, RI beam factory (RIBF), RIKEN [18]. We aim at measuring pionic atoms with a spectral resolution comparable or better than the $1s$ natural width of about 300 keV and at determining b_1 value for each pionic atom with comparable precision to that in GSI, an error level of $\pm 0.007\ m_\pi^{-1}$.

In the facility two key components are available, namely a high intensity (a few 100 pnA) deuteron beam with the kinetic energy of 500 MeV and a fragment separator BigRIPS, which is used as a high-resolution and large-angular-acceptance spectrometer. Table 1.2 compares facility specifications of GSI and RIKEN RIBF. As shown, beam intensity is effectively about 60 times larger in RIKEN than that in GSI[1] and the angular acceptance by about 8 times. This substantially larger intensity per unit time and the larger coverage of the acceptance open various new opportunities.

In the meantime, the intrinsic momentum spread is larger than that in GSI. Thus, we need to develop an ion optical setting using a dispersion matching method to suppress the contribution of the intrinsic beam momentum spread to the spectral resolution, which is explained in Sect. 2.5.

Specification	GSI	RIKEN
Beam Intensity	10^{11} particles/(cycle=6 s)	10^{12} particles/second
Angular acceptance (horizontal × vertical)	10 mrad × 10 mrad	20 mrad × 40 mrad
intrinsic momentum spread of primary beam	0.03 % (FWHM)	0.1 % (FWHM)

Table 1.2: Specification of GSI and RIKEN RIBF

1.4.1 Pilot experiment

In 2010, we have carried out a pilot experiment in RIBF with an allocated beamtime of about 3 days. The goal was to make an overall test of the measurement, that is the beam, the spectrometer system, the detectors, the DAQ, and the analysis, for identification of potential problems. We employed a ^{122}Sn target to accomplish a first observation of pionic ^{121}Sn atoms.

Major achievements in the experiment are (i) first observation of pionic ^{121}Sn atoms and (ii) first observation of angular dependence of the pionic atom formation cross section of the $(d, {}^3\text{He})$ reaction. The obtained binding energies and widths of the $1s$ and $2p$ states are summarized in Table 1.3. These remarkable achievements are revealing the potential capabilities of the experimental setup in view of the pionic atom spectroscopy [19].

---

[1] The main accelerator at GSI is a synchrotron, and the spill cycle is about 6 second.

In the meantime, we found the estimated experimental resolution to be about 500 keV (FWHM) which is worse than above targeted resolution of 300 keV and very severe optical aberration effects in the spectrometer system which did not allow us to deduce a meaningful b_1 value from the measurement.

pionic states $(nl)_\pi$ in ${}^A\text{Sn}$	B_{nl} [MeV]	Γ_{nl} [MeV]
$1s$ in ${}^{121}\text{Sn}$	$3.853 \pm 0.013(\text{stat.})^{+0.035}_{-0.046}(\text{sys.})$	$0.363 \pm 0.033(\text{stat.})^{+0.109}_{-0.111}(\text{sys.})$
$2p$ in ${}^{121}\text{Sn}$	$2.345 \pm 0.023(\text{stat.})^{+0.046}_{-0.051}(\text{sys.})$	—

Table 1.3: Result of pilot experiments at RIKEN

1.4.2 Precision spectroscopy of pionic atoms in 2014

Based on the analysis result of the pilot experiment, we set goals of the present experiment to (i) an experimental resolution of about 300 keV (FWHM) and (ii) deduction of b_1 at an error level of ± 0.007 m_π^{-1}. We employed the same target of ${}^{122}\text{Sn}$ and performed a precision spectroscopy in 2014 with an allocated beamtime of about 7 days. An additional target of ${}^{117}\text{Sn}$ was also prepared to make a test study using an odd-neutron-number target.

(i) Experimental resolution

The pilot experiment revealed that the resolution contribution was dominated by the emittance and the momentum spread of the primary beam and the incompleteness of beam line optics before the target. For the improvement, we optimized conditions in the accelerators and reduced the emittance and the momentum spread of the primary beam (Sect. 2.3) and tuned the beam line optics before the target in newly developed procedures (Sect. 2.5.5).

(ii) b_1 precision

We aimed at measuring two pionic states simultaneously in order to deduce the difference of the binding energies precisely. Taking difference will suppress ambiguities arising from the determination of the absolute energies. Especially, the uncertainties arising from the absolute beam energy ambiguities and calibration peak position determination will be largely suppressed. Also fluctuations of the spectrometer system commonly influencing over the spectra will also be suppressed. We took a data set for precision measurement of the ion optical aberration effects, evaluated them, and compensated for them (Sect. 3.3).

1.5 Expected spectra

The expected spectrum in the ^{122}Sn $(d, {}^{3}\mathrm{He})$ reaction is theoretically calculated [20]. In the calculation, the binding energies, widths, and wave functions of pionic states are obtained by solving the Klein-Gordon equation with using the optical parameters tabulated in Table 1.4 taken from Ref. [21]. The results are summarized in Table 1.5. The formation cross section is calculated based on an effective number approach with an Eikonal approximation. The effective neutron numbers for configurations of pions and neutron holes are estimated by integrating the overlap functions between the pion wave functions and the neutron wave functions in the target nuclei as described in detail in Ref. [20].

b_0	$-0.0283\ m_\pi^{-1}$
b_1	$-0.12\ m_\pi^{-1}$
$\mathrm{Re}B_0$	$0.0\ m_\pi^{-4}$
$\mathrm{Im}B_0$	$0.042\ m_\pi^{-4}$
c_0	$0.223\ m_\pi^{-3}$
c_1	$0.25\ m_\pi^{-3}$
$\mathrm{Re}C_0$	$0.0\ m_\pi^{-6}$
$\mathrm{Im}C_0$	$0.010\ m_\pi^{-6}$
ξ	1.0

TABLE 1.4: Optical potential parameters used in the calculation [20, 21]. The detail of these parameters are explained in Sect. 4.4.2.

	^{116}Sn	^{121}Sn
B_{1s} [MeV]	3.884	3.787
B_{2p} [MeV]	2.277	2.257
B_{2s} [MeV]	1.432	1.409
B_{3p} [MeV]	1.019	1.012
B_{3s} [MeV]	0.739	0.730
Γ_{1s} [MeV]	0.357	0.306
Γ_{2p} [MeV]	0.123	0.110
Γ_{2s} [MeV]	0.092	0.078
Γ_{3p} [MeV]	0.042	0.038
Γ_{3s} [MeV]	0.036	0.030

TABLE 1.5: Theoretically calculated binding energies and widths of pionic states in ^{121,116}Sn.

The calculated spectra are shown in Fig. 1.4. The figures show theoretically calculated spectra of $^{122}\mathrm{Sn}(d, {}^3\mathrm{He})$ reaction [20] with reaction angle = 0 (Top) and finite reaction angles (Bottom). The experimental resolution is assumed to be 300 keV (FWHM).

As indicated in the top panel, the peak structures are composed of coupled configurations of pionic states and neutron hole states as $(nl)_{\pi^-} \otimes (j_n)_n^{-1}$. The contribution of quasi-free π^- and π^0 are also indicated in the figure. The total formation cross section is represented with the black thick line.

As described in Sect. 1.2.2, quasi-substitutional configurations such as $(1s)_{\pi^-} \otimes (3s_{1/2})_n^{-1}$ are enhanced in the small reaction angle. In the meantime, other configurations start to be significant as the reaction angle and the momentum transfer become larger. As shown in the bottom panel of Fig. 1.4, the contribution of the $2p$ state, which corresponds to the structure around BE = 2.5 MeV, appear in the finite reaction angles. In the experiment, we aim at simultaneous measurement of this $2p$ structure and the $1s$ peak structure by the measurement with the reaction angles ranging in $1 - 2$ degree.

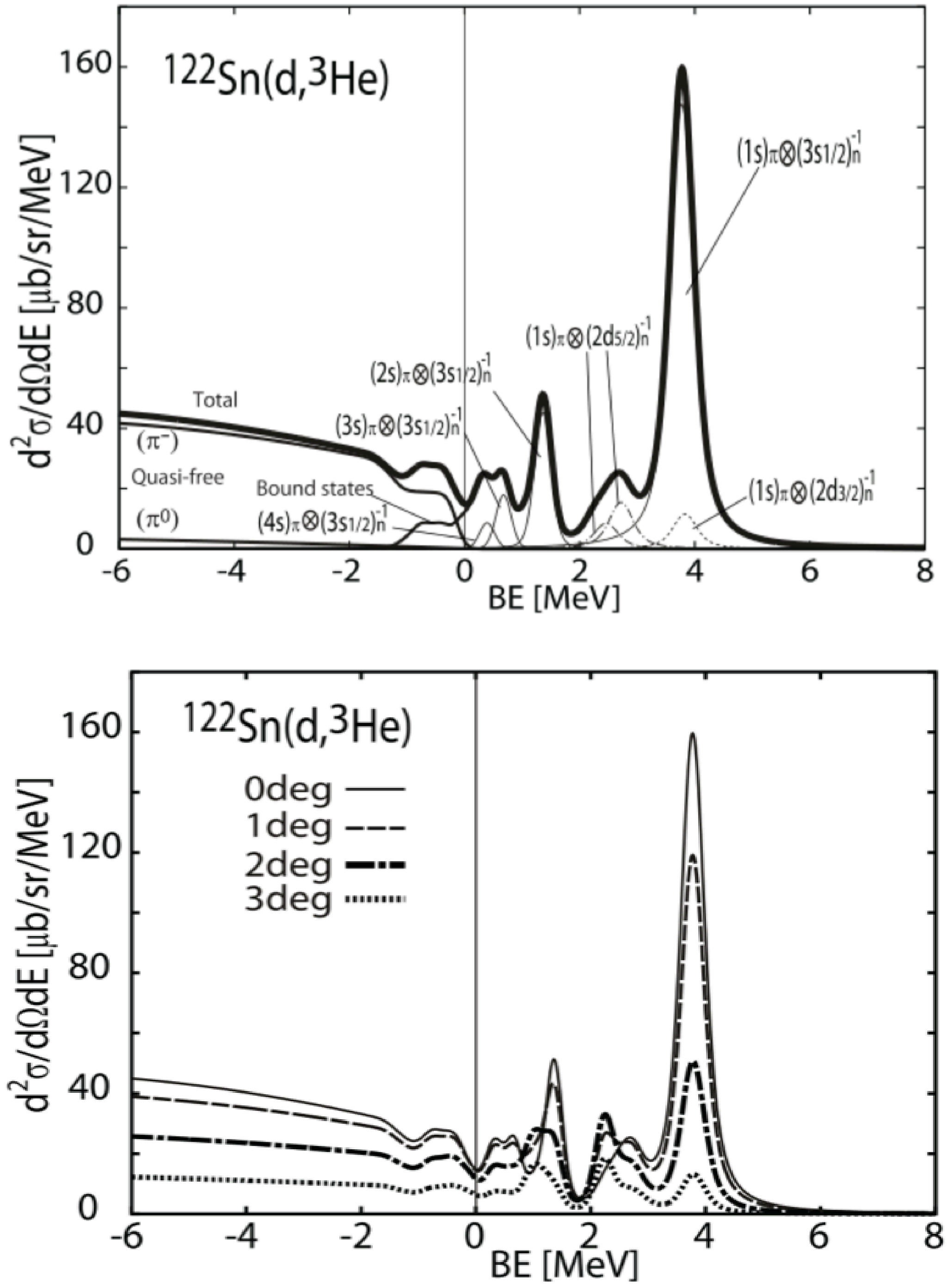

FIGURE 1.4: Theoretically calculated spectra for the formation of pionic states in the ^{122} with reaction angle = 0 (Top) and finite reaction angles (Bottom). The energy resolution of 300 keV(FWHM) is included to the calculation. In the top figure, The contribution of each configuration are represented. The contribution of quasi-free π^- and π^0 are also indicated. The total formation cross section is represented with the black thick line. The bottom figure shows the total cross sections with different reaction angles. The figures are cited from the reference [20].

1.6 Thesis objectives and outline

The thesis covers the details of the experimental spectroscopy of pionic atoms in ^{122,117}Sn $(d, ^3\mathrm{He})$ reactions. The experimental setup is described in Chapter 2. In Chapter 3 details of the data analyses are described. In Chapter 4 the measured excitation spectra of ^{121,116}Sn are presented as a result of the experiment. In the chapter, the binding energies and widths of deeply bound pionic atoms are determined. We also discuss the experimentally achieved data in view of pion-nucleus interaction. In the end, we evaluate the value of b_1 at finite density from the experimental data of simultaneous measurement of several pionic states.

The author conducted the experiment as a co-spokesperson, and took a major role for the experiment; design of the experimental procedure including beam and optical system tuning, setup of the multi wire drift chambers and segmented scintillators, test of the detector performance, and all analysis of the experimental data.

Chapter 2

Experiment

2.1 Experimental overview

The experimental goal is to obtain the binding energies and widths of deeply bound pionic atoms in ^{121,116}Sn through the measurement of the excitation spectra of the ^{122,117}Sn$(d, {}^{3}$He$)$ reaction near the π^- emission threshold, and evaluate the pion-nucleus optical potential parameter b_1 precisely.

The $(d, {}^{3}$He$)$ reaction in this experiment is interpreted as a pionic atom formation reaction. The incident deuteron beam picks up a neutron in the target, and at the same time a π^- is transferred to the target nucleus producing pionic atoms. A ^{3}He is emitted in the reaction with the kinetic energy of ~ 365 MeV reflecting the produced configurations of the π^- and the neutron hole states.

We have conducted an experiment at Radioactive Ion Beam Factory (RIBF) [22], the world-class heavy-ion accelerator facility, in RIKEN, Saitama, Japan in June 2014. Figure 2.1 shows a schematic view of the RIBF (Sect. 2.2). A primary deuteron beam with a maximum intensity of 400 pnA was accelerated by the Superconducting Ring Cyclotron (SRC) to 500 MeV (Sect. 2.3) and impinged on the tin targets (Sect. 2.4). The emitted ^{3}He in the $(d, {}^{3}$He$)$ reaction is identified and magnetically momentum-analyzed in the momentum range of 1460 MeV/c to 1510 MeV/c by the BigRIPS used as a spectrometer with a specially developed ion optics (Sect. 2.5). We installed pID detectors and tracking detectors near the dispersive focal plane F5 to identify and measure the ^{3}He trajectories (Sect. 2.6).

To achieve high resolution in the spectroscopy, we performed (1) tuning accelerator conditions to reduce the beam emittance and momentum. (2) tuning of the ion optics from an extraction point of SRC to the target. The details of (1) and (2) are explained in Sect. 2.3 and Sect. 2.5.5, respectively.

Trigger logic and DAQ system are described in Sect. 2.7. Finally run summary is presented (Sect. 2.8).

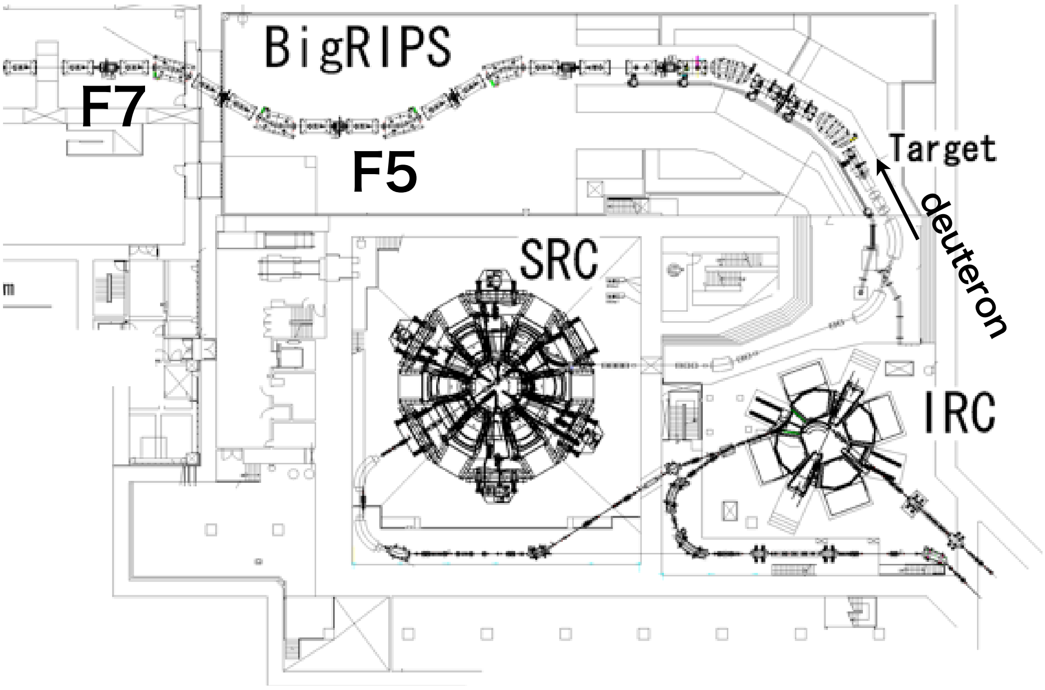

FIGURE 2.1: Schematic view of the Superconducting Ring Cyclotron (SRC) and the fragment separator BigRIPS adopted from the RIBF user's guide [23]. A deuteron beam was accelerated by the SRC to 500 MeV and impinges on the target. The emitted ^{3}He particles were magnetically analyzed by BigRIPS, used as a spectrometer, and detected in the focal planes F5 and F7.

2.2 RIKEN RI Beam Factory

Figure 2.2 shows a bird's-eye view of the RIBF, which consists of lower energy accelerators and newly constructed higher energy accelerators, FRC, IRC, and SRC. By using these accelerators, the RIBF provides intense heavy ion beams, i.e. ≈ 40 pnA for 345 MeV/u Uranium beam. A key component of the RIBF is the in-flight RI beam fragment separator, BigRIPS [24]. The high resolving power and large acceptance realize production of intense RI beam with wide range of masses and isospins.

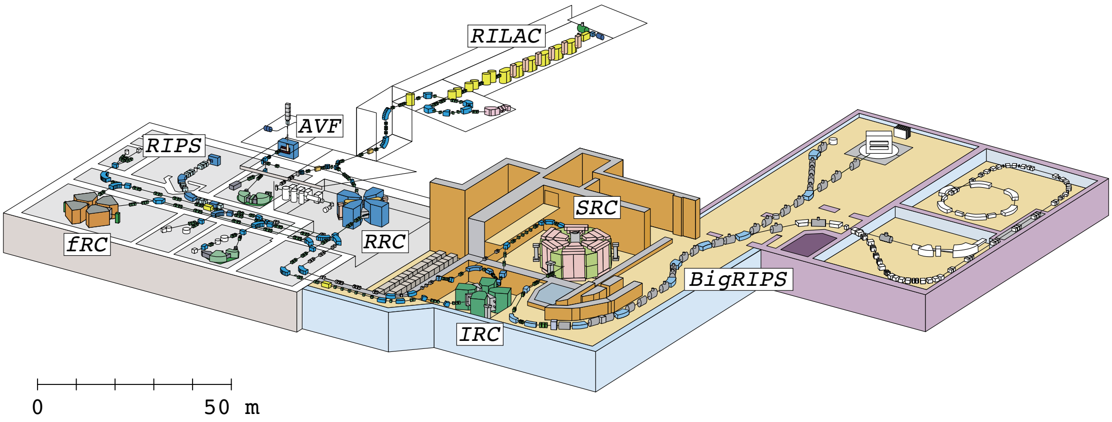
RILAC
AVF
RIPS
fRC
RRC
SRC
BigRIPS
IRC
0
50 m

FIGURE 2.2: The bird's-eye view of the RIKEN-RIBF. This figure is taken from the RIBF user's guide [23].

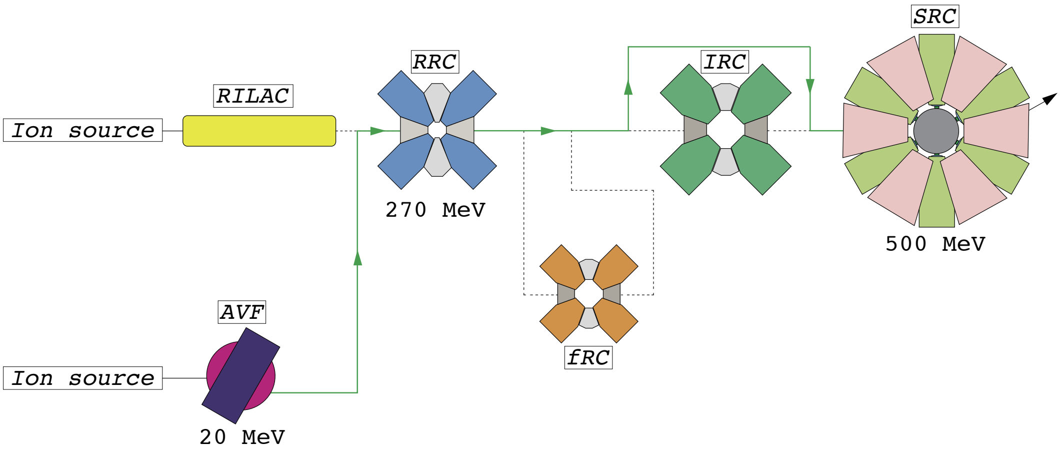
Ion source
RILAC
RRC
270 MeV
IRC
SRC
500 MeV
fRC
AVF
Ion source
20 MeV

FIGURE 2.3: The acceleration scheme for the deuteron beam in the experiment. AVF, RRC and SRC are used. This figure is taken from the RIBF user's guide [23].

2.3 Beam properties

We made use of a deuteron beam with the intensity of 400 pnA at maximum and the energy of 500 MeV. The primary deuteron beam was accelerated by three accelerators: AVF, RRC and SRC. The AVF accelerated the deuteron beam up to 20 MeV. The RRC then accelerated the beam from AVF up to 270 MeV. Finally the SRC accelerated the beam from RRC up to 500 MeV. The primary beam properties are described in this section.

2.3.1 Intensity and beam energy

The beam intensity was measured by Faraday cups installed in the beam line between SRC and the target and the luminosity on the target was continuously monitored by coincidence signals of three scintillation counters installed in the upstream of the target, counting the back-scattered particles. The luminosity was calibrated and normalized by using a ^{122}Sn target foil with sufficiently large size to cover the beam spot on the target. In the calibration, the beam intensity was changed by attenuators (See Sect. 2.3.3) and the counting rates of the back-scattered particles were measured and related to the beam intensity measured by the Faraday cups.

Figure 2.4 shows the relation between the count rate of the back-scattered particles at F0 and the beam intensity. By a linear fitting, we obtain a relation, beam intensity [pnA] = 0.04 × count rate of the back-scattered particles [cps]. While the production runs, we made use of 1 mm-wide strip targets. In that case, count rate of the back-scattered particles reflects the effective amount of the primary beam intensity hitting the target strip.

The incident deuteron beam energy was measured by using the Nuclear Magnetic Resonance probe (NMR) in the dipole magnets of BigRIPS and determined to be 501.3 MeV. The error of the primary beam energy is discussed in Sect 4.2.1.

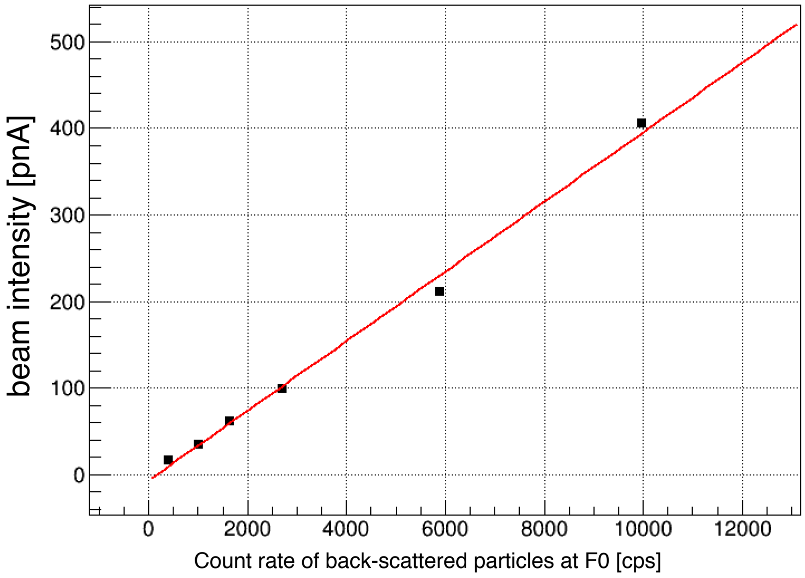

Figure 2.4: Relation between the count rate of the back-scattered particles at the target and beam intensity.

2.3.2 Emittance and momentum spread

The emittance and momentum spread were measured using the position and angle at the achromatic focal plane F3 and the dispersive focal plane F5 in the BigRIPS as shown in Fig. 2.5. The top and middle panel of the figure show the horizontal angle and position distributions measured at the F3 focal plane. From the widths of these distributions, the emittance of the beam was estimated. The bottom panel shows the horizontal position distribution at the F5 focal plane. By utilizing the dispersion at the F5 focal plane, the momentum spread was deduced from the distribution.

According to these measurements, the voltage and phase of the flat top cavity of SRC, the phase of the RF of RRC, and the voltage of the rebuncher were optimized. We also optimized the phase slit inside and the double slits downstream of the AVF cyclotron. After optimization, we achieved significantly better emittance of $0.2 \pm 0.04 \times 2.0 \pm 0.4\pi$ mm·mrad (horizontal/σ) and momentum spread of $0.03 \pm 0.006\%$ (RMS), which used to be $0.7 \times 3.0\pi$mm·mrad (horizontal/σ) and 0.04% (RMS) in the pilot experiment. The errors contains the deviation within a few hour measurement.

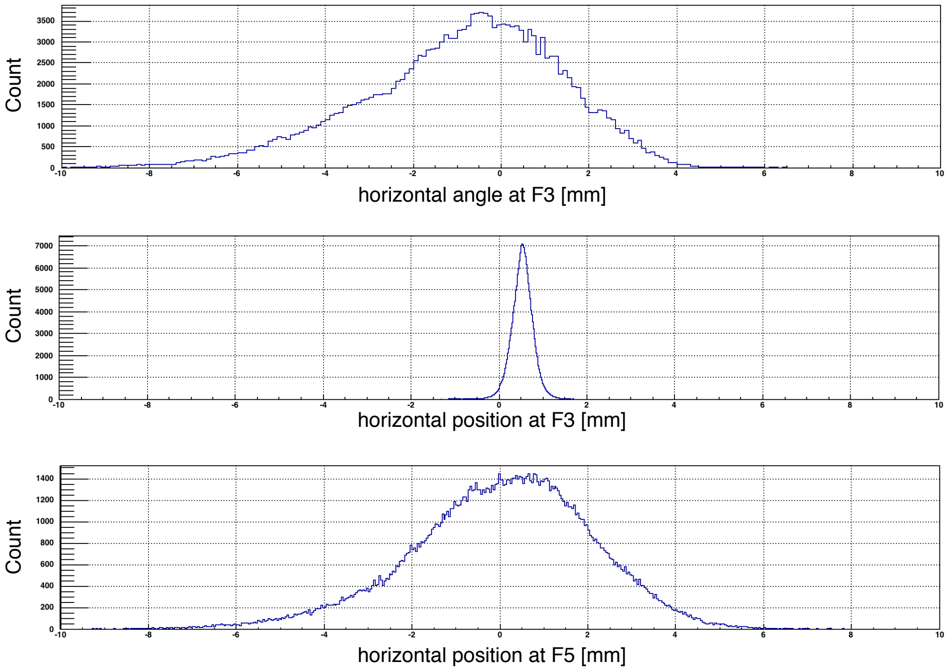

Figure 2.5: The beam profile measured at the achromatic focal plane (F3) and the dispersive focal plane (F5). The top and middle figures show the angular and position distributions at the F3 focal planes, which correspond to the beam emittance. The bottom figure shows the position distribution at the F5 focal plane, which corresponds to the beam momentum spread.

2.3.3 Stability of the beam properties

During the emittance measurement, a low-intensity beam of 1 – 0.1 nA was employed. Figure 2.6 shows attenuators of the same type used in the experiment. The attenuators have Honeycomb structures to keep the beam structures same. The ratio between holes and combs determines the attenuation factor. In the experiment, 11 attenuators were prepared, whose attenuation factors varied from 1/1.8 to 1/100. These attenuators were installed in the beam lines between the ion source and the AVF cyclotron, and the beam lines between the AVF cyclotron and the RRC cyclotron avoiding the focused point. The beam envelope was monitored by the wire-scanners in the upstream of the target in case that an attenuator was installed or deinstalled.

Figure 2.7 shows the measured beam envelope by a wire-scanners on the online monitors. the wire scanner has three wires, which scan the spatial beam distribution in horizontal, vertical, and 45-degree tilted axes, respectively. The beam envelopes are represented as the blue, magenta, and sky-blue lines with the unit of mm. The black lines corresponds to reference data, which were used to compare the beam envelopes in each conditions. As a result, it was confirmed that all of the attenuators used in the experiment did not change the beam emittance. The beam envelope was also monitored in the production runs every a few hours by profile monitors, and confirmed to be stable.

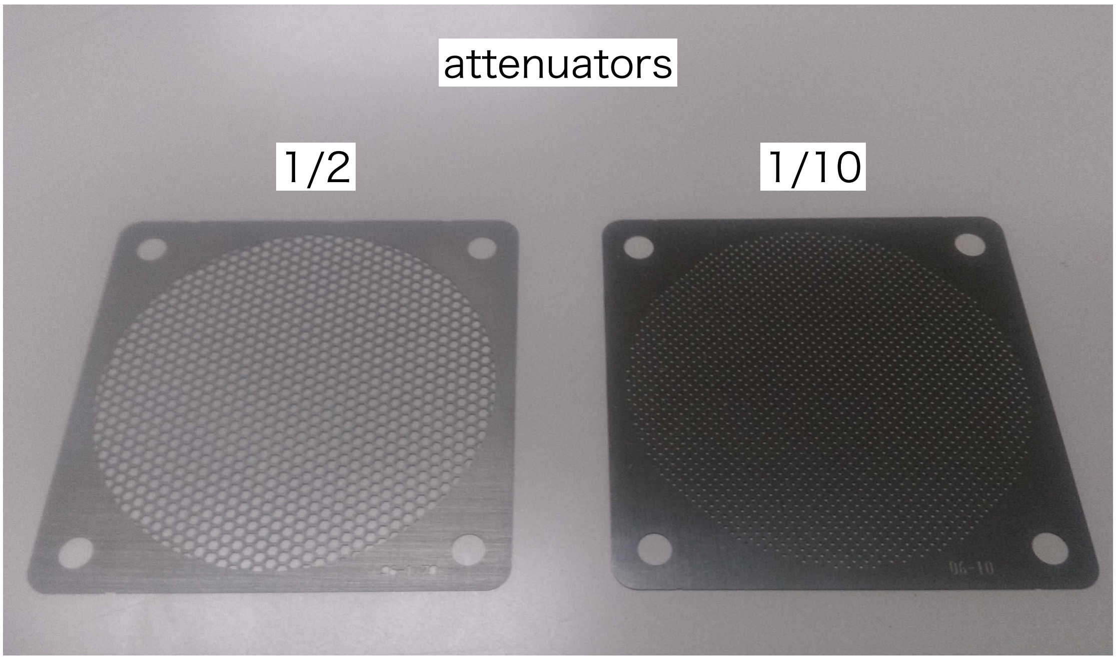

Figure 2.6: Attenuators used in the experiment. The attenuators have Honeycomb-like structures to keep the beam structures. The ratio between halls and combs determines the attenuation factor. The left and right attenuators have the attenuation ratio of 1/2 and 1/10, respectively.

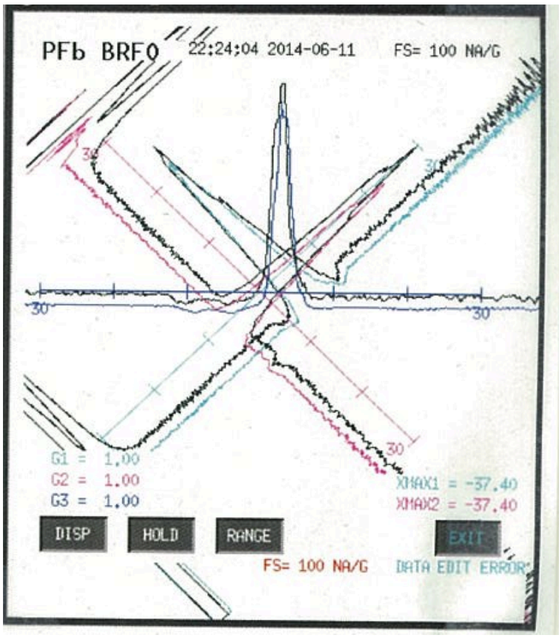

FIGURE 2.7: The measured beam envelope by the wire-scanners on the online monitors. The beam envelopes are represented as the blue, magenta, and sky-blue lines with the unit of mm. The black lines corresponds to reference data, which were used to compare the beam envelopes in each conditions.

2.4 Target

The prepared targets in the experiment are listed in Table 2.1. The 1 mm width strip targets of ^{122}Sn and ^{117}Sn are for the production runs. The width is determined to achieve good experimental resolution by limiting the beam momentum bite (In the experiment, target is installed at a dispersive focal plane. See section 2.5). A ^{122}Sn target with a larger size is prepared for the intensity calibration (See section 2.3). Polyethylene target is for the energy calibration and is used as a proton target for the well-known two-body kinematics of the $p(d,^3\text{He})\pi^0$ reaction.

Material	Thickness	Width	Purpose
^{122}Sn	12.5 ± 0.5 mg/cm^2	1.0 mm	Production
^{117}Sn	9.9 ± 0.5 mg/cm^2	1.0 mm	Production
^{122}Sn	12.2 ± 0.5 mg/cm^2	10.0 mm	Beam intensity calibration
polyethylene	100 ± 1 μm	2.0 mm	Production

TABLE 2.1: Target list

2.5 Spectrometer system

In this section, we describe the spectrometer system used for measuring the excitation spectra of pionic tin isotopes. The ion optics used in the experiment is also described. Sect. 2.5.1 defines notation for the following analysis.

For the spectroscopy of deeply-bound pionic atoms in RIKEN, a new ion optics was invented in the pilot experiment [19]. Since a typical momentum spread of the primary beam at RIBF is estimated to be 0.1%(FWHM)[1], which can be a dominating source of resolution deterioration in precise spectroscopy, we need to suppress the contribution of the momentum spread. Thus, we adopted a dispersion-matching method [25–27] for the ion optics. The concept of the dispersion matching method is explained in Sect. 2.5.2 and its adoption in the beam transfer line and the BigRIPS are described in Sect. 2.5.3,2.5.4 and2.5.6,2.5.7, respectively. In Sect. 2.5.5, the optimization of the beam transfer line is described.

2.5.1 Notations of the ion optical parameters

Let us here define notations for the following analysis. A horizontal position of a particle is represented as x. The sign of the x is defined as plus for the lefthand from upstream view. Horizontal and vertical angles are represented as a and b, respectively. A momentum deviation of a particle from that of a central momentum is represented as δ. Here, the central momentum is defined as the momentum of a particle in the central trajectory of the beam line. The subscript represents where the parameter is measured; i.e. a_{F5} means the horizontal angle at F5 focal plane.

Elements of transfer matrices are represented as

$$\begin{aligned}&(\text{parameters in the down stream}|\text{parameters in the upstream})\\ \equiv\ &\partial(\text{parameters in the down stream})/\partial(\text{parameters in the up stream}).\end{aligned} \tag{2.1}$$

For example, a proportionality coefficient of a position at F5 focal plane as a function of a horizontal angle at F0 can be represented as $(x_{\mathrm{F5}}|a_{\mathrm{F0}})$. This representation is expanded for higher order of the transfer matrix, such as $(x_{\mathrm{F5}}|a_{\mathrm{F0}}\delta)$ and $(a_{\mathrm{F5}}|a_{\mathrm{F0}}^3)$. These elements correspond to $\partial^2 x_{\mathrm{F5}}/\partial a_{\mathrm{F5}}\partial\delta$ and $\partial^3 a_{\mathrm{F5}}/\partial a_{\mathrm{F0}}^3$, respectively. The parameter δ does not have the subscript because the δ does not change the value from F0 to F5.

---

[1] This value is assumed from the momentum acceptance at the electric deflection channel (EDC), which is the entrance of the extraction system inside SRC.

2.5.2 Dispersion matching

In an ordinary experimental condition where the target position is designed to be ion-optically achromatic, missing mass resolution is directly deteriorated by the intrinsic momentum spread of the primary beam. This is because the momentum deviation of the incident beam from the central value, $\delta p_{\text{primary}}$ is reflected in the track positions at the dispersive focal plane x_{fp} as

$$x_{\text{fp}} = (CS_{16} + S_{11}B_{16})\delta p_{\text{primary}}, \tag{2.2}$$

where C, S_{11}, S_{16} and B_{16} are kinematical factor of the reaction, magnification and dispersion of the spectrometer, and dispersion of the beam line at the target, respectively. In the dispersion matching method, to suppress the effect of the $\delta p_{\text{primary}}$, the S_{11}, S_{16} and B_{16} are adjusted to realize the following condition,

$$CS_{16} + S_{11}B_{16} = 0. \tag{2.3}$$

The kinematical factor C for pionic atom production reaction of $(d, {}^3\text{He})$ is 1.31. In an experiment, we need to design the ion optics so as to have the left side of Eq. (2.3) small enough. Our designed value is estimated to be sufficiently small as

$$\begin{aligned} CS_{16} + S_{11}B_{16} = {} & 1.31 \cdot 62.0 - 1.82 \cdot 44.6 \\ = {} & 0.048 \text{ [mm/\%]}. \end{aligned} \tag{2.4}$$

The details of the designed transfer matrices are described in the following subsections.

2.5.3 Beam transfer line

We call the beam line connecting the SRC and the standard target position of the BigRIPS as the beam transfer line. The total length of the beam transfer line is about 42 m. The magnet configuration of the beam transfer line is

QQ - QT - D - QD - QD - D - QT - D - QT,

where D denotes a dipole magnet, and QQ, QT and QD a quadrupole quartet, triplet and doublet, respectively. Figure 2.8 shows a top view of the beam transfer line. The bending angle of dipoles are 20, 50 and 50 degrees for the three dipoles from the upstream, respectively. The specification of the dipoles are summarized in Table 2.2. Here, DMT1-3 are model numbers of the dipole magnets.

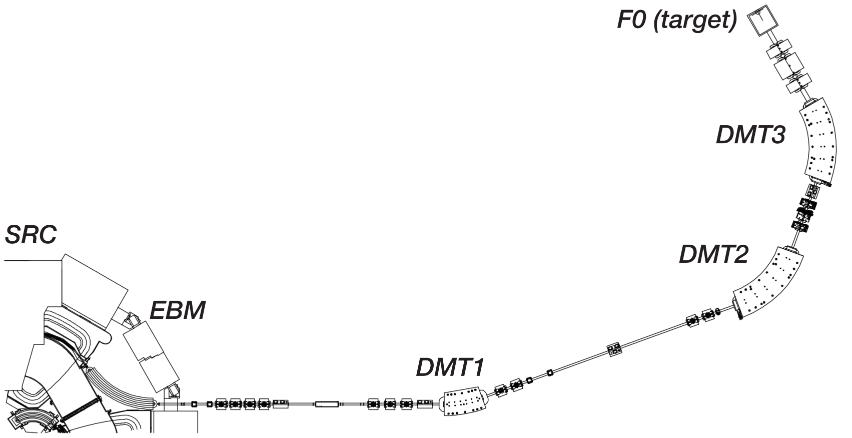

FIGURE 2.8: A schematic view of the extraction and transfer beam lines from SRC to RIBF standard target position.

Dipole magnet properties	DMT1	DMT2-3
Bending angle [degree]	20	50
Radius of central trajectory [m]	5	4.02
Pole gap [cm]	5	5
Max. magnetic field [A]	1.7	1.7

TABLE 2.2: Specifications of dipoles in beam transfer line.

2.5.4 Ion optics design for beam transfer line[2]

In the present experiment, a primary beam is used as an incident beam. Thus, we need to consider the optical properties of the SRC itself. The transfer matrix from the electric deflection channel (EDC) in the SRC to the normal-conducting bending magnet (EBM), the exit of the extraction system, is calculated using a 5th order Runge-Kutta-Fehlberg method based on the magnetic field map of the SRC. In the calculation, bending of the particles by the magnetic field is included. The transfer matrix of the beam transfer line is designed using COSY INFINITY [29, 30]. The first order transfer matrix in the beam transfer line is

---

[2] The large part of this section and the next section are taken from the Ref. [28]

$$\begin{pmatrix} (x|x) & (x|a) & (x|y) & (x|b) & (x|\delta) \\ (a|x) & (a|a) & (a|y) & (a|b) & (a|\delta) \\ (y|x) & (y|a) & (y|y) & (y|b) & (y|\delta) \\ (b|x) & (b|a) & (b|y) & (b|b) & (b|\delta) \end{pmatrix}_{\mathrm{EDC}\rightarrow\mathrm{F0}}$$

$$= \begin{pmatrix} -0.38 & 0.0 & 0.0 & 0.0 & 44.6 \\ -0.20 & -2.634 & 0.0 & 0.0 & 0.0 \\ 0.0 & 0.0 & 0.96 & 0.0 & 0.0 \\ 0.0 & 0.0 & -0.25 & 1.04 & 0.0 \end{pmatrix}, \tag{2.5}$$

where units of positions, angles and momentum deviations are mm, mrad and %, respectively. While the target position F0 is designed to be achromatic focus in “standard optics”, in our optics F0 is dispersive to realize the dispersion matching condition. Beam trajectories with the first-order calculation from EBM to F0 are displayed in Fig. 2.9.

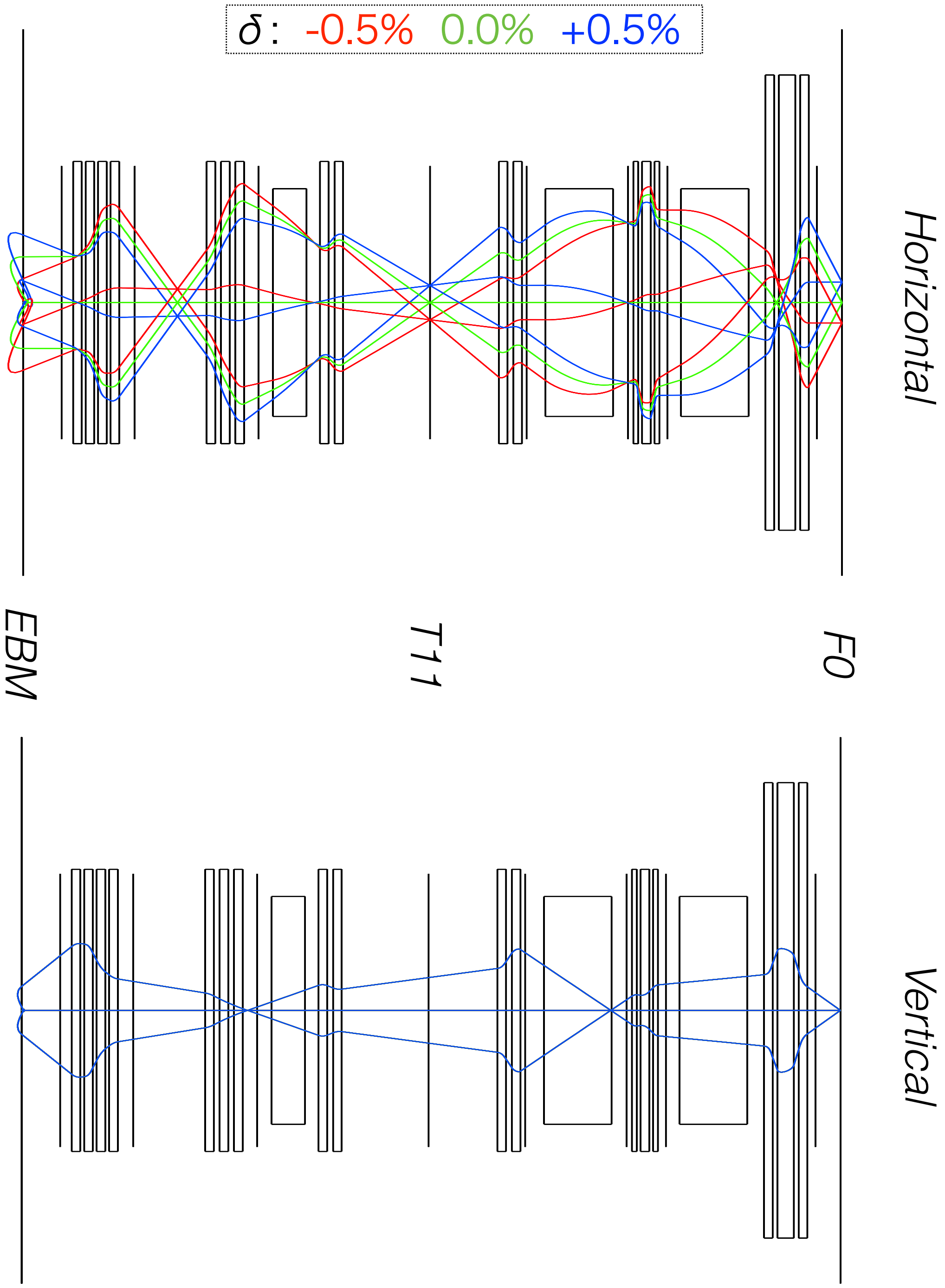

FIGURE 2.9: Optics of the beam transfer line. Calculated beam trajectories in horizontal direction (top) and in vertical direction (bottom) are shown. The red, green, and blue lines in the top figure correspond to the different relative momentum difference. Three lines correspond to the horizontal angle of -1, 0 and +1 mrad. In the bottom figure the lines are monochromatic, because in the vertical direction the particles with different momentum has same trajectories. The trajectories at EBM reflect the transfer matrix from EDC to EBM. The figure is taken from [28].

2.5.5 Beam transfer line optimization

To optimize the dispersion at F0, we developed a new method using position information at the F3 and F5 focal planes. In RI beam factory, the ion optics in the BigRIPS are well controlled by a tracker in each focal plane. Meanwhile, there are no high-precision position/angle detectors in the beam-transfer line to tune the optics, and the ambiguities are large.

In the new method, δ and x_{F0} are deduced through the position measured at the F3 and F5 focal planes, x_{F3} and x_{F5}, using the following equations:

$$x_{\mathrm{F0}} = x_{\mathrm{F3}}/(x_{\mathrm{F3}}|x_{\mathrm{F0}}), \tag{2.6}$$

$$\delta = \{x_{\mathrm{F5}} - (x_{\mathrm{F5}}|x_{\mathrm{F3}})x_{\mathrm{F3}}\}/(x_{\mathrm{F5}}|\delta). \tag{2.7}$$

Because of achromatic transport from F0 to F3, the position at F3 is reflecting the position at F0 directly. These transfer matrix elements of BigRIPS are measured in advance by setting the optics of the beam-transfer line to the standard mode, in which the F0 focal plane is achromatic. Figure 2.10 shows the 2D plot of the deduced δ and x_{F0}. By using this method, we succeeded in measurement and improvement of the optics in the beam-transfer line.

As a result, the dispersion of the beam transfer line was tuned to be 28 mm/%. Still the value was not equal to the designed values, the values were closer compared with that of the pilot experiment, 24 mm/%, and the contribution of the primary beam momentum spread for the resolution was suppressed. The 4 mm/% difference corresponds to the reduction of the contribution of $\delta p_{\mathrm{primary}}$ for missing-mass resolution from 280 keV to 220 keV (FWHM). The detail of the calculation is shown in Sect. 3.7.1.

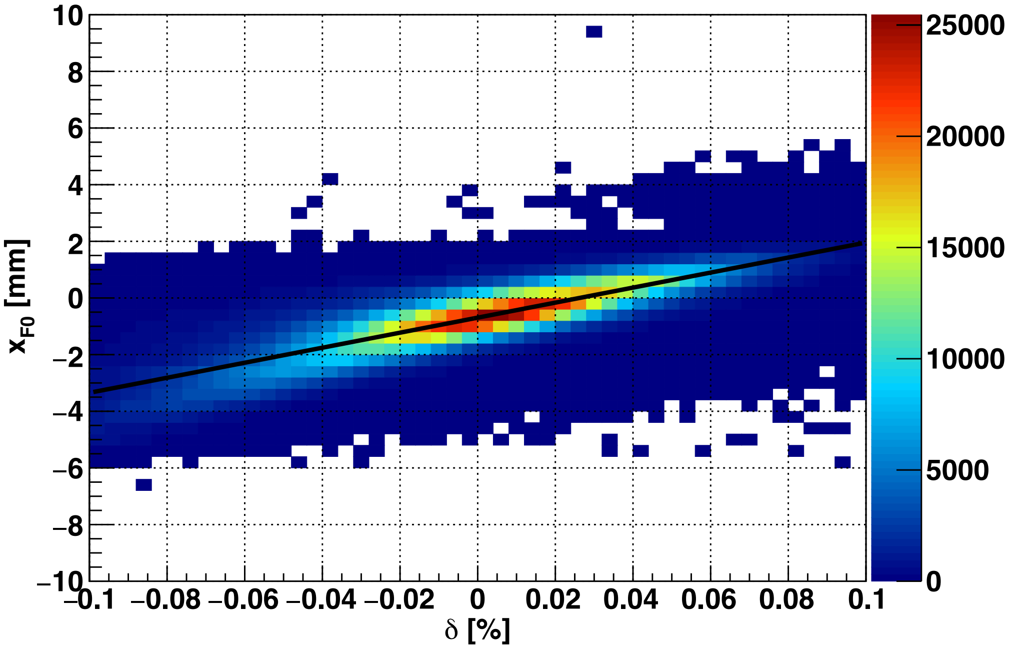

FIGURE 2.10: Color plot of x_{F0} versus δ deduced from x_{F3} and x_{F5}. The slope corresponds to the dispersion at F0.

2.5.6 BigRIPS

The BigRIPS consists of six room-temperature dipole magnets with the bending angle of 30 degrees (D1 to D6), fourteen superconducting quadrupole triplets (STQ1 to STQ14) and 7 focal planes (F1 to F7). The primary beam is dumped in D1. The magnet configuration is

(F0)-QDQ-(F1)-QDQ-(F2)-QQ-(F3)-QDQ-(F4)-QDQ-(F5)-QDQ-(F6)-QD-(F7),

as shown in the Fig. 2.11. Here, Q denotes Superconducting triplet quadrupole magnets (STQ). Properties of the dipole and quadrupole magnets are summarized in Table 2.3 and 2.4. The total length of the BigRIPS spectrometer is 77 m between the F0 and F7 focal planes.

The angular acceptance is about ±20 mrad in horizontal direction and about ±40 mrad in vertical direction in our optics. The large acceptance of the BigRIPS is realized by the superconducting quadrupoles with large apertures, and this feature is indispensable in identifications of combinations of pionic bound states and neutron hole states according to the angular dependence of the formation cross section.

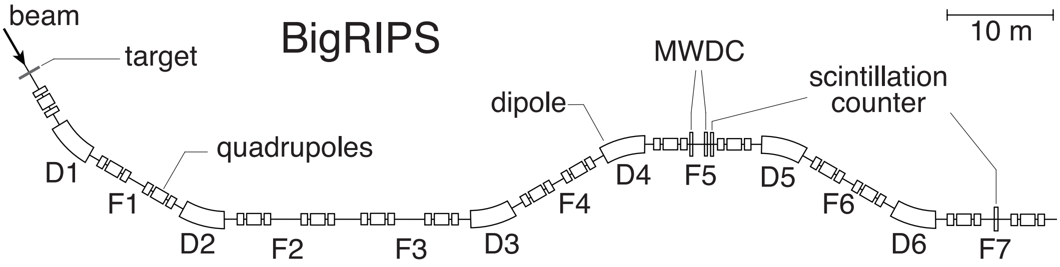

Figure 2.11: A schematic view of BigRIPS and the detector setup.

Dipole magnet properties	
Bending angle [degree]	30
Radius of central trajectory [m]	6
Maximum magnetic field [T]	1.6
Pole gap [cm]	14
Path length [mm]	3140
Effective length [mm]	120
Maximum current [A]	1100
Current density [A/mm^2]	5.6
Number of turns/coil [turn/Coil]	100

Table 2.3: Specifications of dipoles in BigRIPS.

STQ name	Bore radius [mm] (room temp.)	Effective length [mm]			Max. field gradient [T/m]		
		Q1	Q2	Q3	Q1	Q2	Q3
STQ1	120 (90 for Q1)	500	800	500	24	20	20
STQ2-4	120	500	800	500	14.1	14.1	14.1
STQ5-6,STQ10-11	120	500	1000	500	14.1	14.1	14.1
STQ7-9,STQ12-14	120	500	800	500	14.1	14.1	14.1

Table 2.4: Specification of quadrupoles in BigRIPS.

2.5.7 Ion optics design for BigRIPS

Ion optical settings of the BigRIPS are also designed using the COSY INFINITY. The F1 and F5 focal planes are designed to be dispersive and beam-focused planes in horizontal and vertical directions (double-focusing), while the F2, F3 and F7 focal are designed to be achromatic and double-focusing planes. The optical conditions from F3 to F5 and from F7 to F5 are symmetric. The obtained first-order transfer matrix from the target to the dispersive focal plane F5 is

$$\begin{pmatrix} (x|x) & (x|a) & (x|y) & (x|b) & (x|\delta) \\ (a|x) & (a|a) & (a|y) & (a|b) & (a|\delta) \\ (y|x) & (y|a) & (y|y) & (y|b) & (y|\delta) \\ (b|x) & (b|a) & (b|y) & (b|b) & (b|\delta) \end{pmatrix}_{\mathrm{F0}\rightarrow\mathrm{F5}}$$

$$= \begin{pmatrix} -1.82 & 0.0 & 0.0 & 0.0 & 62.0 \\ 0.04 & -0.54 & 0.0 & 0.0 & 0.0 \\ 0.0 & 0.0 & -1.63 & 0.0 & 0.0 \\ 0.0 & 0.0 & -0.18 & -0.61 & 0.0 \end{pmatrix}, \tag{2.8}$$

where units for elements are same as these of optics from EDC to F0. The beam trajectories of the first-order calculation from F0 to F7 are displayed in Fig. 2.12.

The intrinsic momentum resolution of the whole optical systems is $\Delta p/p = (M \cdot \Delta x_0)/D$, where Δx_0 denotes the full monochromatic beam size on target, and M and D are the magnification and dispersion from F0 to F5. If we assume the monochromatic beam spot size of 1.0 mm (FWHM) on the target, the expected momentum resolution for the ion optical setting of Eq. (2.8) is

$$\begin{aligned} \Delta p/p = & \quad (1.82 \cdot 1.0)/62.0 \\ = & \quad 0.029\% \text{ (FWHM)} \end{aligned} \tag{2.9}$$

under dispersion matching condition. This momentum resolution corresponds to the energy resolution of about 200 keV (FWHM) for 365 MeV ^{3}He of the (d,^{3}He) reaction.

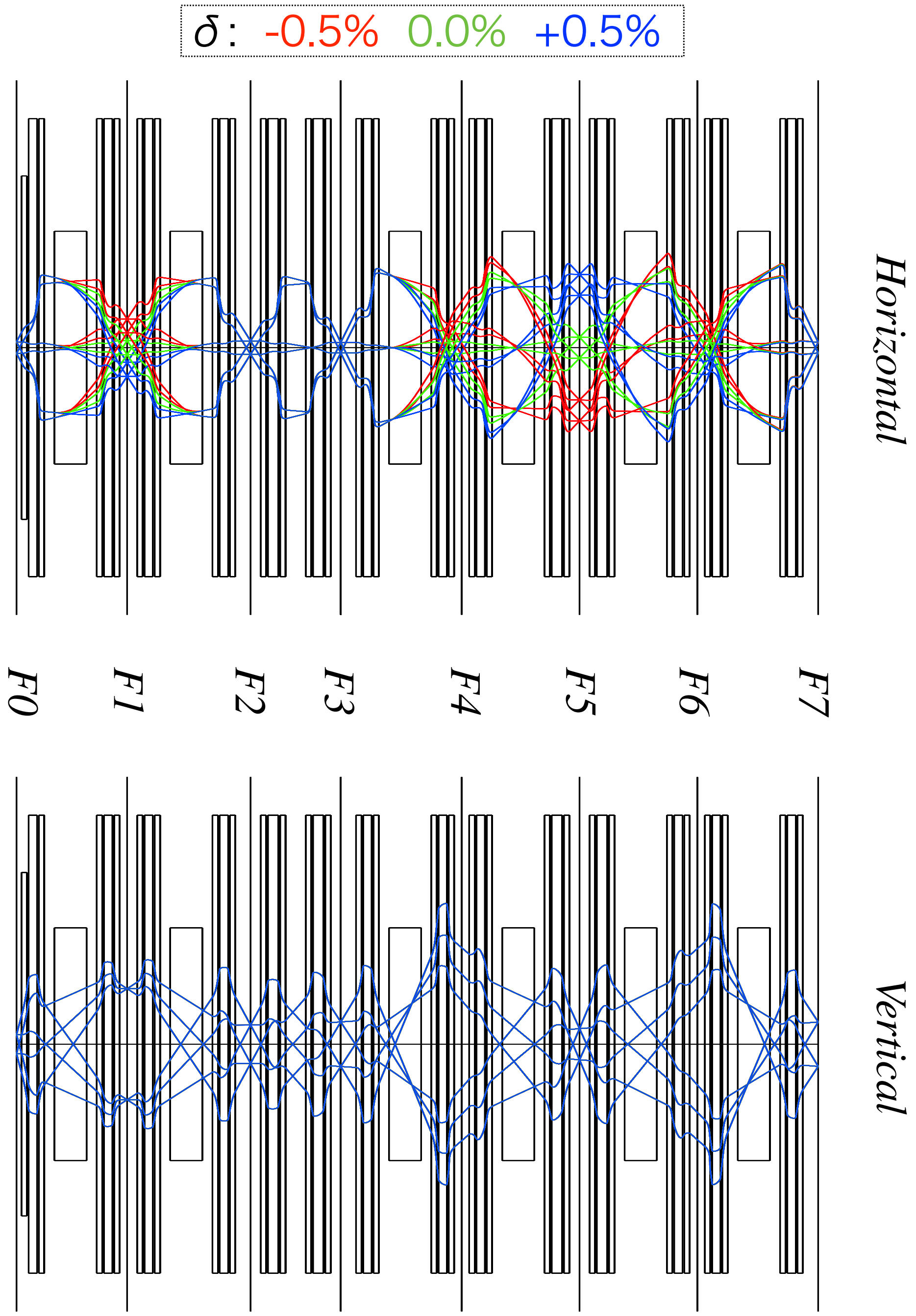

Figure 2.12: Calculated beam trajectories in BigRIPS in horizontal direction (top) and in vertical direction (bottom) are shown. The colored lines in the top figure correspond to the different relative momentum difference. Three lines correspond to the horizontal angle of -1, 0 and +1 mrad. In the bottom figure the lines are monochromatic, because in the vertical direction the particles with different momentum has same trajectories. Three lines correspond to the horizontal angle of -3, 0 and +3 mrad. The figure is taken from [28].

2.6 Detectors

We installed scintillators at the F5, F7 and F8 focal planes and two multi-wire drift chambers (MWDCs) at the F5 focal planes. A ^{3}He was identified by three means: (i) the time of flight (ToF) between F5 and F7 focal plane, (ii) energy loss in MWDCs, which was measured as time over threshold and (iii) relative timing to the RF of cyclotron.

The excitation energy of the reaction products and reaction angles of the ^{122,117}Sn(d, ^{3}He) reaction are derived by the trajectories of ^{3}He at the dispersive focal plane F5 measured by the MWDCs. The scintillator at F7 is a standard detector of BigRIPS, whose thickness is 3 mm. We also installed two low-pressure multi-wire drift chambers (lp-MWDCs) during the tuning of the transfer matrix in the beam transfer line as described in Sect. 2.5.5 and the beam emittance measurement as described in Sect 2.3.2. The lp-MWDCs are uninstalled during the production and calibration runs.

2.6.1 Low-pressure multi-wire drift chambers at F3

The two low-pressure multi-wire drift chambers (lp-MWDCs) [31] at F3 were used for the tuning of the beam transfer line and the measurement of the beam emittance. Each lp-MWDC consists of four planes, X, X′, Y, Y′. In X plane wires are set vertically and in Y planes wires are set horizontally. The prime means the wire position are set alternately. Effective area is 216 × 144 mm^{2}, with 9 mm wire spacing. Lp-MWDCs were installed into vacuum chamber and operated with 50 kPa isobutane gas. The plane resolutions were 60 – 70 μm (RMS), and plane efficiencies were more than 99%.

2.6.2 Multi-wire drift chambers at F5

Each MWDC consists of eight planes, X1, X′1, X2, X′2, U, U′, V, V′. One plane has 48 sense wires with 5 mm spacing. The dimensions of the active area of each plane is 250 mm × 150 mm. Here, 250 mm corresponds to about 27 MeV in energy scale. In X plane wires are set vertically and in U and V planes wires are set with an angle of 15 and -15 degree from that in X plane respectively. The prime means the wire position are set alternately.

The top panel of Fig. 2.14 shows the front view of the sense wires as seen in beam axis. The bottom panel of Fig. 2.14 shows the top view of the X and X′ planes.The sense wires are made of gold-plated tungsten and their diameter is 12.5 μm, while potential wires are made of gold-plated copper and their diameter is 75 μm. The distance between sense wires and potential wires is 2.5 mm. Aluminized Kapton films of 7.5 μm are used as cathode planes. MWDCs were operated with one atom mixtures gas (argon : metylal : isobutone = 74 : 10 : 28). The methylal was used to eliminate the accumulated polymers formed by recombination of organic molecules in the quenching gas. The voltage of -1200 V were applied to the potential wires of the upstream MWDC and of -1150 V to these of the downstream MWDC. To the cathode planes 50 V lower voltage are applied: -1250 for the upstream MWDC and -1200 for the downstream MWDC. In the V' plane of downstream MWDC, which was the most downstream plane, signals from some wires could not be detected in the experiment. Therefore, in the analysis we do not use the signals from the V' plane of downstream MWDC to avoid non-uniformity. The resolution and efficiency of the MWDCs are evaluated in Sect. 3.2.

2.6.3 Scintillation counter at F5

The scintillator at F5 is segmented to two parts in vertical direction to keep good performance under a large number of breakup protons ($\approx 10^5$ particles/s). Figure 2.15 shows the schematic view of the scintillator at F5. For the F5 scintillators, EJ-212 plastic are used. The rise / decay time is about 0.9 / 2.4 ns and the pulse width is about 2.7 ns (FWHM). The refractive index is 1.58. The segmented two parts of scintillators have about 1 mm overlapped region, and the black delrins are attached to other regions to make the material thickness homogeneous. In the downstream of the F5 scintillator, 10 mm acrylic plastic board is attached as a degrader to make energy loss difference between ^{3}He and protons. In the experiment a number of break-up protons reached F5 focal plane, because the rigidity of the protons and that of ^{3}He were almost same ($\approx$ 2.47 Tm). After the F5 scintillator and the degrader, the rigidity of proton became about 2.43 Tm, while that of ^{3}He became 2.26 Tm. The inefficiency for ^{3}He particles is assumed to be negligible, because the scintillator is thick enough and could detect the minimum ionized particles (MIP). The energy loss of signal ^{3}He is about 8 times larger than that of MIP, and therefore the efficiency for ^{3}He is assumed to be high enough.

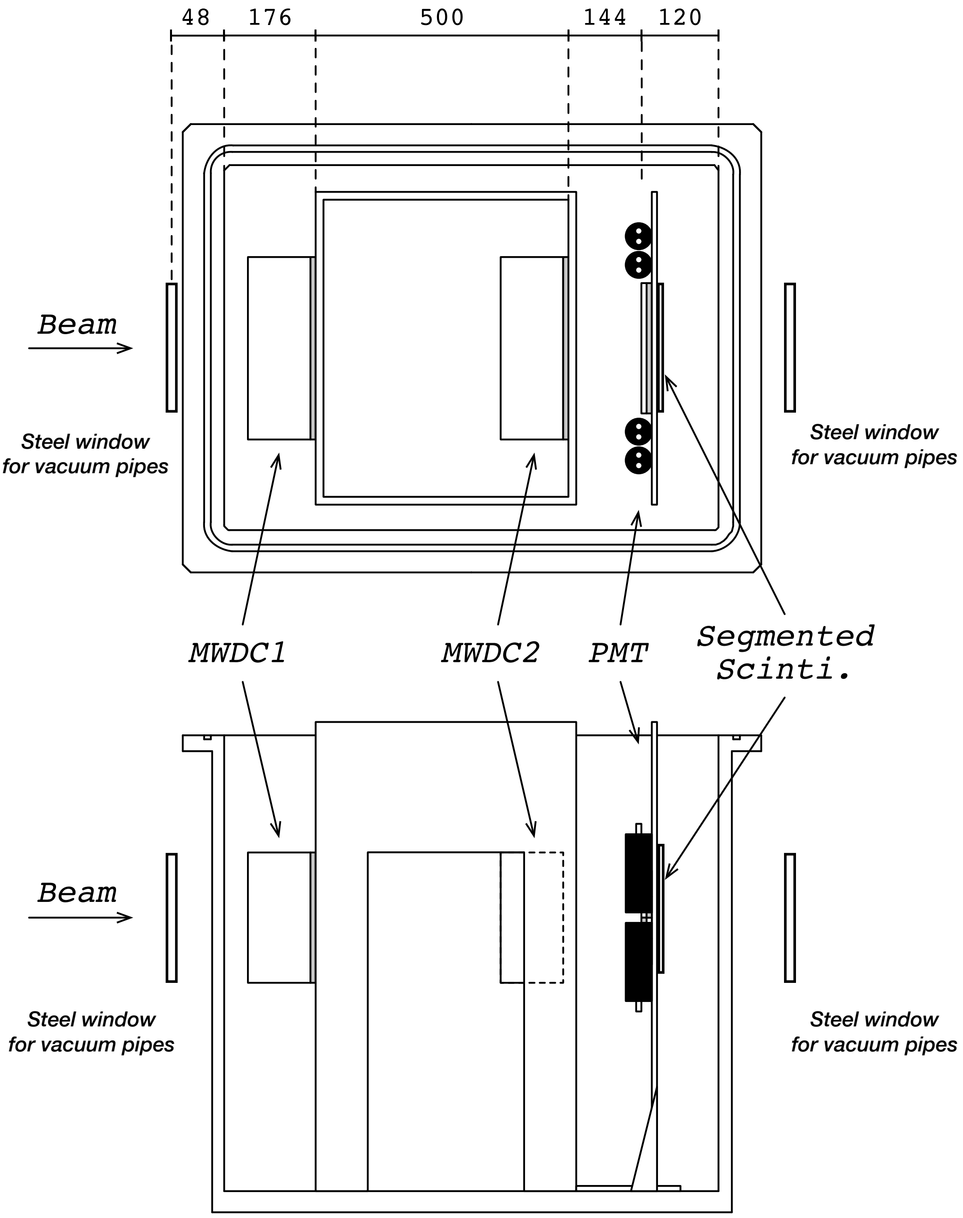
48
176
500
144
120
Beam
Steel window
for vacuum pipes
Steel window
for vacuum pipes
MWDC1
MWDC2
PMT
Segmented
Scinti.
Beam
Steel window
for vacuum pipes
Steel window
for vacuum pipes

FIGURE 2.13: Schematic drawings of the detectors and their stands in the F5 chamber. (Top) The view from above. (Bottom) The view from side. The figures are taken from [19].

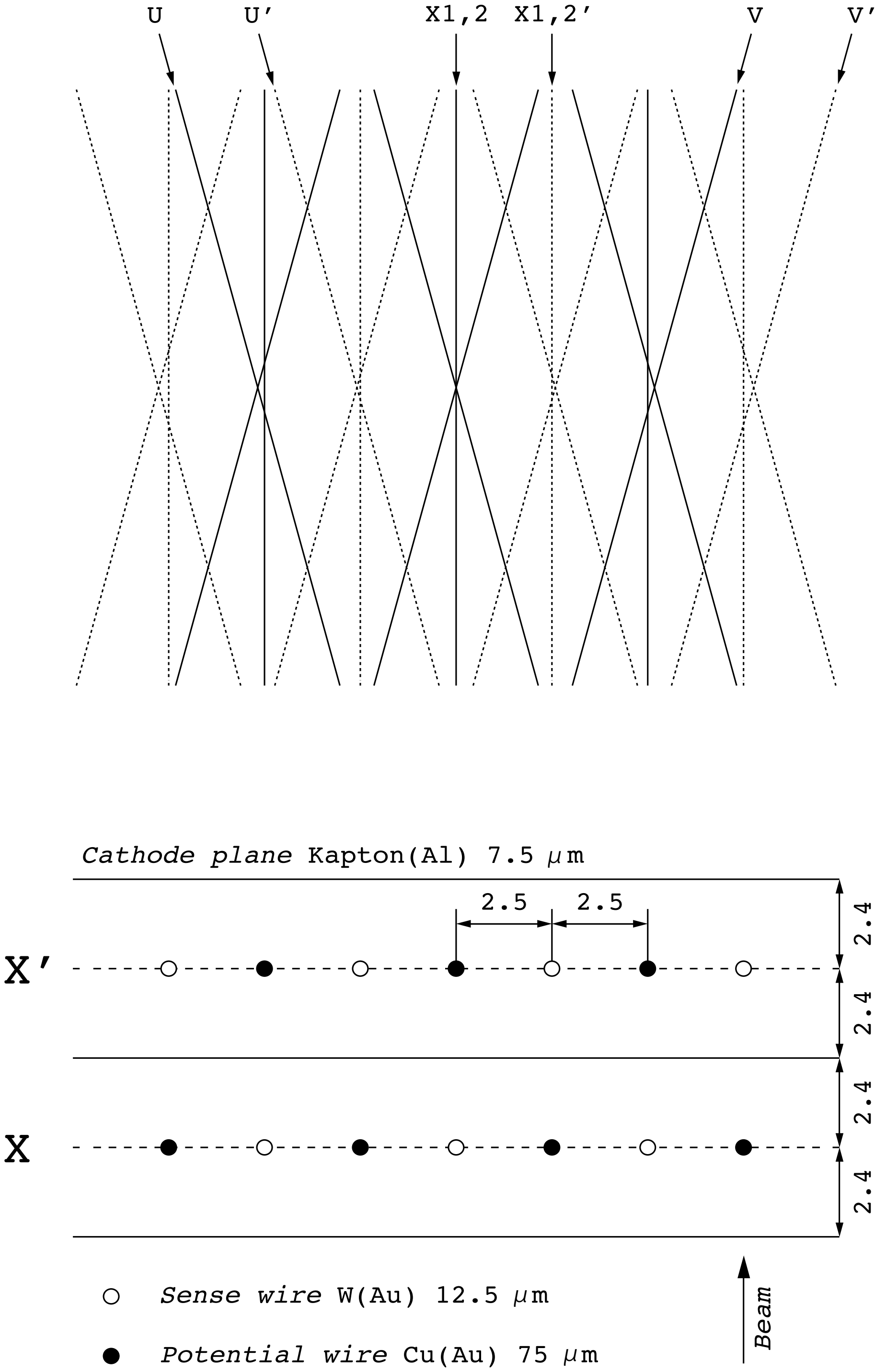
U
U′
X1,2
X1,2′
V
V′
Cathode plane Kapton(Al) 7.5 μm
2.5
2.5
2.4
2.4
2.4
2.4
X′
X
○ *Sense wire* W(Au) 12.5 μm
● *Potential wire* Cu(Au) 75 μm
Beam

FIGURE 2.14: A front view of sense wires in the drift chamber (top) and a top view of the X and X′ planes in the drift chamber (bottom) are displayed.
The figures are taken from [19].

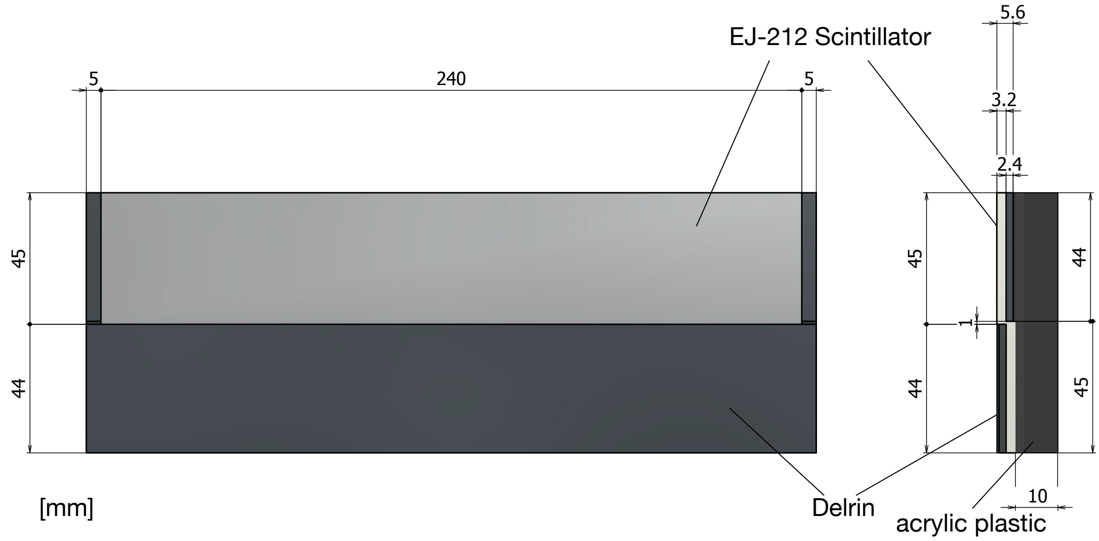

FIGURE 2.15: Schematic drawings of segmented scintillator.

2.7 DAQ and trigger logic

The signals from the MWDCs were amplified and discriminated by the amplifier shaper discriminators (ASDs), which were attached to the MWDCs directly. The time constant of ASDs were 16 ns for the upstream and 80 ns for the downstream MWDCs, respectively. The leading and trailing edge of the signal from the ASDs are read out by 64 ch VME-AMT module, which is multi-hit TDCs. The ASD and AMT-VME modules were developed in KEK [32, 33]. The signals from the F5 scintillators were amplified by PMTs (H7195B / Hamamatsu) and read out by 16 ch multi-hit TDC (V1290N / CAEN) and 16 ch multi-event QDC (V792N / CAEN). For the data acquisition system (DAQ), we adopted the RIBF DAQ, which is developed for the RIBF [34].

The trigger for the production runs was the coincidence of the delayed F5 trigger and the F7 trigger signals. The simplified trigger logic is shown in Fig. 2.16. Each trigger signal was produced by the mean time of signals from left and right PMTs for each scintillator. The delay time was adjusted to 170 ns corresponding to time of flight of ^{3}He. The gate width to accept the trigger, or the sum of the width of F5 and F7 signals, was about 50 ns. The coincidence trigger produced the trigger rate of about 200 Hz for the production runs, which was about the 1/1,000 of the count rate at F5 single trigger. As an unbiased trigger, the 1/10,000 prescaled F5 single trigger was also mixed.

The multi hit events caused the hardware trigger inefficiency for ^{3}He signals. As for the inefficiency the following two causes are evaluated; (i) ^{3}He and proton hit a F5 scintillator slat simultaneously within the signal propagation time and the coincidence of the PMTs on both sides did not measure ^{3}He appropriately. (ii) The preceding proton signals at F5 caused hardware deadtime in the coincidence circuit of the trigger logic.

(i) Multihit of ^{3}He and protons

For this inefficiency, the count rate of simultaneous hit of proton with the ^{3}He is evaluated. As explained in Sect. 3.1.3, the primary beam has bunch structures. As a result, the signals of ^{3}He were bunched within 20 ns and apart by about 25 ns from the main component of the background protons. The count rate of the protons in the same timing with the ^{3}He signals were 2 kHz, which is evaluated from the unbiased trigger events. This small count rate leads to the probability of case (i) to be less than 0.01%.

(ii) Hardware deadtime in trigger cirtuit

This inefficiency was caused by the non-updating discriminator after the delay modules for F5 signals represented in Fig. 2.16. In the case the proton signals arrived just before the ^{3}He signals, the proton signals made the discriminator blind. This deadtime of the discriminator caused the inefficiency.

Figure 2.17 shows the averaged timing of PMTs on both ends of the F5 scintillators for ^{3}He events. The blue line corresponds to the signals from ^{3}He, while the black line corresponds to the multi-hit background protons. The background protons arrived every 75 ns which corresponds to the cyclic structures in the primary beam. As shown in the figure, when the signals came between the red dashed lines, the trigger was not created. To estimated the ratio of the unrecorded events to recorded, the number of events in the same phase of cyclic structures represented by the black dashed lines are counted. As a result, the inefficiency is estimated to be 2%.

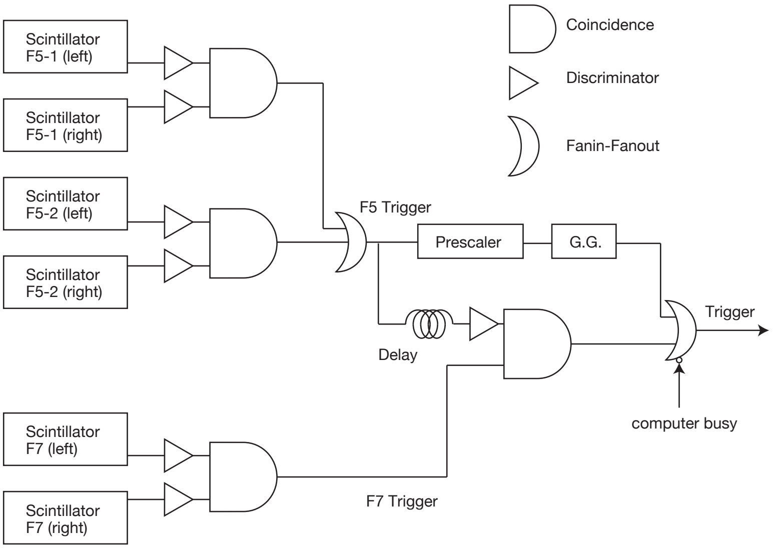
Scintillator F5-1 (left)
Scintillator F5-1 (right)
Scintillator F5-2 (left)
Scintillator F5-2 (right)
Scintillator F7 (left)
Scintillator F7 (right)
Coincidence
Discriminator
Fanin-Fanout
F5 Trigger
Prescaler
G.G.
Delay
Trigger
computer busy
F7 Trigger

FIGURE 2.16: A schematic diagram of the trigger logic. The trigger was made of the coincidence signal of the F5 and the F7 scintillators. The 1/10,000 prescaled F5 single trigger was also mixed.

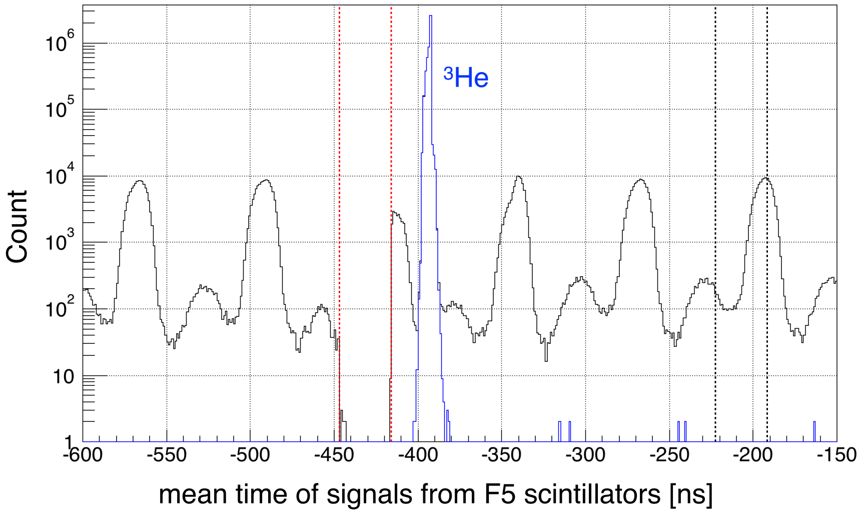

FIGURE 2.17: The averaged values of TDC signals from left and right side PMT of the F5 scintillators for ^{3}He events. The blue line corresponds to the signals from ^{3}He, while the black line corresponds to the multi-hit background protons. The ^{3}He signal accompanied by the accidental protons in the timing within red-dashed lines did not create the trigger. The ratio of such events are evaluated as the inefficiency of hardware trigger efficiency, from the number of event in the red-dashed lines.

2.8 Run summary

The experiment was performed in 11 days in June 2014. It took about 9 days for detector commissioning, tuning of primary beam and tuning of ion optics. Production runs for ^{122}Sn and ^{117}Sn target were performed for 14 hours and 4 hours, respectively. For the ion optical transfer matrix measurement (See Sect 3.3), additional runs with ^{122}Sn target were also taken. The total duration time, number of ^{3}He events, averaged beam intensity and their purpose are summarized in Table 2.5. Here, the listed intensity values correspond to the number of deuterons hitting the target. The intensity for polyethylene run is not listed, because the intensity calibration is performed only for Sn targets.

Target	Duration	^{3}He events	Intensity	Purpose
^{122}Sn	861 min.	3,381,613	108 enA	Production
^{117}Sn	251 min.	1,058,821	170 enA	Production
^{122}Sn	335 min.	1,147,318	108 enA	transfer matrix measurement
polyethylene	144 min.	3,896,081	-	Energy calibration

Table 2.5: Run summary of the experiment

Chapter 3

Data analysis

In this chapter the details of the experimental data analysis are described. To obtain the excitation spectra from the experimental data, we take following four steps in the analysis;
(i) selection of events including ^{3}He originating in the target by the ToF between the F5 and F7 focal planes, the energy loss in MWDC, and the event timing with respect to the radio frequency of the SRC (Section 3.1),
(ii) reconstruction of the ^{3}He trajectories at the F5 focal plane by MWDCs (Section 3.2),
(iii) deduction of the ^{3}He momenta at the target using the transfer matrix (Section 3.3),
(iv) conversion of the ^{3}He momenta to the excitation spectra (Section 3.4) after acceptance correction and normalization of the ^{3}He counts to the cross section (Section 3.5).

In the last part of the section, experimental resolution of the excitation spectra are evaluated (Sect. 3.7).

3.1 Event selections for ^{3}He

As described in Sect. 2.7 the DAQ trigger rate was amounted to about 200 Hz, which is sufficiently low with respect to the DAQ live rate. However, even after applying a 50 ns coincidence gate to the F5 and F7 timing differences to efficiently collect ^{3}He triggered events by the hardware trigger system, about 80% of the collected events were triggered by protons. At the stage of the data analysis events including ^{3}He are selected by (i) the time of flight between the F5 and F7 focal planes ($\mathrm{ToF}_{\mathrm{F5F7}}$), (ii) the energy loss measured by the MWDCs, and (iii) the time difference between the detecting time at the F5 focal plane and the radio frequency of the SRC. In the following sections, these three methods of ^{3}He event selection are explained. In the last part of the section, the efficiency and contamination of background particles are evaluated, including their position dependence.

3.1.1 Time of flight between the F5 and F7 focal planes

The time of flight between the F5 and F7 focal planes ($\equiv \mathrm{ToF_{F5F7}}$) was measured by the plastic scintillators in these focal planes. To identify the ^{3}He clearly by the $\mathrm{ToF_{F5F7}}$ information, timing offset between the two scintillator slats at F5 and their F5 position dependence are corrected. The $\mathrm{ToF_{F5F7}}$ after these correction is used for the ^{3}He event selection.

For the time offset correction between the slat 1 (upper segment) and the slat 2 (lower segment) as shown in Fig. 3.1, the ^{3}He produced in the $p(d,{}^3\mathrm{He})\pi^0$ is used. Triggered events are dominated by ^{3}He in this reaction. As explained in Sec. 2.7, the timing coincidence of F5 and F7 signals was used as the trigger. Figure 3.1 shows the averages of the TDC measured values for the signals from the PMTS at both ends of the F5 scintillators. Top and bottom panels show the signals from the slat 1 and the slat 2, respectively. Red lines represent "before timing calibration". The timing of slat 2 is corrected to be the black lines by a shift of 7.5 ch, which corresponds to about 200 ps (1 ch = 25 ps), through the comparison of the center of the peak structures in the red lines.

For the rough correction of the $\mathrm{ToF_{F5F7}}$ dependence on the ^{3}He momentum, namely, the position at the dispersive focal plane F5, the position at F5 is deduced solely from the timing difference between the left and right PMTs of the F5 scintillators ($\equiv \Delta t_{\mathrm{LR}}$) after calibration by the MWDCs.

Left panels of Fig. 3.2 show the relation between Δt_{LR} in each slat and position deduced from the tracking by the MWDCs at F5 ($\equiv x_{\mathrm{F5MWDC}}$) for the $p(d,{}^3\mathrm{He})\pi^0$ reaction. As shown, these two variables clearly indicate a linear corelations. The slopes are about 0.9 mm/ch, which correspond to the transmission speed of 1/4 of the speed of light and is consistent with naive calculation[1]. Based on the correlation, the position at F5 is deduced from Δt_{LR} ($\equiv x_{\mathrm{F5Sci}}$). Right panels of Fig. 3.2 show the difference between x_{F5MWDC} and x_{F5Sci} in each slat. The widths of the distribution are about 3 mm (RMS). The x_{F5Sci} is used to correct the F5 position dependence of the $\mathrm{ToF_{F5F7}}$.

Left top panel of Fig. 3.3 shows a two dimensional plot of $\mathrm{ToF_{F5F7}}$ and x_{F5Sci} measured in the $^{122}\mathrm{Sn}(d,{}^3\mathrm{He})$ reaction in a production run. The middle locus of the plot is ^{3}He. The

---

[1] The refractive index of the scintillators is 1.58. By assuming the path length of the signals become about 2 – 3 times longer than the straight lines because of the geometrical effect, the slopes is expected to be about 1/5 – 1/3.

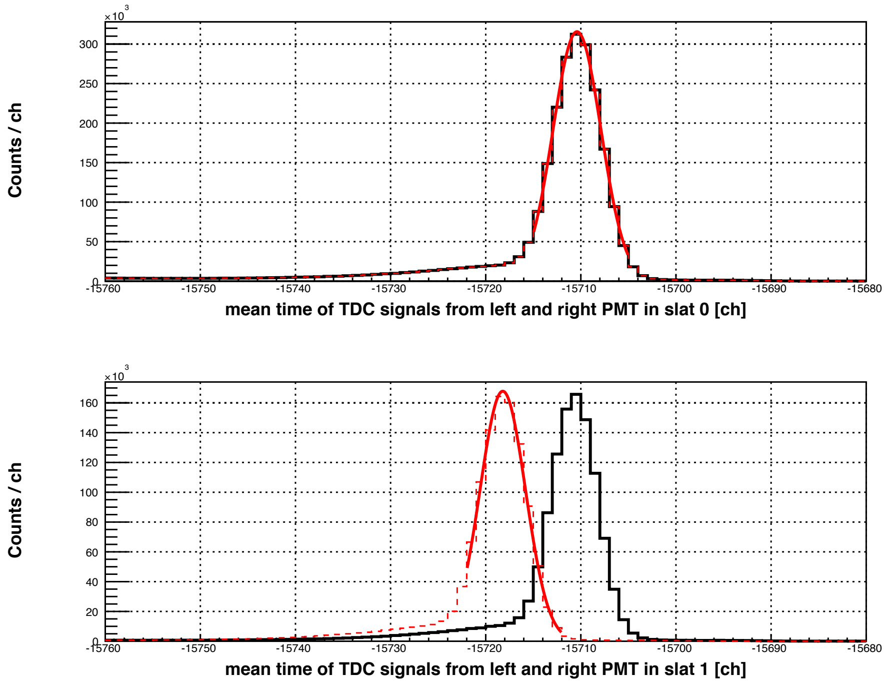

FIGURE 3.1: The averaged values of TDC signals from left and right side PMT of the F5 scintillators with the $p(d,{}^3\mathrm{He})\pi^0$ reaction. The peaks correspond to ^{3}He from p(d, ^{3}He). Top and bottom figures show the signals from slat 1 and slat 2. Red and black lines represent before and after the timing correction, respectively.

ToF$_{\mathrm{F5F7}}$ of ^{3}He depends on the position at F5, because the F5 focal plane is dispersive (dispersion: 62 mm/%) and larger x_{F5Sci} corresponds to higher ^{3}He momentum. The events in the right side are triggered by two protons[2]. The ToF$_{\mathrm{F5F7}}$ of ^{3}He shows clear dependence on the F5 position. The dependence agrees well with expected ToF$_{\mathrm{F5F7}}$ dependence on the ^{3}He momentum.

Left bottom panel of Fig. 3.3 shows the ToF$_{\mathrm{F5F7}}$ distribution. The width of ToF$_{\mathrm{F5F7}}$ for ^{3}He is about 2.5 ns (RMS). The edges of the distribution locate at 285 (left) and 335 (right) ns. The edges are defined by 50 ns gate width of the hardware coincidence trigger circuits. Right top panel of Fig. 3.3 shows the two dimensional plot of corrected ToF$_{\mathrm{F5F7}}$ and x_{F5Sci}. Here, the F5 position dependence is compensated by subtracting the dependence after fitting with a first-order polynomial function. Applying the correction, the distribution of the corrected ToF$_{\mathrm{F5F7}}$ becomes narrower as shown in the right bottom panel of Fig. 3.3, to be 0.8 ns. ^{3}He triggered ToF$_{\mathrm{F5F7}}$ is well separated from that of protons partly observed in the right-hand side of the figure. For identification of the ^{3}He events, we set a gate of interval (304, 314) ns in the corrected $\mathrm{ToF}_{\mathrm{F5F7}}$ for the following analysis, as shown by the dashed black lines in the right panels of Fig. 3.3.

---

[2] In the case, trigger is created by the coincidence between F5 signals from the first proton and F7 signals from the second proton in the next bunch. The x_{F5Sci} is calculated from the F5 signals from the first proton. Larger x_{F5Sci} corresponds to higher momentum of the first proton, and the time difference between signals from first and second protons is enlarged. Therefore, the sign of position dependence of ToF$_{\mathrm{F5F7}}$ is reverse compared with that of ^{3}He.

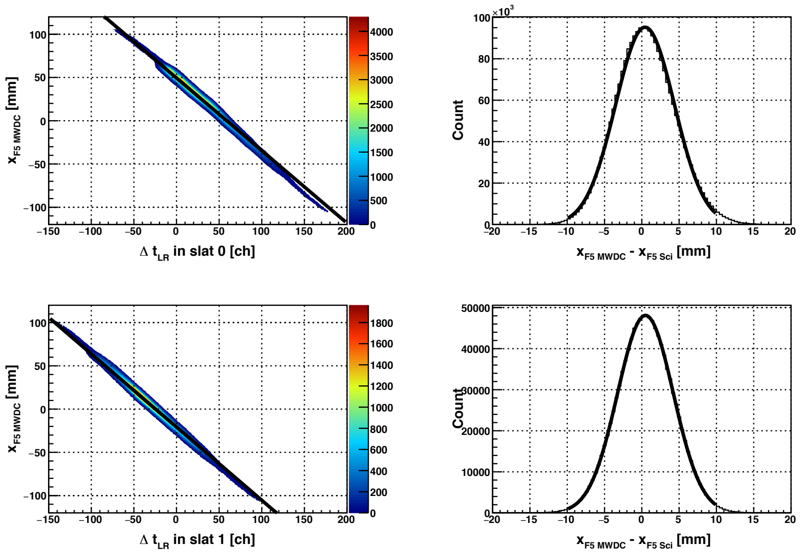

FIGURE 3.2: (Left) Relation between TDC signal difference of left and right PMT of F5 scintillators ($\equiv \Delta \mathrm{t}_{\mathrm{LR}}$) and position deduced from the tracking by MWDCs at F5 ($\equiv x_{\mathrm{F5MWDC}}$). (Right) Difference of x_{F5MWDC} and position deduced from Δt_{LR} ($\equiv x_{\mathrm{F5Sci}}$). Top and bottom figures corresponds to slat 1 and 2 of the F5 scintillators, respectively.

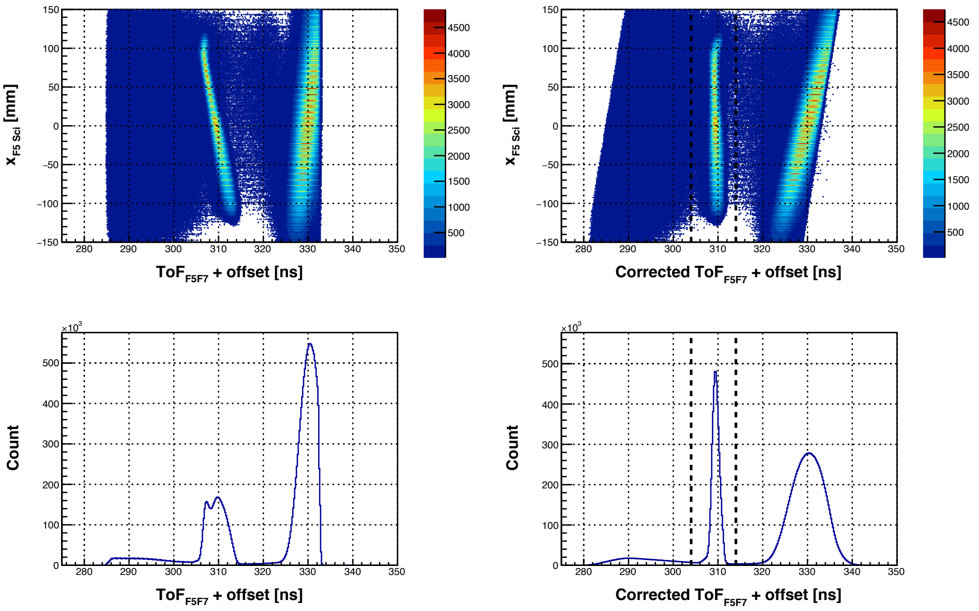

FIGURE 3.3: (Left Top) Two dimensional plot of $\mathrm{ToF}_{\mathrm{F5F7}}$ and x_{F5Sci}. The group in the middle of the plot is ^{3}He. (Left bottom) Projection of left top plot on X axis. (Right Top) Two dimensional plot of the corrected $\mathrm{ToF}_{\mathrm{F5F7}}$ and x_{F5Sci}. The $\mathrm{ToF}_{\mathrm{F5F7}}$ is corrected to compensate for the position dependence. (Right bottom) Projection of left top plot on X axis. The dashed black lines in the right panels represent the gate for the particle identification.

Above selected events by the corrected $\mathrm{ToF}_{\mathrm{F5F7}}$ still include contamination of proton events. Figure 3.4 shows the two dimensional plot of the $\mathrm{ToF}_{\mathrm{F5F7}}$ and the energy loss in the F5 scintillator ($\equiv \Delta E_{\mathrm{SciF5}}$ [3]) (Top), and the $\Delta E_{\mathrm{SciF5}}$ histogram (Bottom) after the ^{3}He event selection by the corrected $\mathrm{ToF}_{\mathrm{F5F7}}$. The blue line in the bottom histogram corresponds to the event selection by the corrected $\mathrm{ToF}_{\mathrm{F5F7}}$ and additional ^{3}He selection by the energy loss in the MWDCs (explained in the next section). The events included in the black lines and not included in the blue lines represents the contamination of the event selection by the corrected $\mathrm{ToF}_{\mathrm{F5F7}}$. The contamination distribution has a peak around 400 ch, which is consistent with the assumption that the contamination comes from the protons. The contamination is estimated to be about 5% of the ^{3}He selected events at this stage.

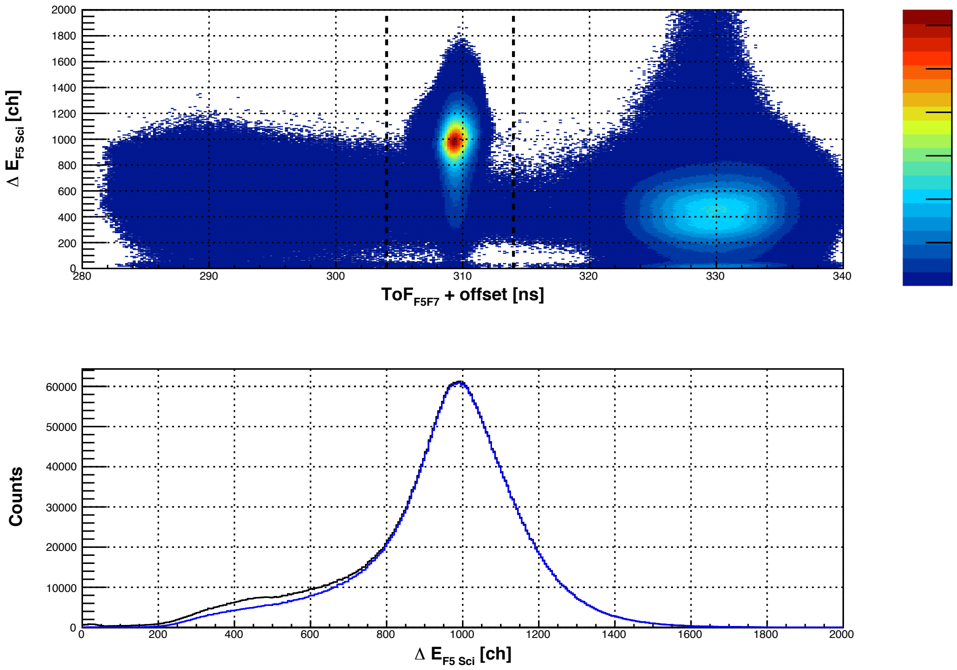

FIGURE 3.4: (Top) Two dimensional plot of the corrected $\mathrm{ToF}_{\mathrm{F5F7}}$ and $\Delta E_{\mathrm{SciF5}}$. The locus in the middle is ^{3}He. The dashed black line shows the gate for ^{3}He event selection. (Bottom) The black line shows $\Delta E_{\mathrm{SciF5}}$ histogram after the event selection by the corrected $\mathrm{ToF}_{\mathrm{F5F7}}$, which is the projection of the top plot on Y axis. The blue line shows $\Delta E_{\mathrm{SciF5}}$ histogram with the additional condition for ^{3}He event selection, the energy loss in MWDCs. The difference between two lines corresponds to the contamination of the event selection by the corrected $\mathrm{ToF}_{\mathrm{F5F7}}$.

---

[3] The energy loss is calculated as the geometric mean of the pulse heights measured by the left and right PMS in each slat.

3.1.2 Energy loss in MWDCs at the F5 focal plane

In order to further reduce the contaminations from the background protons at a level of about 5%, we make use of the energy loss measured by the MWDCs. The ratio of the energy loss between the proton and the ^{3}He is calculated to be 1 : 7.1. This difference of pulse heights is measured as the time difference between leading and trailing points at the threshold levels of the analog pulses, or Time over Threshold (ToT). Measurement of the ToT in each plane (15 planes in total) is equivalent to the measurement of the energy loss by 15 times. By counting the number of planes detecting large energy loss, ^{3}He events can be selected reliably.

Figure 3.5 shows the ToT distribution detected by the upstream and downstream MWDCs in a production run with ^{122}Sn target under the condition that the F5 scintillators detect a single hit. The absolute scale of the ToT differ between two MWDCs because of the difference of the time constant of the preamplifiers (16 ns for the upstream and 80 ns for the downstream). The black lines in the figures correspond to the measured all signals. The sky-blue and red lines correspond to the ^{3}He selected events and not-selected events by $\mathrm{ToF_{F5F7}}$, respectively. The blue lines represent the signals used for the tracking in the case that the tracking is succeeded. The red and blue lines correspond to the ToT distributions from the proton and the ^{3}He, respectively.

We set the ^{3}He selection thresholds of the ToT to be 40 ch for the upstream and 100 ch for the downstream MWDCs as indicated by the black vertical lines and select ^{3}He-like signals. Here we count the number of planes detecting the ^{3}He-like signals as $N_{\mathrm{plane}}^{^3\mathrm{He}}$ for each event. Figure 3.6 shows the distribution of the $N_{\mathrm{plane}}^{^3\mathrm{He}}$. The blue line corresponds to the ^{3}He events selected by the $\mathrm{ToF_{F5F7}}$. The red line represents the proton events, which is defined as the event with at least one signal in "proton" region (320 – 340) in $\mathrm{ToF_{F5F7}}$ histogram and no signals in the ^{3}He gate. We set $N_{\mathrm{plane}}^{^3\mathrm{He}} \geq 14$ as a condition to identify ^{3}He by the ToT analysis of the MWDCs.

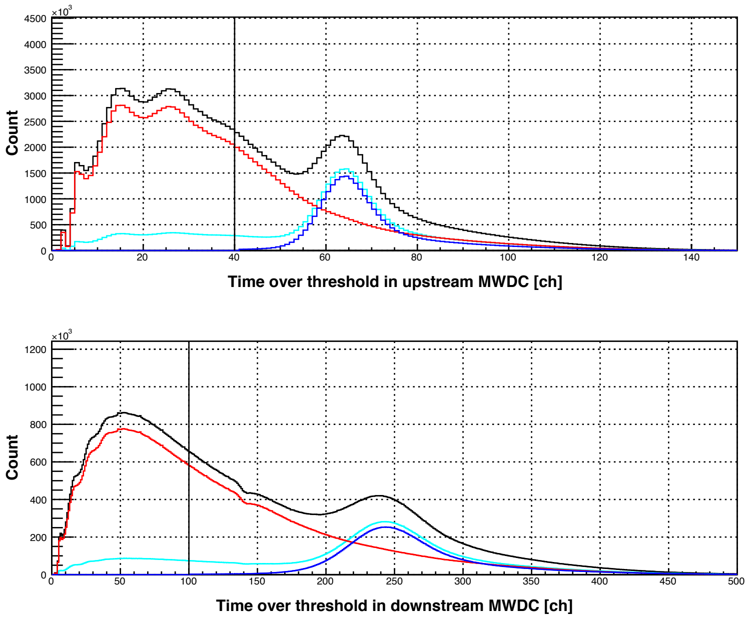

FIGURE 3.5: Time over threshold distribution of upstream MWDC (Top) and of downstream MWDC (Bottom) in a production run with ^{122}Sn target with requiring a single hit event in the F5 scintillators. The black lines correspond to the all signals. The sky-blue and red lines correspond to the ^{3}He selected events and not-selected events by ToF$_{\mathrm{F5F7}}$, respectively. The blue lines represent the signals used for the tracking in the case that the tracking is succeeded.

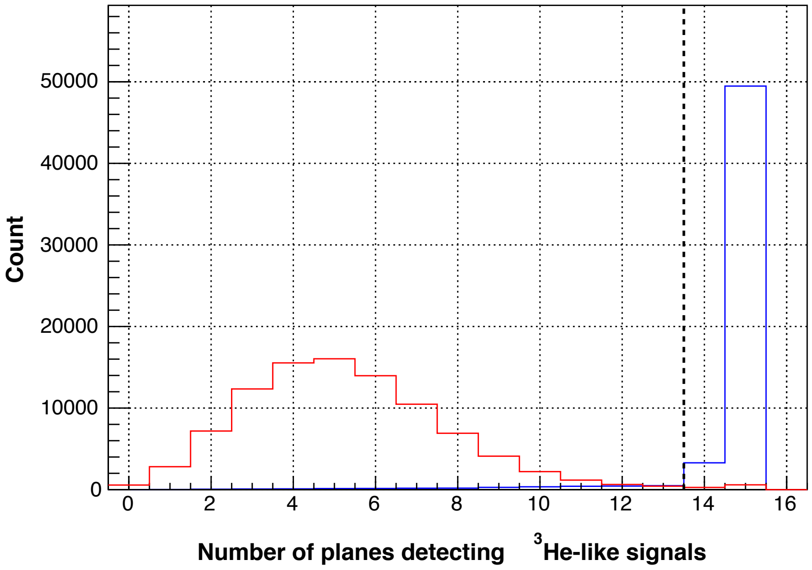

FIGURE 3.6: Number of planes detecting ^{3}He-like signals ($N^{^{3}\mathrm{He}}_{\mathrm{plane}}$). The blue line corresponds to the ^{3}He events chosen by the ToF$_{\mathrm{F5F7}}$. The red line represents the "proton" events, which is defined as the event with at least one signal in the "proton" region (320 – 340) in ToF$_{\mathrm{F5F7}}$ histogram and no signals in the ^{3}He gate in the corrected ToF$_{\mathrm{F5F7}}$ histogram.

3.1.3 Event timing with respect to radio frequency of SRC

To improve and evaluate the particle identification capabilities, the time difference between timing signals at F5 and the radio frequency (RF) timing of SRC $\equiv \Delta t_{\mathrm{SciF5-RF}}$ is also analyzed. The primary beam provided by the SRC has micro time structures in time with the cyclic frequency of 13.7 MHz, which corresponds to the frequency of the accelerator voltage of the SRC. Figure 3.7 shows a timing diagram of particle transportation in BigRIPS with the cyclic structures. The solid lines correspond to the particles produced by a primary beam in each micro structure. The dashed lines correspond to those by the primary beam in so-called "half bunch", which means that the deuteron beam is accelerated with a half cycle deviated phase of the acceleration. The "half bunch" events were estimated to be about 1% of all events. These events should be rejected from the analysis, because the energy may be deviated.

A signal synchronized to the RF was measured in the experiment. The left top and bottom panels of Fig. 3.8 show the two dimensional plots of the $\Delta t_{\mathrm{SciF5-RF}}$ and the x_{SciF5}, and the $\Delta t_{\mathrm{SciF5-RF}}$ distribution in a production run. As shown in the figure, the time structure of $\Delta t_{\mathrm{SciF5-RF}}$ also becomes cyclic. The distributions around $\Delta t_{\mathrm{SciF5-RF}} = -75$, 0 and $+75$ ns correspond to ^{3}He, while the distributions around $\Delta t_{\mathrm{SciF5-RF}} = -25$ and 50 ns correspond to protons.

$\Delta t_{\mathrm{SciF5-RF}}$ and x_{SciF5} has strong correlation scinse $\Delta t_{\mathrm{SciF5-RF}}$ reflects the time of flight between the F0 and F5 focal planes. $\Delta t_{\mathrm{SciF5-RF}}$ of ^{3}He at $x_{\mathrm{F5Sci}} = 60$ mm, which correspond to about 1.0% higher momentum, is 3.4 ns smaller compared with that at $x_{\mathrm{F5Sci}} = 0$ mm. The result agrees fairly well with calculated value, 2.9 ns. Position dependence of $\Delta t_{\mathrm{SciF5-RF}}$ of proton is also confirmed to be consistent with the calculation: 1.6 ns in the measurement and 1.7 ns in the calculation.

Similar to the case for $\mathrm{ToF}_{\mathrm{F5F7}}$, $\Delta t_{\mathrm{SciF5-RF}}$ is corrected by third-order polynomial function to compensate for the position dependence as shown in the middle panels of Fig. 3.8. To correctly treat the cyclic structures, $\Delta\tilde{t}_{\mathrm{SciF5-RF}}$ is defined as the remainder of the corrected $\Delta t_{\mathrm{SciF5-RF}}$ divided by the cycle of the RF, 75 ns. The two dimensional plot of $\Delta\tilde{t}_{\mathrm{SciF5-RF}}$ and x_{SciF5}, and the $\Delta\tilde{t}_{\mathrm{SciF5-RF}}$ distribution are shown in the right panels of Fig. 3.8.

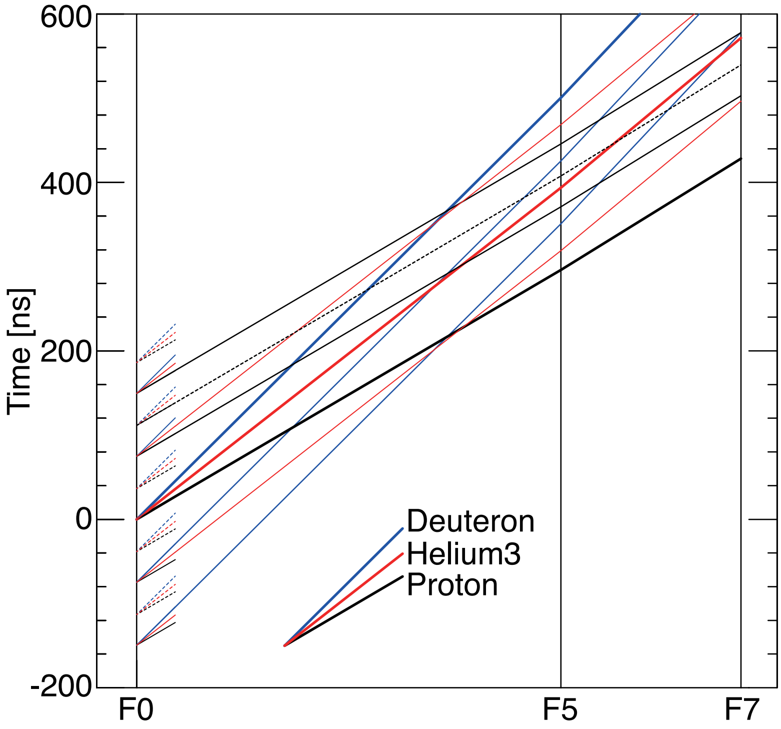

FIGURE 3.7: A timing diagram of particles passing through the BigRIPS. Lines are showing the particles in RF bunches and broken lines those in half-cycle-shifted bunches.

To see the time structures of signal ^{3}He and background, an enlarged view of $\Delta\tilde{t}_{\mathrm{SciF5-RF}}$ distribution in a production run is shown in Fig. 3.9. The black line represents all signals. The blue line corresponds to the signals in the events identified as ^{3}He by the ToF$_{\mathrm{F5F7}}$ and the $N^{^3\mathrm{He}}_{\mathrm{plane}}$. The explanation of each component is given in the figures. The peak at $\Delta\tilde{t}_{\mathrm{SciF5-RF}} \simeq -4$ ns corresponds to ^{3}He originating in the $(d, {}^3\mathrm{He})$ reaction at the target. The width of the peak is about 1 ns (RMS).

A ^{3}He produced in the beam dump is also observed in the distributions. The primary beam was dumped in the first dipoles, D1. In the case that ^{3}He is produced at the beam dump, the calculated time of flight from F0 to F5 becomes 10 ns faster than the signal ^{3}He, which agrees well with the observed distribution near $\Delta\tilde{t}_{\mathrm{SciF5-RF}} \simeq -14$ ns. To choose the signal ^{3}He from the target, the gate from -7 to 4 ns for $\Delta\tilde{t}_{\mathrm{SciF5-RF}}$ is adopted.

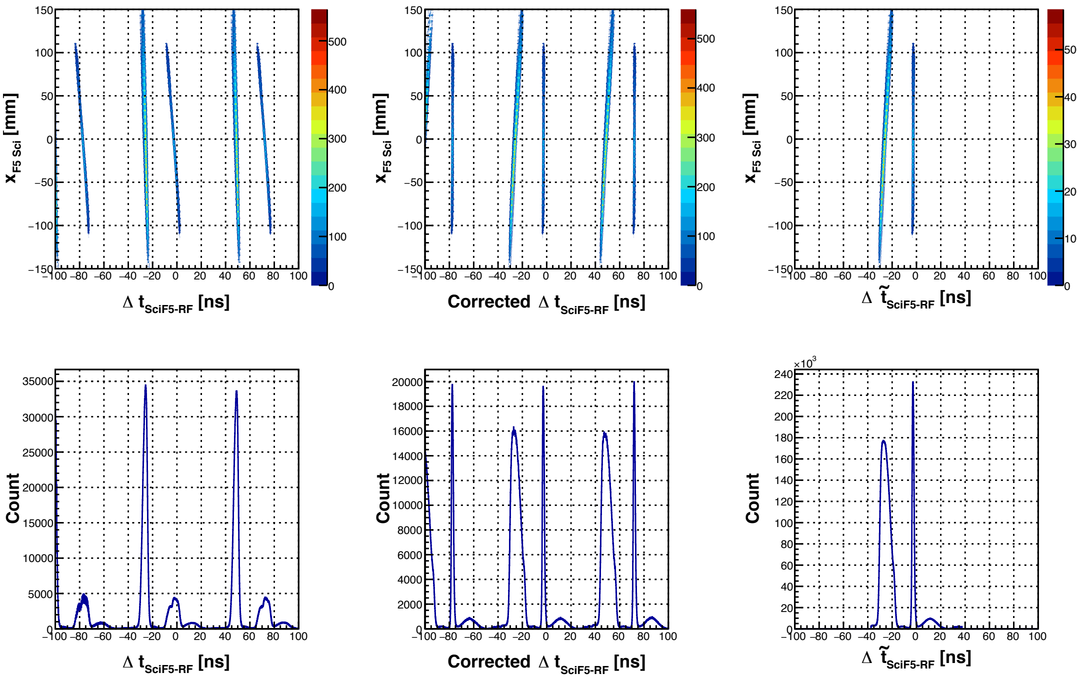

FIGURE 3.8: (Left Top) Two dimensional plot of $\Delta t_{\mathrm{SciF5-RF}}$ and x_{F5Sci}. The locus with $\Delta t_{\mathrm{SciF5-RF}} = -75$, 0 and 75 ns correspond to ^{3}He. (Left bottom) Projection of left top plot on X axis. (Middle Top) Two dimensional plot of the corrected $\Delta t_{\mathrm{SciF5-RF}}$ and x_{F5Sci}. The $\Delta t_{\mathrm{SciF5-RF}}$ is corrected to eliminate the position dependence. (Middle Bottom) Projection of middle top plot on X axis. (Right Top) Two dimensional plot of the remainder of the corrected $\Delta t_{\mathrm{SciF5-RF}}$ divided by the cycle of RF ($\equiv \Delta\tilde{t}_{\mathrm{SciF5-RF}}$) and x_{F5Sci}. (Right Bottom) Projection of right top plot on X axis.

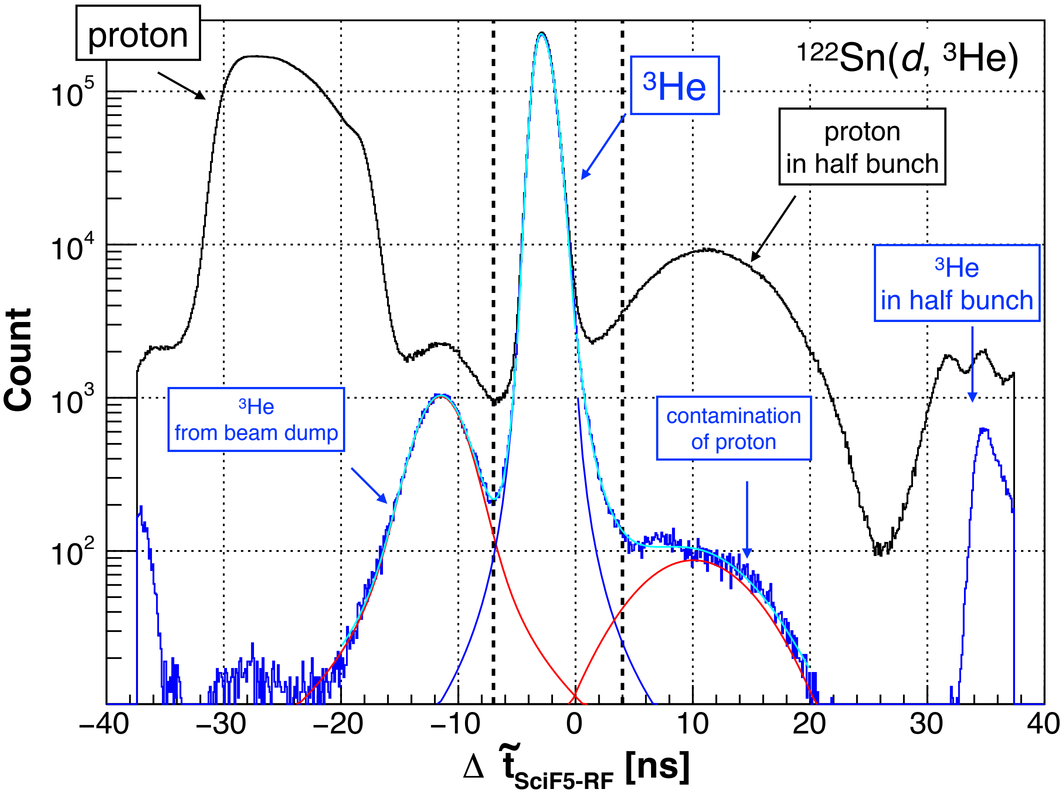

FIGURE 3.9: Enlarged view of $\Delta\tilde{t}_{\mathrm{SciF5-RF}}$ distribution in a production run with the ^{122}Sn target. The explanation of each components are represented in the figure. The sky-blue line is the fitting result of the structures of the events identified by the ToF$_{\mathrm{F5F7}}$ and the $N^{^3\mathrm{He}}_{\mathrm{plane}}$. The blue line is a sub component of the fitting function corresponding to the signal ^{3}He. The left and right red lines are sub components of the fitting function corresponding to the ^{3}He from the beam dump and contamination of protons, respectively. The definition of the fitting function is written in the text.

3.1.4 Evaluation of contamination and efficiency of particle identification

Here the contamination and efficiency, and their position dependence of particle identification by ToF$_{\mathrm{F5F7}}$, $N^{^3\mathrm{He}}_{\mathrm{plane}}$ and $\Delta\tilde{t}_{\mathrm{SciF5-RF}}$ are evaluated. The contamination is evaluated by a fit of the $\Delta\tilde{t}_{\mathrm{SciF5-RF}}$ distribution in the events identified as ^{3}He by ToF$_{\mathrm{F5F7}}$ and $N^{^3\mathrm{He}}_{\mathrm{plane}}$ as shown in Fig. 3.9. The fitting function is represented as sky-blue lines. The function is composed of four regions: (i) Voigtian[4] corresponding to ^{3}He from beam dump plus Voigtian corresponding to signal ^{3}He (−20 to −5 ns), (ii) Voigtian corresponding to signal ^{3}He (−5 to −3 ns), (iii) Voigtian corresponding to signal ^{3}He (−3 to 0 ns) and (iv) Gaussian corresponding to contamination from proton plus Voigtian tail corresponding to signal ^{3}He (0 to 20 ns). Each Voigtian of signal ^{3}He in four regions has own σ and Γ, and share the center of the distributions. The red lines represents the Voigtian corresponding to ^{3}He from the beam dump in region (i) and Gaussian corresponding to contamination from proton in region (iv).

---

[4] A function of convolution of a Lorentzian and a Gaussian distributions.

The contamination of ^{3}He from the beam dump and the protons are evaluated by the integral of these functions in the gate indicated by black lines. As a result, the contamination of ^{3}He produced in the beam dump is 0.06% of total amount of the signal ^{3}He and that from the proton is 0.03%, which are much smaller than the statistical errors of the excitation spectra of ^{121,116}Sn.

The position distributions of the contaminations are evaluated from the x_{SciF5} distributions in $\Delta\tilde{t}_{\mathrm{SciF5-RF}} = -25$ to -12 ns region (^{3}He from the beam dump) and in $\Delta\tilde{t}_{\mathrm{SciF5-RF}} = 8$ to 20 ns region (half bunch proton). The distributions are shown in Fig. 3.10. No distinct structures are seen in both distributions.

The efficiency of the ^{3}He gate of $\Delta\tilde{t}_{\mathrm{SciF5-RF}}$ is also evaluated from the fitting of $\Delta\tilde{t}_{\mathrm{SciF5-RF}}$ distributions. The blue lines represent the Voigtian of signal ^{3}He in regions (i) to (iv). The efficiency of $\Delta\tilde{t}_{\mathrm{SciF5-RF}}$ is evaluated by integration of these functions out of the gate. The evaluated efficiency of the gate of $\Delta\tilde{t}_{\mathrm{SciF5-RF}}$ is 99.95 %, which is high enough and the inefficiency of the gate is negligible.

The efficiency of the particle identification (pID) by the $\mathrm{ToF}_{\mathrm{F5F7}}$ and the $N^{^3\mathrm{He}}_{\mathrm{plane}}$ are evaluated from the data of $p(d, {}^3\mathrm{He})\pi^0$ in a calibration run with the polyethylene target. In the run S/N ratio is better by an order of two compared with that of the production runs. Therefore the contamination of protons can be ignored. The efficiency of the pID by $\mathrm{ToF}_{\mathrm{F5F7}}$ is evaluated as the ratio of the events with ^{3}He identified by $\mathrm{ToF}_{\mathrm{F5F7}}$ to the ^{3}He events identified by $\Delta\tilde{t}_{\mathrm{SciF5-RF}}$ and $N^{^3\mathrm{He}}_{\mathrm{plane}}$. The pID efficiency by $N^{^3\mathrm{He}}_{\mathrm{plane}}$ is also evaluated as the ratio of ^{3}He events identified by $N^{^3\mathrm{He}}_{\mathrm{plane}}$ to the ^{3}He events identified by $\Delta\tilde{t}_{\mathrm{SciF5-RF}}$ and $\mathrm{ToF}_{\mathrm{F5F7}}$.

The pID efficiencies are evaluated for each x_{SciF5} and the results are shown in Fig. 3.11. The left and middle panels show the position dependence of the pID efficiency by $\mathrm{ToF}_{\mathrm{F5F7}}$ and $N^{^3\mathrm{He}}_{\mathrm{plane}}$. The total pID efficiency by is calculated as the product of the pID efficiency by $\mathrm{ToF}_{\mathrm{F5F7}}$ and $N^{^3\mathrm{He}}_{\mathrm{plane}}$ as shown in the right panel. The evaluated efficiency is fitted by a fourth-order polynomial function.

In conclusion of the particle identification, signal ^{3}He is identified clearly by (i) time of flight between F5 and F7 focal planes ($\mathrm{ToF}_{\mathrm{F5F7}}$), (ii) the energy loss measured by MWDCs ($N^{^3\mathrm{He}}_{\mathrm{plane}}$), and (iii) the time difference between the detecting time at the F5 focal plane and the radio frequency of the SRC ($\Delta\tilde{t}_{\mathrm{SciF5-RF}}$). The evaluated contamination by the pID is negligibly small (less than 0.06%) compared with the statistical errors of the excitation spectra of ^{121,116}Sn and does not produce distinct position dependence.

Therefore the effect of the contamination is ignored in the following analysis. The position dependence of the efficiency is also evaluated as shown in the right panel of Fig. 3.11. The efficiency is more than 98.5% for all positions, and the dependence on the position is small enough (within 0.5%). The evaluated position dependence of the efficiency is taken into account in the following analysis.

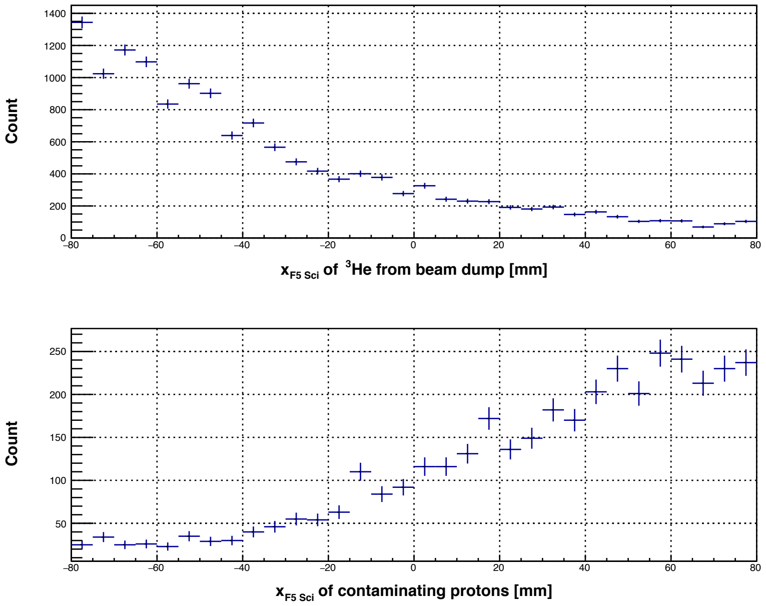

FIGURE 3.10: (Top) The x_{SciF5} distribution with $\Delta\tilde{t}_{\mathrm{SciF5-RF}} = -25$ to -12, which corresponds to the ^{3}He from beam dump. (Bottom) The x_{SciF5} distribution with $\Delta\tilde{t}_{\mathrm{SciF5-RF}} = 8$ to 20, which corresponds to the contamination of proton. In both distributions, no distinct structures are observed.

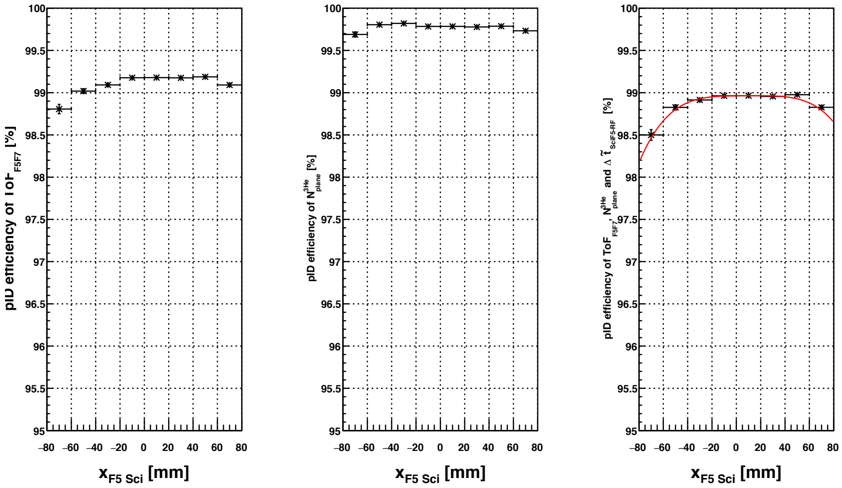

FIGURE 3.11: Position dependence of the PID efficiency by $\mathrm{ToF}_{\mathrm{F5F7}}$ (Left), $N^{^3\mathrm{He}}_{\mathrm{plane}}$ (Middle) and the logical product (Right). No remarkable strucutre is observed.

3.2 Tracking of ^{3}He

In this section the track reconstruction of the ^{3}He trajectories by the MWDC is explained. The events including the ^{3}He are selected as described in the previous sections. The ^{3}He trajectories are reconstructed by using the ToT-identified 3He-like signals described in Sect. 3.1.2 for detail. From the evaluation of the plane resolution, tracking efficiency and their position dependences, it is conformed that there are no significant position dependence on the tracking. After these analysis, we smeared the obtained spectrum to ensure the uniformity of the position. Note that even after the position smearing, the precise information of the angle of the track is kept, which is used for the optical correction (Sect. 3.3).

3.2.1 Conversion function from drift time to drift length

For the tracking with the MWDCs, here we deduce a conversion function from a measured drift time to a drift length. The drift time is measured as time difference between MWDC signals and the F5 scintillator signals. The conversion function is deduced based on the assumption that the particle number in a cell (a space between wires) distributes uniformly by averaging the distribution of all wires in one plane.
Figure 3.12 shows the time difference (left panel) and conversion function (right panel) for ^{3}He detected in the most upstream plane of the upstream MWDC. The function is determined to reproduce uniform distribution, and is prepared for each plane. Note that a larger leading time corresponds to a small drift length, because the signals from the F5 scintillators were used as common stop signals for the TDC.

3.2.2 Fitting of particle trajectories

The particle trajectories are reconstructed by integrating the positions measured at each plane of the MWDCs. Measured positions for ^{3}He-like signals selected by the ToT method are fitted by a line using χ^2 minimization, and the track positions and directions are deduced.

Figure 3.13 shows typical examples. The top and the bottom graphs in each panel correspond to the upstream and the downstream MWDCs. The horizontal and vertical axes indicate the horizontal position and the position at beam-direction coordinate, respectively. Each of the circles represents the position of fired wire and the radius does the estimated drift length. Red circles is the signals with ToT under ^{3}He threshold, while the blue and sky-blue with ToT over the ^{3}He threshold, defined as ^{3}He-like signals.

About 80% of ^{3}He event contain only 1 hit in the F5 scintillator, which is represented by the top panel of Fig. 3.13.

For each plane, one ^{3}He-like signal, whose ToT is over the threshold, is selected and the χ^2 is evaluated. The χ^2 of all combinations of ^{3}He-like signals are evaluated and a combination with the minimum χ^2 is chosen as the ^{3}He trajectory. As a result, the trajectory is reconstructed as the blue line in the figure. The ^{3}He-like signals used for the tracking are represented with blue circles. About 20% of ^{3}He events are accompanied by an accidental proton simultaneously injected to the MWDC, which is represented by the bottom panel in Fig. 3.13. Even in such events, with ToT information the ^{3}He trajectory can be reconstructed clearly as shown. Note that the χ^2 is calculated based on the resolution of each plane. The resolution is estimated as in the following sections. The tracking and estimation of the resolution is repeated iteratively.

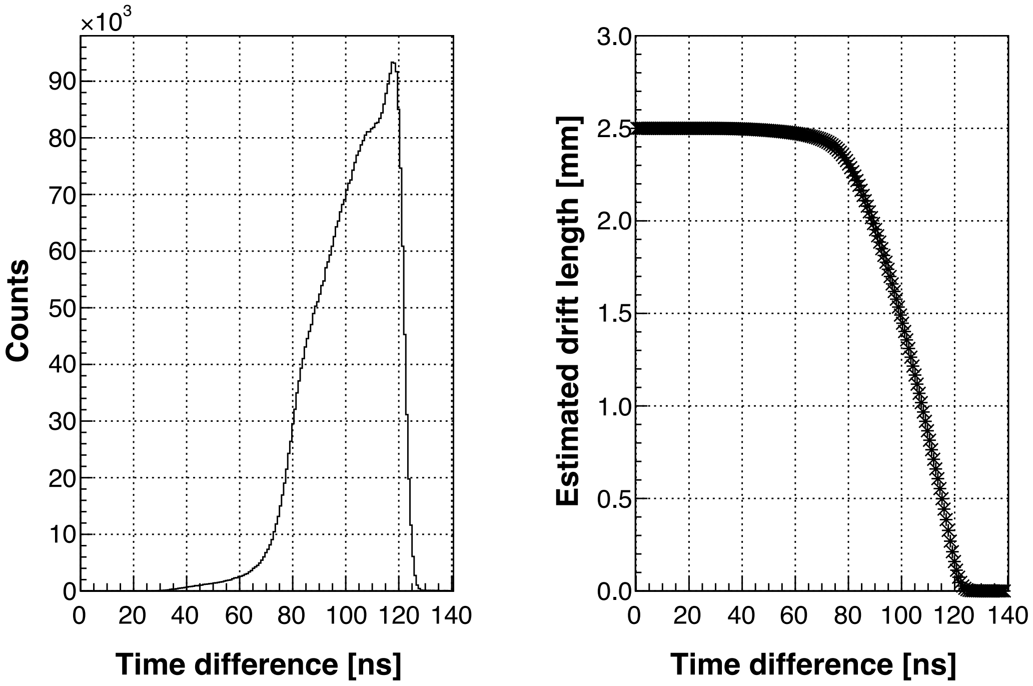

FIGURE 3.12: (Left) The distribution of time difference between MWDC signals and the F5 scintillator signals. (Right) Conversion function from the time difference to drift length of X plane of upstream MWDC.

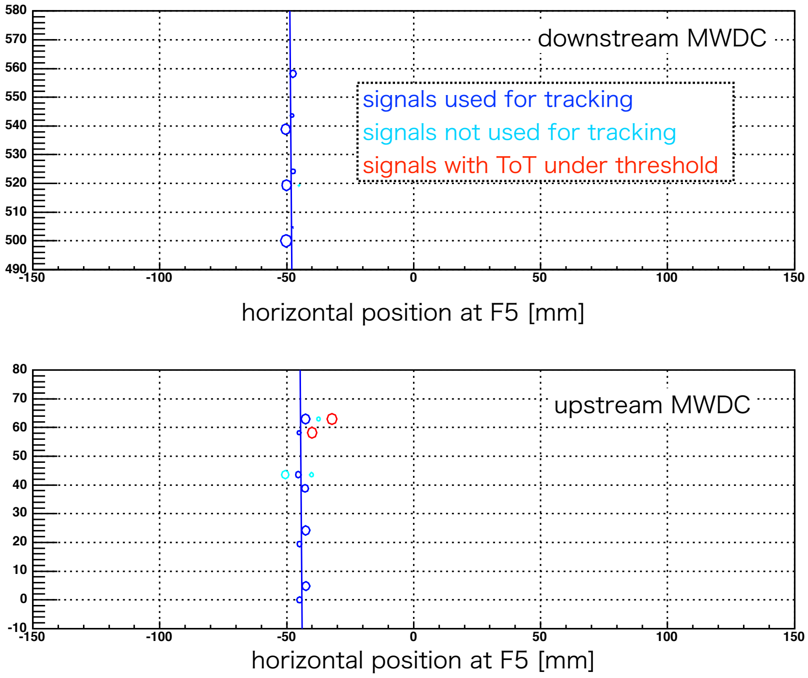

(A) An example of tracking by MWDC with single hit of ^{3}He

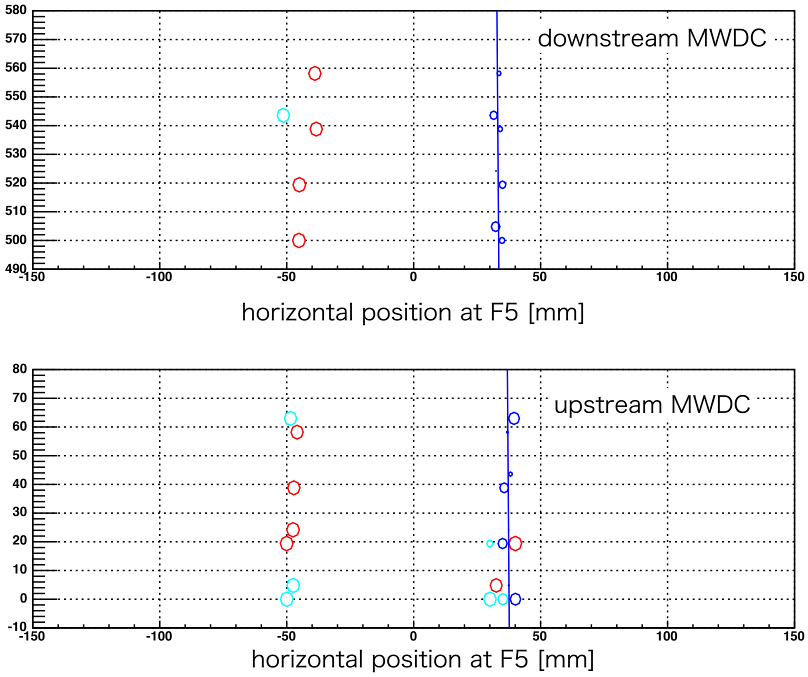

(B) An example of tracking by MWDC with double hit of ^{3}He and proton

FIGURE 3.13: Examples of tracking by MWDCs. The top and the bottom graphs in each panel correspond to the upstream and the downstream MWDCs. The X and Y axes indicate the horizontal position and the position at beam-direction coordinate, respectively. Each of the circles represents the position of fired wires and radius does the estimated drift length. About 80% of ^{3}He events contain only signals from ^{3}He as a example in the top figure, while 20% of ^{3}He events contain signals from ^{3}He and proton as a example in the bottom figure.

3.2.3 Wire offset correction

Deviation of each wire position is measured and corrected by using an exclusive residual distribution explained in the next subsection. The residual distribution is defined for each wire reflecting the offset of the wire position brought-in at the fabrication.

Figure 3.14 shows the measured wire offset of the X1 plane in the upstream MWDC. The estimated wire offset is taken into account in the tracking analysis. After the correction, the residues are confirmed to be smaller than 0.02 mm for all wires in the region of interest, wire number 8 to 40, corresponding to -80 to 80 mm in x. The value of 0.02 mm is small enough compared with the tracking resolution of each plane.

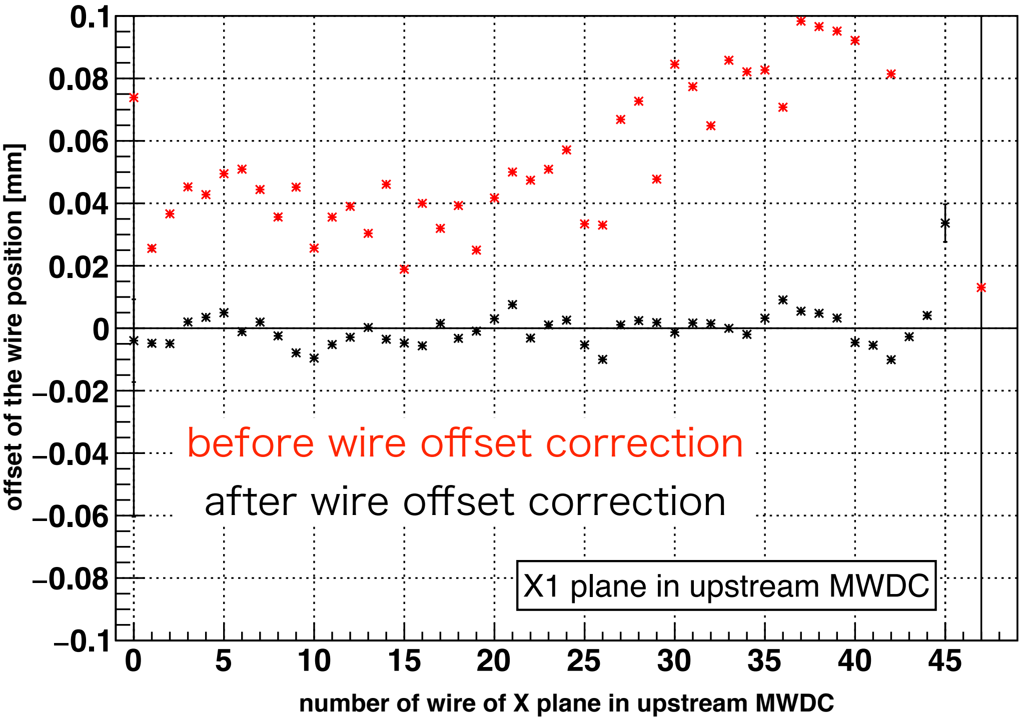

FIGURE 3.14: Measured offset of wires in the X1 plane of the upstream MWDC. The offset is well controlled to be < 0.1 mm, and after software correction, the offset becomes negligible.

3.2.4 Tracking resolution

The residual distributions are also used for the evaluation of the tracking resolution. The residual is defined by subtracting the estimated drift length from the distance between the fitted trajectory and the sense wire. The residual for each plane is calculated for trajectories deduced in two methods: (i) the position information in the corresponding plane is used in the fitting and (ii) the information is not used in the fitting. The residual deduced by method (i) is defined as inclusive residual, while that deduced by method (ii) as exclusive residual. Figure 3.15 shows the inclusive and exclusive residual distribution on X1 plane in the upstream MWDC measured with the ^{122}Sn(d, ^{3}He) reaction.

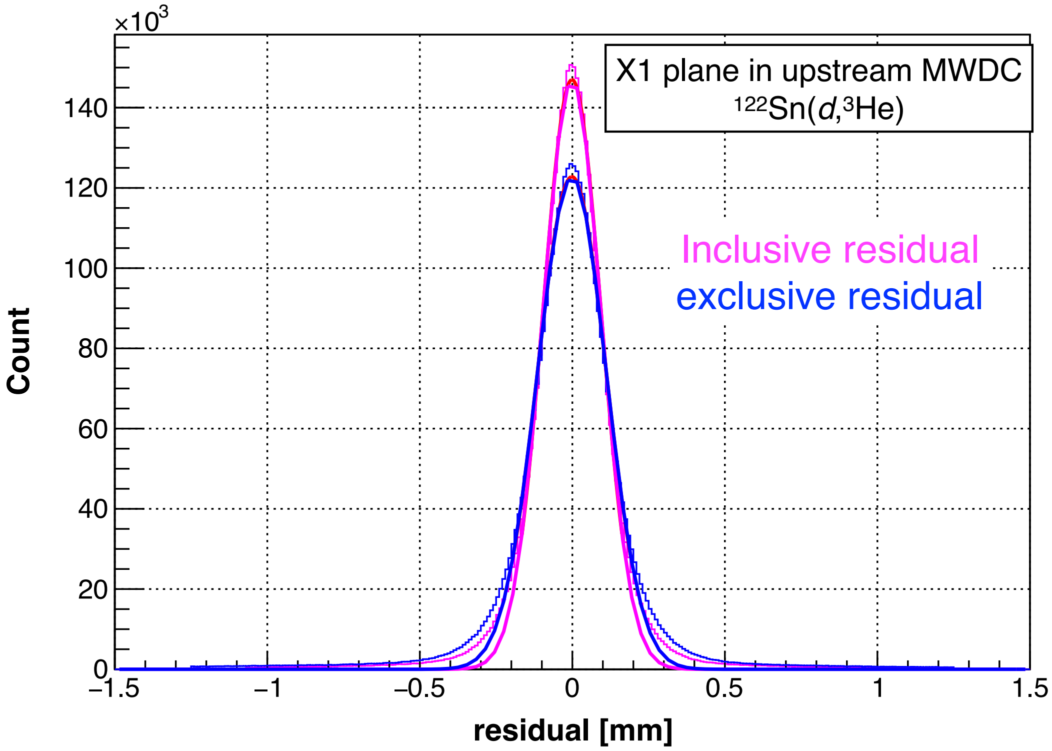

FIGURE 3.15: Residual distribution of the tracking by MWDC on the X1 plane in upstream MWDC measured in the production run with ^{122}Sn target after wire offset correction. The magenta and blue distribution correspond to inclusive and exclusive residual, respectively.

The tracking resolution is evaluated from the residual distribution. The standard deviation of the inclusive and exclusive residual distribution are defined as $\sigma_{\text{inclusive}}$ and $\sigma_{\text{exclusive}}$. It is known that the plane resolution, $\sigma_{\text{resolution}}$, is calculated [35] as

$$\sigma_{\text{resolution}} = \sqrt{\sigma_{\text{inclusive}} \times \sigma_{\text{exclusive}}}. \tag{3.1}$$

The evaluated plane resolution is shown in Fig. 3.16. The plane resolution distributes between 0.1 and 0.2 mm. The corresponding trajectory resolution is ≈ 0.04 mm for the horizontal position, 0.3 mrad for the horizontal angle and 0.7 mrad for the vertical angle. These values are sufficiently small compared with other factors; ≈ 1 mm from the primary beam momentum spread and ≈ 2 mrad from multiple scattering by the F5 materials. To confirm the uniformity, the resolution is evaluated for each wire in each plane as shown in Fig. 3.17. As a result, the resolution of each wire is confirmed to be distributed within 0.1 - 0.25 mm. As shown in the figure, there are several wires with worse resolution than others, which may have influence on the position dependence of tracking efficiency or tracking resolution. However, it is confirmed that there are no significant position dependence on the tracking efficiency, as shown in the following section. Besides, the obtained horizontal position is smeared by a Gaussian distribution with the σ of 0.5 mm to ensure the uniformity of the histogram as explained in Sect. 3.2.6. After the smearing of the tracks, the resolution in each position is dominated by the smearing factor, and the small deviation of the wire resolution is safely ignored.

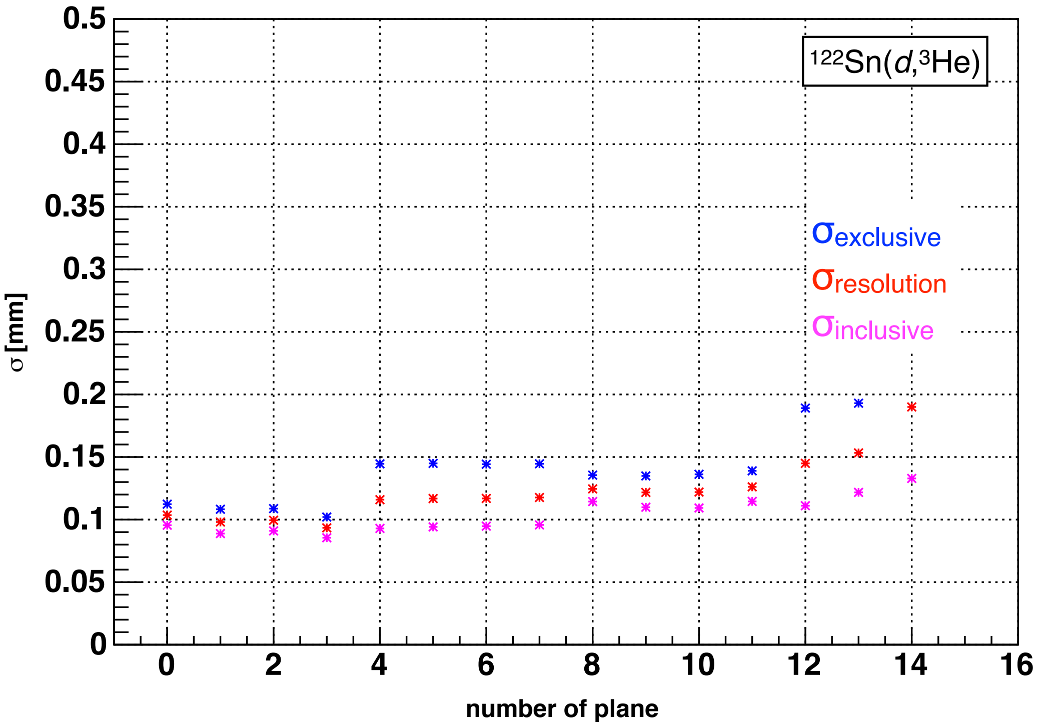

FIGURE 3.16: Estimated track resolution for each MWDC plane. The resolution is well controlled to be < 0.2 mm.

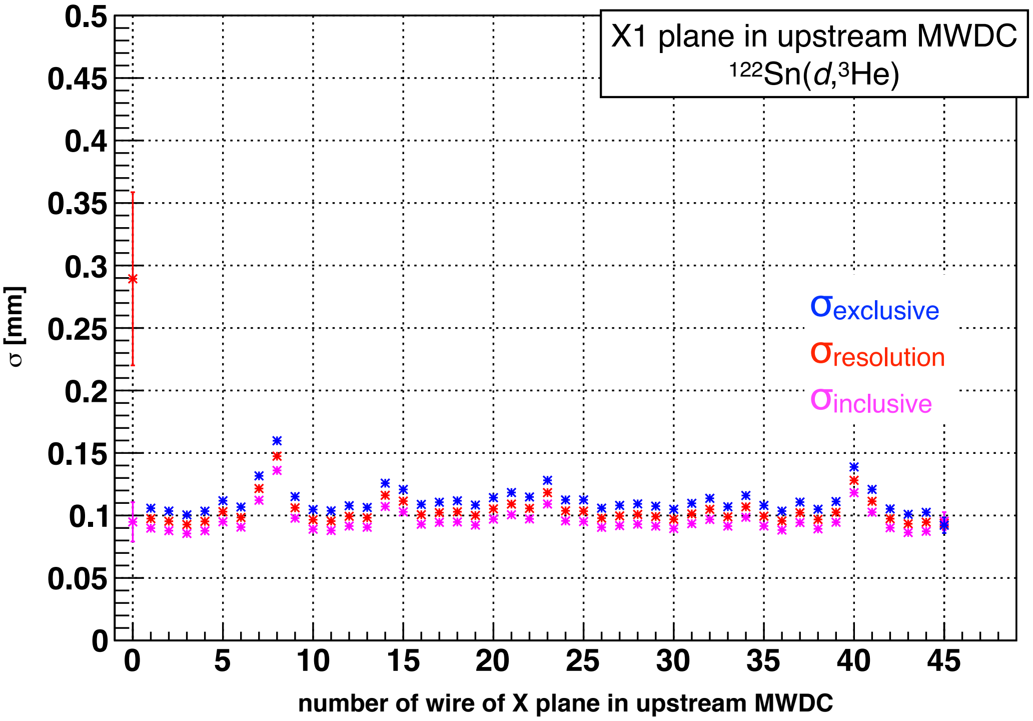

FIGURE 3.17: Position (wire) dependence of the tracking resolution for the X1 plane of the upstream MWDC. The slightest wire-dependence of the resolution is well controlled to be < 0.15 mm for the whole wires except for the left edge.

3.2.5 Tracking efficiency

The goodness of the tracking is evaluated by reduced χ^2 of the fitting. Figure 3.18 shows the obtained reduced χ^2 distribution in a production run with the ^{122}Sn target. The number of degree of freedom (ndf) is 10 or 11, which depends on the $N^{^3\mathrm{He}}_{\mathrm{plane}}$. In the following analysis, we require reduced χ^2 to be less than 20. Note that the distribution has longer tail than ideal reduced χ^2 with ndf of 10 or 11. That is because the residual distribution has a longer tail than a Gaussian distribution. Under this condition, the tracking efficiency is evaluated in the production run with the ^{122}Sn target, as a function of the position at the F5 focal plane as shown in the Fig. 3.19. The efficiency is calculated as the ratio of successful tracking to the ^{3}He events, which is explained in Sect. 3.1. The efficiency is higher than 98.7% in whole region of interest, and is sufficiently homogenous with $< 0.2\%$ level, which is negligible compared with the statistical errors of the excitation spectra of ^{121,116}Sn.

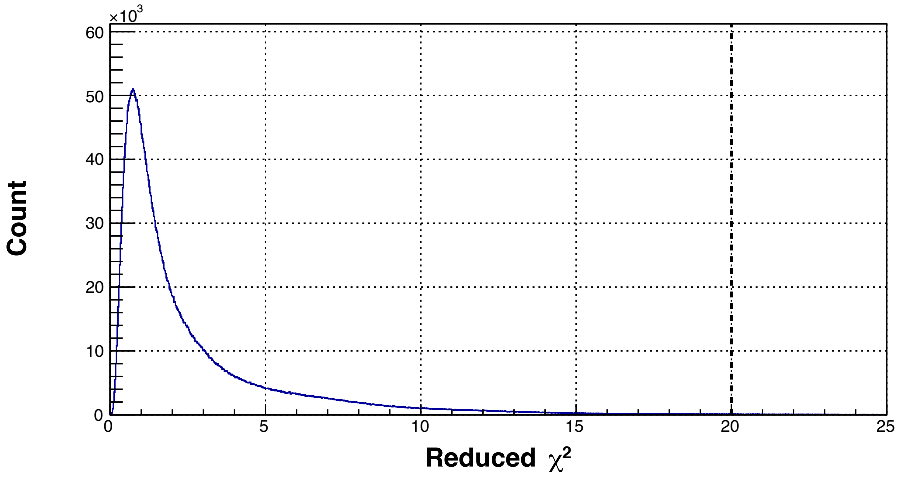

FIGURE 3.18: Reduced χ^2 distribution of the fitting in a production run with ^{122}Sn target. The ndf is 10 or 11. The events less than the vertical dashed line are used for the analysis.

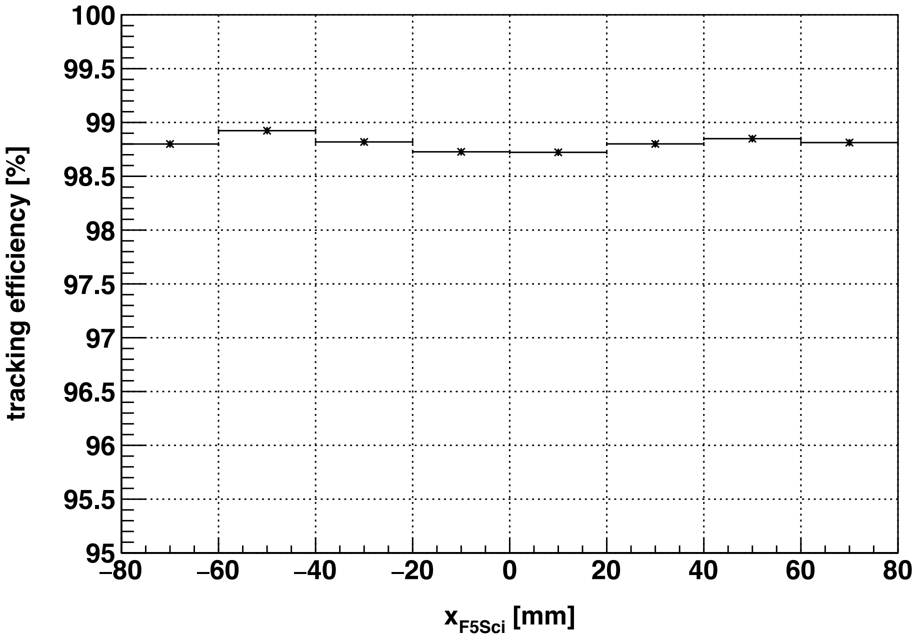

FIGURE 3.19: Position dependence of the tracking efficiency. The efficiency is controlled to be > 98.7% level over the whole region of interest and is sufficiently homogenous with < 0.2% level.

3.2.6 Smearing of the position spectra

The obtained horizontal position is smeared by a Gaussian distribution with a standard deviation of 0.5 mm to ensure the uniformity against the wire structures of the MWDCs. The top panel of Fig. 3.20 shows the position histogram on the X1 plane in the downstream MWDC, which is closest to the focused plane in a production run with the ^{122}Sn target. As observed in the figure, comb-like structures are seen in every 5 mm. The period corresponds to the wire structures of MWDCs. To suppress the effect of the structures, we introduce smearing using a Gaussian distribution with a standard deviation of 0.5 mm[5]. The bottom panel shows the position distribution after the smearing is introduced, where the comb-like structures disappear. To confirm the uniformity, we performed a linear fitting on the histograms in the range of (20, 50). As a result, the value of χ^2 of the fitting becomes reasonable after the smearing is introduced, while the value without the smearing is far from the value expected only with statistical fluctuations.

According to a simplified simulation [36], these ‘comb-like structures appear even with the ideal condition. The origin of the “combs” are assumed to be that the reconstructed drift length in each plane is limited inside the cell. The limitation makes the singularity of the conversion function around the edges. The detail is described in the Appendix A. In the following analysis, the smeared position spectra are used. The effect of smearing is taken into account in the estimation of spectral energy resolution discussed in Sect. 3.7.

---

[5] The value of 0.5 is chosen to make the position distribution statistically reasonable, keeping the effect on experimental resolution acceptable. The 0.5 mm smearing corresponds to the missing mass resolution of 130 keV (FWHM). This value is sufficiently small compared with other contribution, i.e., that of beam momentum spread, 220 keV.

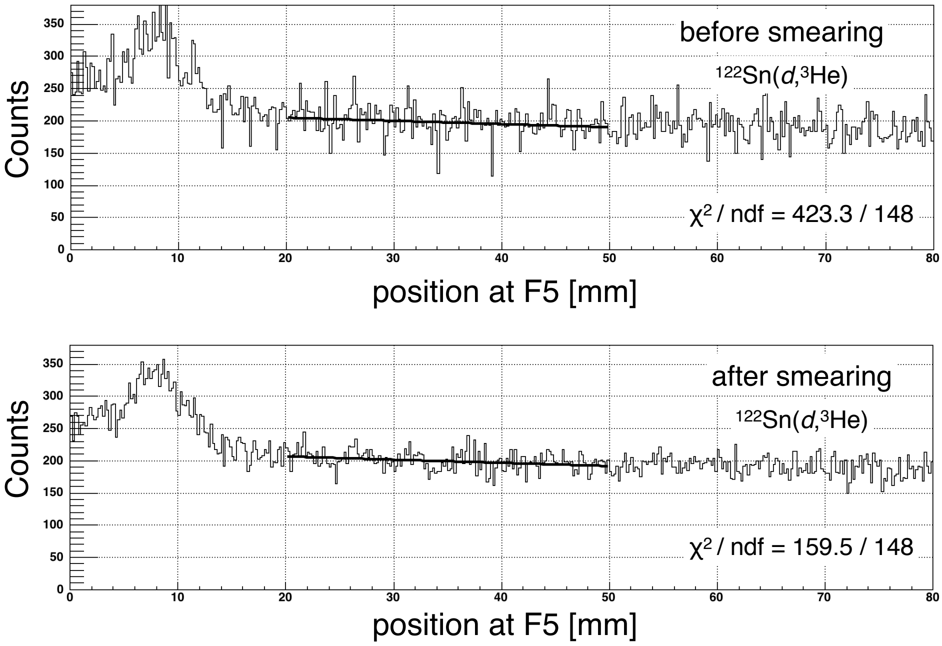

FIGURE 3.20: The position histogram on the X1 plane in the downstream MWDC in a production run with the ^{122}Sn target. (Top) The spectrum before the smearing is introduced. "Combs" are seen in every 5 mm, which is interpreted to be caused by the wire structures. (Bottom) The spectrum after the smearing is introduced, in which "Combs" disappear.

3.2.7 Focal plane position and angle spectra

The obtained position and angle spectra in the ^{122}Sn $(d, {}^{3}\mathrm{He})$ reaction are shown in Fig. 3.21. The peak structures in the horizontal position spectrum correspond to the pionic states in ^{121}Sn.

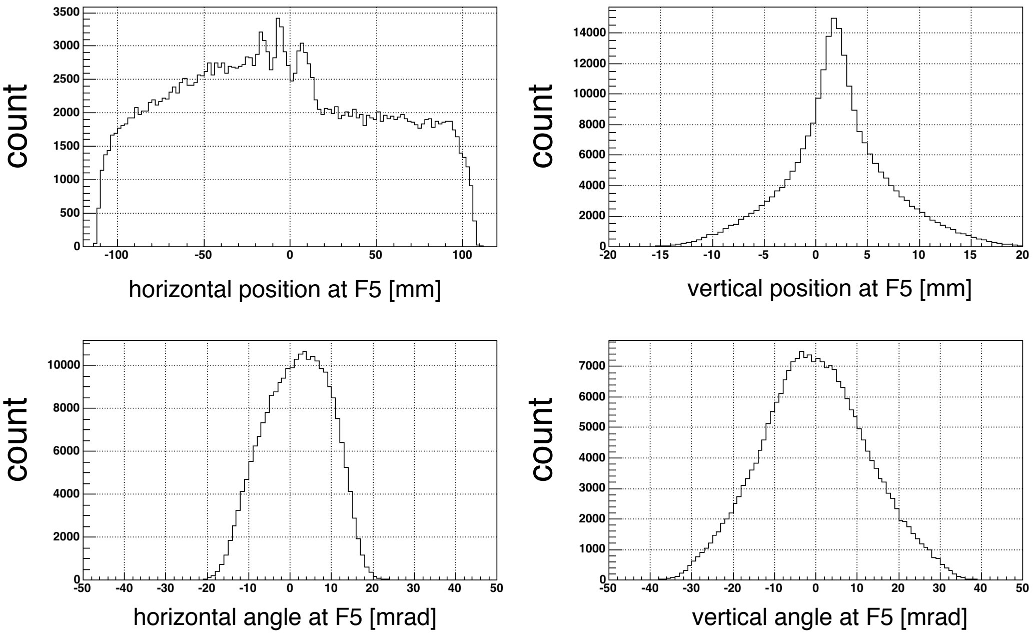

Figure 3.21: The obtained position and angle spectra in a production run with the ^{122}Sn target.

3.3 Deduction of ^{3}He momenta from trajectories at F5 using transfer matrix

^{3}He momenta are deduced based on transformation of the measured trajectories of ^{3}He at F5 focal plane (x_{F5}, a_{F5}, and b_{F5}) to (δ, a_{F0}, and b_{F0}) using ion-optical transfer matrix. The dominant elements of transfer matrix are evaluated from experimental data, while some higher order elements are estimated from the calculated transfer matrix by standard ion optical simulation codes.

The optical parameters at F5 and F0 are related using the transfer matrix elements by the following relations:

$$\begin{aligned}
x_{\mathrm{F5}} = &\ \textstyle\sum_{n=1}^{3}(x_{\mathrm{F5}}|a_{\mathrm{F0}}^n)a_{\mathrm{F0}}^n + \sum_{n=1}^{2}(x_{\mathrm{F5}}|b_{\mathrm{F0}}^n)b_{\mathrm{F0}}^n + (x_{\mathrm{F5}}|a_{\mathrm{F0}}b_{\mathrm{F0}}^2)a_{\mathrm{F0}}b_{\mathrm{F0}}^2 && (3.2)\\
+ &\ (x_{\mathrm{F5}}|a_{\mathrm{F0}}\delta)a_{\mathrm{F0}}\delta + (x_{\mathrm{F5}}|a_{\mathrm{F0}}^2\delta)a_{\mathrm{F0}}^2\delta, && (3.3)\\
+ &\ (x_{\mathrm{F5}}|\delta)\delta + (x_{\mathrm{F5}}|\delta^2)\delta^2 && (3.4)\\
a_{\mathrm{F5}} = &\ (a_{\mathrm{F5}}|a_{\mathrm{F0}})a_{\mathrm{F0}} + (a_{\mathrm{F5}}|a_{\mathrm{F0}}\delta)a_{\mathrm{F0}}\delta, && (3.5)\\
b_{\mathrm{F5}} = &\ (b_{\mathrm{F5}}|b_{\mathrm{F0}})b_{\mathrm{F0}} + (b_{\mathrm{F5}}|b_{\mathrm{F0}}\delta)b_{\mathrm{F0}}\delta + (b_{\mathrm{F5}}|b_{\mathrm{F0}}\delta^2)b_{\mathrm{F0}}\delta^2. && (3.6)
\end{aligned}$$

We solve these equations to obtain the values of δ, a_{F0}, and b_{F0} from F5 parameters: x_{F5}, a_{F5}, and b_{F5}. Each equation consists of the elements in the transfer matrix up to third order, and determined to reproduce experimental dependence of F5 parameters on δ, a_{F0}, and b_{F0} with minimum number of terms.

The parameters in Eq. (3.2)–(3.4) and $(a_{\mathrm{F5}}|a_{\mathrm{F0}})$, $(b_{\mathrm{F5}}|b_{\mathrm{F0}})$ are evaluated from the experimental data. The ^{3}He momenta and solid angle are determined primarily by these 12 elements. The additional higher order elements, $(a_{\mathrm{F5}}|a_{\mathrm{F0}}\delta)$, $(b_{\mathrm{F5}}|b_{\mathrm{F0}}\delta)$ and $(b_{\mathrm{F5}}|b_{\mathrm{F0}}\delta^2)$ are estimated by simulation codes while other matrix elements are safely ignored since the effects are limited in the forward and central region in the spectrometer. The systematic errors of binding energies, widths and formation cross sections from these matrix elements are discussed in Sect. 4.2.

In this section, the details of the analysis to evaluate the transfer matrix elements are explained. Note that these analyses are repeated iteratively until the all analysis become consistent. At the starting point, δ, a_{F0}, and b_{F0} are deduced from the calculated transfer matrix elements.

3.3.1 $(x_{\mathrm{F5}}|a^n_{\mathrm{F0}})$, $(x_{\mathrm{F5}}|b^n_{\mathrm{F0}})$ and $(x_{\mathrm{F5}}|a_{\mathrm{F0}}b^2_{\mathrm{F0}})$

The 8 matrix elements $(x_{\mathrm{F5}}|a_{\mathrm{F0}})$, $(x_{\mathrm{F5}}|a^2_{\mathrm{F0}})$, $(x_{\mathrm{F5}}|a^3_{\mathrm{F0}})$, $(x_{\mathrm{F5}}|b_{\mathrm{F0}})$, $(x_{\mathrm{F5}}|b^2_{\mathrm{F0}})$ and $(x_{\mathrm{F5}}|a_{\mathrm{F0}}b^2_{\mathrm{F0}})$ are determined in a measurement of the a_{F0}, b_{F0} dependence of the largest peak structure associated with pionic 1s state ($(1s)_{\pi^-} \otimes (3s_{1/2})^{-1}_n$ in Fig. 1.4) in the ^{122}Sn $(d, {}^3\mathrm{He})$ reactions. The peak structure is well separated from other configurations, and it is known that kinematical effects of reactions with finite angles are negligible. Therefore, we can safely assume that the angular dependence of the peak position is entirely due to the optical aberration effects. For the transfer matrix measurement, we took the data of the ^{122}Sn$(d, {}^3\mathrm{He})$ reaction separately from the production runs.

Top panel of Fig. 3.22 shows the two dimensional plot of the x_{F5} and a_{F0}. The locus around $x_{\mathrm{F5}} = 5 - 10$ mm corresponds to the peak structure of $(1s)_{\pi^-} \otimes (3s_{1/2})^{-1}_n$. The locus shows the third-order dependence on a_{F0}, which is understood as a effect of $(x_{\mathrm{F5}}|a_{\mathrm{F0}})$, $(x_{\mathrm{F5}}|a^2_{\mathrm{F0}})$ and $(x_{\mathrm{F5}}|a^3_{\mathrm{F0}})$. These values are evaluated from the fitting result of the peak positions with third-order polynomial function as shown by the blue line in the top panel. The peak positions in each angle represented by the asterisks are deduced by the fitting of sliced histogram along Y direction. The bottom panel of Fig. 3.22 shows an example of the fitting of a sliced histogram.

The middle panel of Fig 3.22 shows a two dimensional plot of the $\tilde{x}_{\mathrm{F5}}$ and a_{F0}, where $\tilde{x}_{\mathrm{F5}}$ denotes corrected x_{F5} defined as $\tilde{x}_{\mathrm{F5}} \equiv x_{\mathrm{F5}} - \{a_{\mathrm{F0}}\text{-dependent terms}\}$. The peak positions in the panel become independent of the horizontal angles. With the same manner, b_{F0} dependence of x_{F5} is also corrected with the matrix elements of $(x_{\mathrm{F5}}|b_{\mathrm{F0}})$ and $(x_{\mathrm{F5}}|b^2_{\mathrm{F0}})$.

We also evaluate the cross term of matrix elements $(x_{\mathrm{F5}}|a_{\mathrm{F0}}b^2_{\mathrm{F0}})$ by the fitting of a_{F0} dependence of x_{F5} in each b_{F0}.

3.3.2 $(x_{\mathrm{F5}}|a_{\mathrm{F0}}\delta)$ and $(x_{\mathrm{F5}}|a^2_{\mathrm{F0}}\delta)$

The δ dependence of $(x_{\mathrm{F5}}|a_{\mathrm{F0}})$ and $(x_{\mathrm{F5}}|a^2_{\mathrm{F0}})$ are evaluated based on the same types of data as in the previous section with different BigRIPS scale. These dependence are represented by the matrix elements $(x_{\mathrm{F5}}|a_{\mathrm{F0}}\delta)$ and $(x_{\mathrm{F5}}|a_{\mathrm{F0}}\delta^2)$. The scaled data were taken for different central momenta of the BigRIPS by scaling the magnetic fields of the whole system by three different factors, 1.00 (nominal setting), +1.004884, and +1.009790. We again make use of $(1s)_{\pi^-} \otimes (3s_{1/2})^{-1}_n$ peak structures measured in these runs. Within these small changes, the linearity of the magnetic field is safely assumed. The magnetic fields were monitored precisely by the NMR in dipoles and are stable within 0.001 % level during each measurement. In each condition, we deduce a_{F0} dependence of x_{F5} as in the previous section, and the δ dependence of $(x_{\mathrm{F5}}|a_{\mathrm{F0}})$ and $(x_{\mathrm{F5}}|a^2_{\mathrm{F0}})$ are evaluated. The δ dependence of $(x_{\mathrm{F5}}|a^3_{\mathrm{F0}})$, $(x_{\mathrm{F5}}|b_{\mathrm{F0}})$ and $(x_{\mathrm{F5}}|b^2_{\mathrm{F0}})$ are found to be negligibly small.

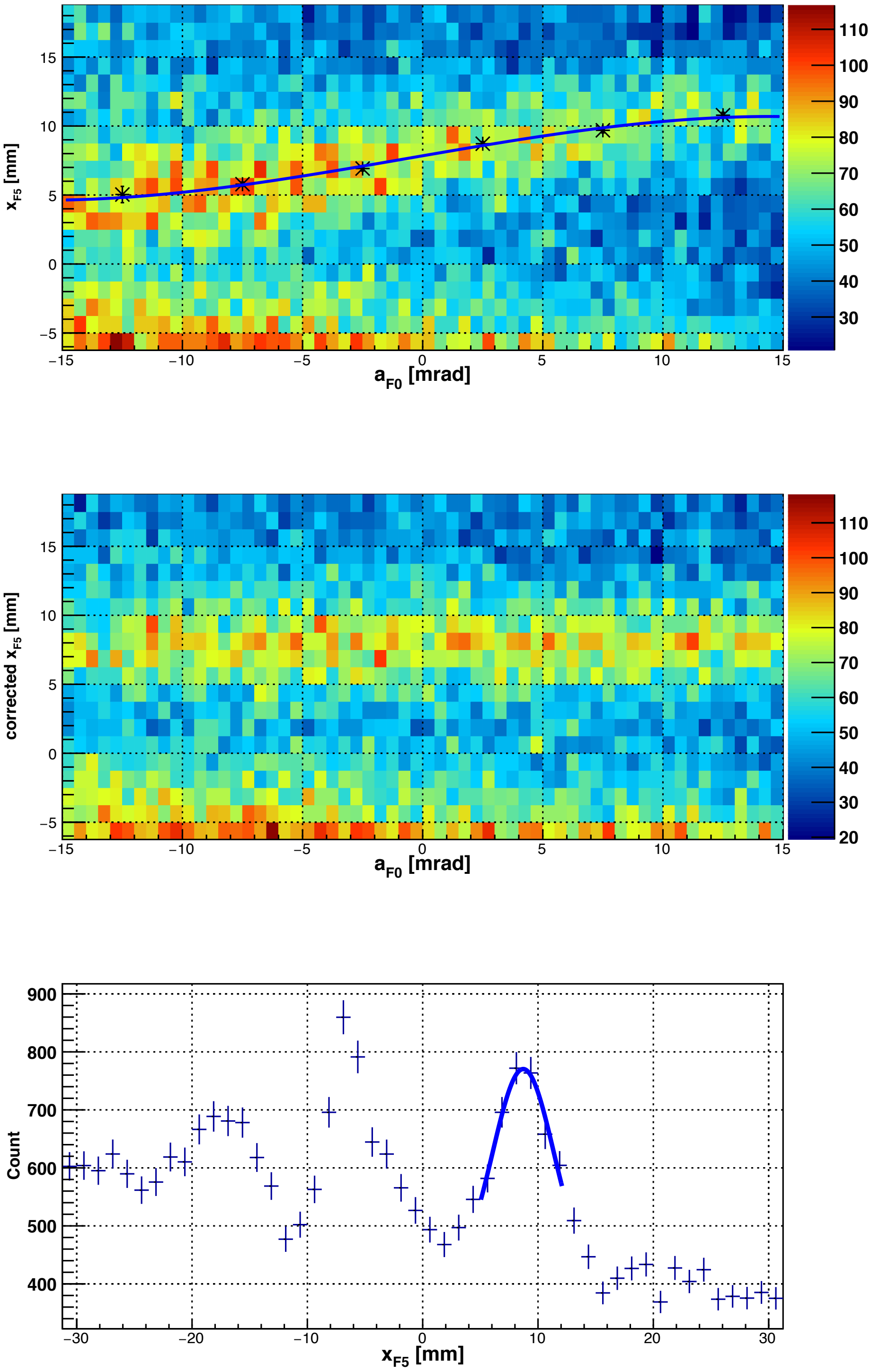

FIGURE 3.22: (Top)Two dimensional plots of x_{F5} and a_{F0} in the transfer matrix measurement run using with the $^{122}(d, {}^{3}\mathrm{He})$ reaction. The locus around $x_{\mathrm{F5}} = 5 - 10$ mm corresponds to the pionic states with the configuration of $(1s)_{\pi^-} \otimes (3s_{1/2})_n^{-1}$. The asterisks represent the peak position of the sliced histogram in each reaction angles as shown in the bottom panel. (Middle) Two dimensional plots of the corrected x_{F5} and a_{F0}. (Bottom) A slice of the two dimensional plot in the top panel along Y direction. The peak positions in each angle are deduced by the fitting as shown in the figure.

3.3.3 $(x_{\mathrm{F5}}|\delta)$ and $(x_{\mathrm{F5}}|\delta^2)$

The values of $(x_{\mathrm{F5}}|\delta)$ and $(x_{\mathrm{F5}}|\delta^2)$ are determined in the same measurement as in Sect. 3.3.2. These values are most dominant terms in the determination of the ^{3}He momenta. The shift of the peak positions in the scaled settings directly represent these values. Figure 3.23 shows $\tilde{x}_{\mathrm{F5}}$ spectrum of ^{3}He with the ^{122}Sn$(d, {}^3\mathrm{He})$ reaction in each scale. The reaction angle $\theta_{\mathrm{reaction}} \equiv \sqrt{a_{\mathrm{F0}}^2 + b_{\mathrm{F0}}^2}$ is limited under 1.5°, which is equivalent to the region used in the subsequent analysis procedures. The peak width of each scale is different because of the position dependence of the experimental resolution (See Sect. 3.7). Fitting functions is a sum of Voigtian and a constant background. The value of δ at a center of the peak with a scaling factor f, denoted as $\delta(f)$, is calculated as

$$\delta(f) = \frac{(1 - f + \delta(1))}{f}. \tag{3.7}$$

The value of $\delta(1)$ is calculated by the corrected x_{F5} of the peak at $f = 1$ and calculated $(x_{\mathrm{F5}}|\delta)$[6]. We measure the peak position in each scaling factor f. Figure 3.24 shows the relation between the $\delta(f)$ (abscissa) and the measured peak positions in the corrected x_{F5} spectra (ordinate). We fit these data by second-order polynomial, which is represented as the black line, and determine the value of $(x_{\mathrm{F5}}|\delta)$ and $(x_{\mathrm{F5}}|\delta^2)$. The correlation coefficient of these value is 0.85, which is used to estimate the systematic errors from these elements.

---

[6] After determination of the $(x_{\mathrm{F5}}|\delta)$, the calculated value is confirmed to be accurate enough for this purpose. The difference between the estimated value by experimental data and the calculated value does not affect the determination of $(x_{\mathrm{F5}}|\delta)$ and $(x_{\mathrm{F5}}|\delta^2)$.

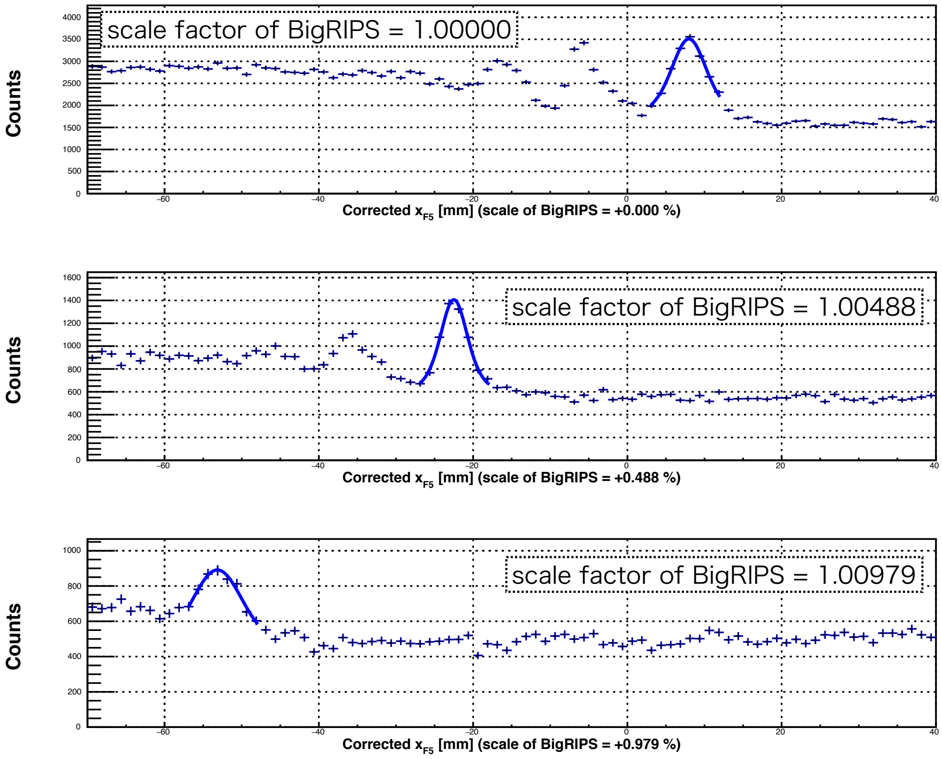

FIGURE 3.23: Spectra of the corrected x_{F5} with ^{122}Sn target in different scale of BigRIPS. The magnetic field of BigRIPS are scaled by +1.00000 (top), +1.00488 (middle) and +1.00979 (bottom), respectively.

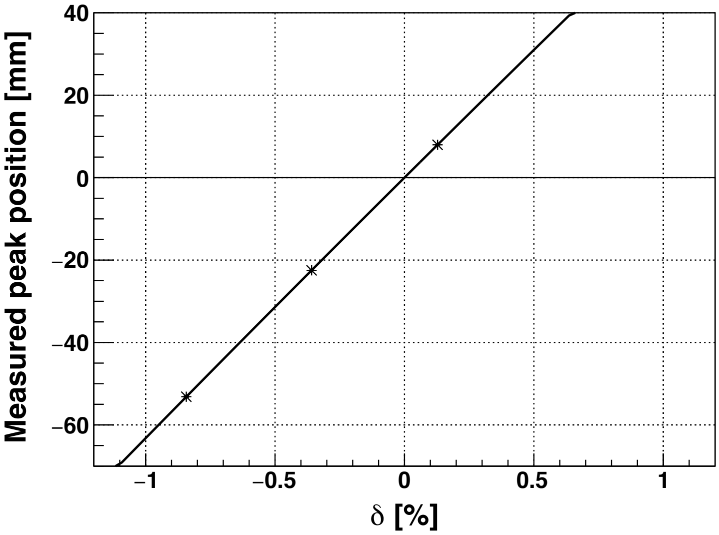

FIGURE 3.24: The relation between the δ associated with the pionic states with the configuration of $(1s)_{\pi^-} \otimes (3s_{1/2})_n^{-1}$ in each scale of BigRIPS (abscissa) and the measured peak positions in the corrected x_{F5} spectra (ordinate). The black line represents the result of the fitting by second-order polynomial.

3.3.4 $(a_{\mathrm{F5}}|a_{\mathrm{F0}})$, $(b_{\mathrm{F5}}|b_{\mathrm{F0}})$ and an incident beam direction

Angular magnifications, $(a_{\mathrm{F5}}|a_{\mathrm{F0}})$ and $(b_{\mathrm{F5}}|b_{\mathrm{F0}})$, are estimated by using two-body reactions of the $p(d, {}^3\mathrm{He})\pi^0$ on the polyethylene target. The momentum of ^{3}He produced in the reaction depends on the reaction angles. We make use of this known relation between the momenta and angles for the deduction of the angular magnifications. In order to make a detailed comparison with the experimental data, we performed a Monte-Carlo simulation[7]. The δ, a_{F0} and b_{F0} distributions of ^{3}He at the target from the $p(d, {}^3\mathrm{He})\pi^0$ reaction are simulated as in the following steps. Optimized parameters through the simulation are the matrix elements of $(a_{\mathrm{F5}}|a_{\mathrm{F0}})$ and $(b_{\mathrm{F5}}|b_{\mathrm{F0}})$, and the incident beam direction with respect to the optical axis of the spectrometer at F0. The analysis is performed in the condition of $|a_{\mathrm{F0}}|$, $|b_{\mathrm{F0}}| < 15$ mrad to suppress the effect of other higher order matrix elements[8].

(a) Simulation of the $p(d, {}^3\mathrm{He})\pi^0$ reaction at F0.
To simulate the emitted ^{3}He distribution at F0, we take into consideration the measured momentum and angular distribution of the primary deuteron beam as explained in Sect. 2.3, dispersion of the beam transfer line and intrinsic position distribution of the beam. The width of the target of 2 mm is also taken into account.

Then, the ^{3}He distribution after the reaction is simulated. ^{3}He momenta are calculated according to the relation between the momenta and reaction angles. The energy loss and multiple scattering in the target are also taken into account. From the obtained angle and momentum of the ^{3}He, the optical parameters at the F0 focal plane (δ, a_{F0} and b_{F0}) are simulated.

(b) Simulation from F0 to F5.
The parameters of ^{3}He at F0 (δ, a_{F0} and b_{F0}) is transferred to the parameters at F5 (x_{F5}, a_{F5} and b_{F5}) based on the deduced transfer matrix elements. In the transformation, we consider the transmission probability as explained in Sect. 3.5.2. We also consider the multiple scattering effect caused by the F5 materials (stainless steel window, air, and MWDCs). The tracker resolutions, including the effect of the smearing on x_{F5} are also taken into account.

(c) Analysis of simulated data and comparison with experiment.
We analyze the simulated data of (x_{F5}, a_{F5} and b_{F5}) produced in (b) and obtain (δ, a_{F0} and b_{F0}) by solving the Eq. (3.2)–(3.6), as for the experimental data.

---

[7] The simulation is different from the simulation performed by MOCADI. In the simulation, the parameters of the particles at the focal plane are calculated based on the transfer matrix obtained from the analysis in this section, as described in the text.

[8] δ dependence of the matrix elements are suppressed as well as the angular dependence with small reaction angle, because the momentum and the reaction angle are strongly correlated in the reaction.

Top and bottom figures in Fig. 3.25 compare two dimensional δ and a_{F0} plots in the experimental data and the simulation. For the analysis, $|b_{\mathrm{F0}}|$ is limited to < 10 mrad. The asymmetric structure of a_{F0} comes from the multiple scattering at the vacuum window at F5 and the subsequent correction of the higher order aberration, such as $(x_{\mathrm{F5}}|a_{\mathrm{F0}}\delta)$.

Parameters (the incident beam direction, angular magnifications) are optimized to minimize a χ^2 of these histograms. A χ^2 between two histograms ($l \times r$ bins) is defines as

$$\begin{aligned} \chi^2 \equiv & \sum_{i=1}^{l}\sum_{j=1}^{r}\frac{(n_{ij}-N\hat{p}_{ij})^2}{N\hat{p}_{ij}} + \sum_{i=1}^{l}\sum_{j=1}^{r}\frac{(m_{ij}-M\hat{p}_{ij})^2}{M\hat{p}_{ij}}, \\ \hat{p}_{ij} \equiv & \frac{n_{ij}+m_{ij}}{N+M}, \end{aligned} \tag{3.8}$$

where n_{ij}, m_{ij} represent the $i \times j$th bin content of each histogram. N, M are total number of contents in each histogram. The χ^2 represents how similar the probability distributions of each histogram are.

We scan the parameters, horizontal incident beam direction and $(a_{\mathrm{F5}}|a_{\mathrm{F0}})$ and evaluate the value of χ^2. Fig. 3.26 shows the χ^2 as a function of each parameter. In the calculation, the another parameter is optimized for each point in the graph. By minimizing the χ^2, the primary beam direction and the $(a_{\mathrm{F5}}|a_{\mathrm{F0}})$ are determined. The same analysis is performed for vertical direction as shown in Fig. 3.27, 3.28. These analyses are performed iteratively until the results of both direction become consistent.

As a result, the incident beam directions are estimated to be $+0.9 \pm 1$ mrad for the horizontal direction and $+0.3 \pm 1$ mrad for the vertical direction. The values of the $(a_{\mathrm{F5}}|a_{\mathrm{F0}})$ and the $(b_{\mathrm{F5}}|b_{\mathrm{F0}})$ are estimated to be -0.519 ± 0.05 and -0.540 ± 0.05, respectively. The errors of the $(a_{\mathrm{F5}}|a_{\mathrm{F0}})$ and the $(b_{\mathrm{F5}}|b_{\mathrm{F0}})$ are deduced by changing the fit ranges of a_{F0} and b_{F0}.

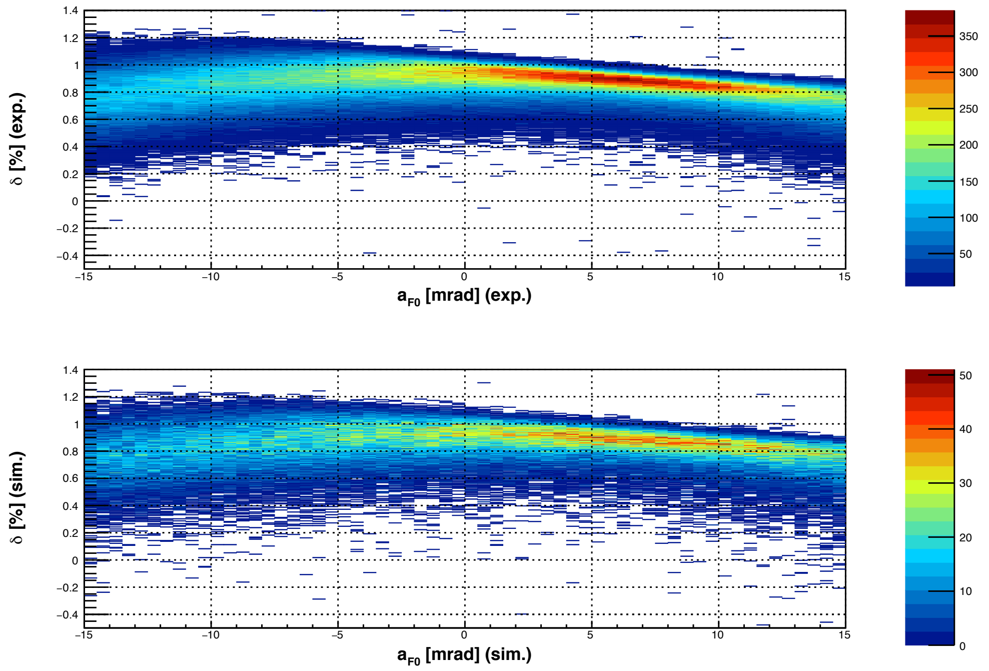

FIGURE 3.25: Two dimensional δ and a_{F0} plots in the experimental data (Top) and simulation (Bottom) with polyethylene target.

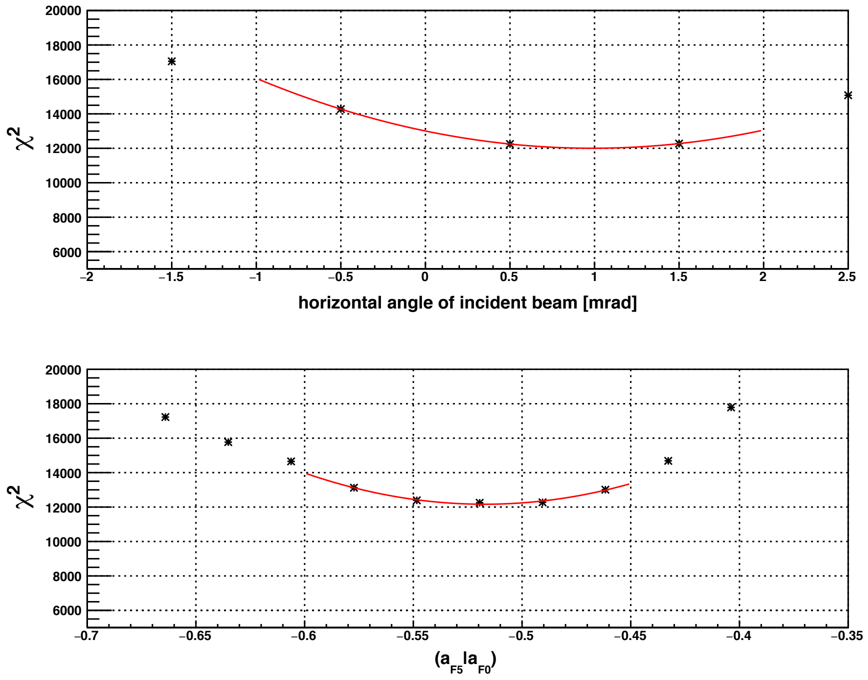

FIGURE 3.26: The χ^2 (ndf = 16631) as a function of the horizontal primary beam direction (Top) and $(a_{\mathrm{F5}}|a_{\mathrm{F0}})$ (Bottom) in the simulation.

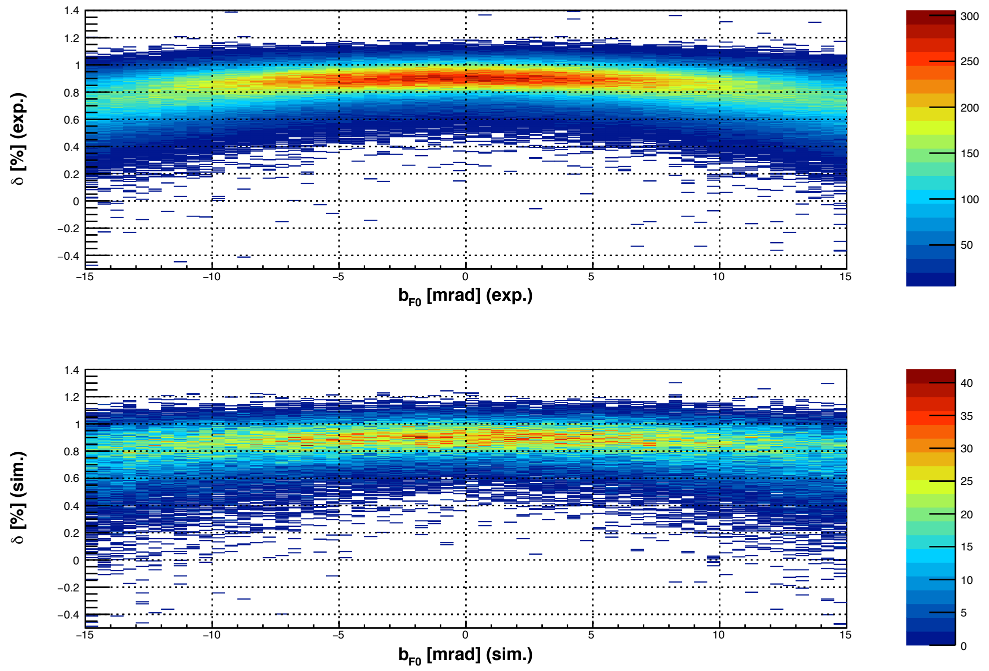

FIGURE 3.27: Two dimensional δ and b_{F0} plots in the experimental data (Top) and simulation (Bottom) with polyethylene target.

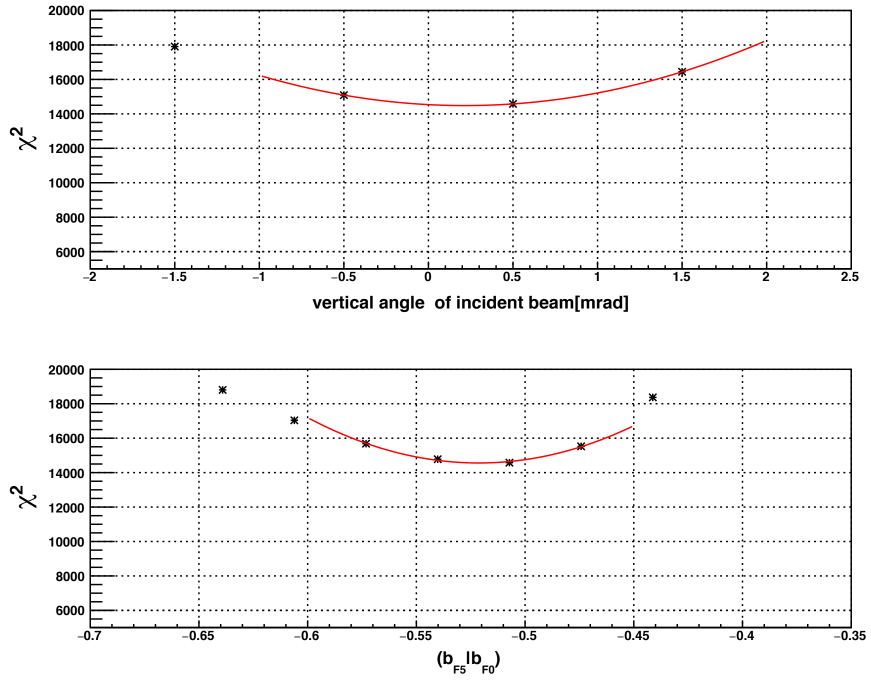

FIGURE 3.28: The χ^2 (ndf = 16631) as a function of the vertical primary beam direction (Top) and $(b_{\mathrm{F5}}|b_{\mathrm{F0}})$ (Bottom) in the simulation.

3.3.5 $(a_{\mathrm{F5}}|a_{\mathrm{F0}}\delta)$, $(b_{\mathrm{F5}}|b_{\mathrm{F0}}\delta)$ and $(b_{\mathrm{F5}}|b_{\mathrm{F0}}\delta^2)$

The higher order aberrations, $(a_{\mathrm{F5}}|a_{\mathrm{F0}}\delta)$, $(b_{\mathrm{F5}}|b_{\mathrm{F0}}\delta)$ and $(b_{\mathrm{F5}}|b_{\mathrm{F0}}\delta^2)$ are estimated by standard ion optical codes. The aberrations are small, and the effects on the F5 optical parameters are as small as those of the errors associated to the first order matrix elements, $(a_{\mathrm{F5}}|a_{\mathrm{F0}})$ and $(b_{\mathrm{F5}}|b_{\mathrm{F0}})$ in the forward region. As standard ion optical simulation codes, we used GICOSY[9] and MOCADI[10], which are known to reproduce the experimental conditions fairly well. By these simulation codes, we produce Monte Carlo data which can be directly compared with the experimental data. These Monte Carlo data are analyzed with the same manner with that for experimental data to obtain the effective transfer matrix elements, reflecting the effect of multiple scattering and energy straggling, to convert the measured trajectories to momenta of ^{3}He at F0. An additional analysis of a same simulation in Sect 3.3.4 with wider angular range $\theta < 1.5^\circ$ including $(a_{\mathrm{F5}}|a_{\mathrm{F0}}\delta)$, $(b_{\mathrm{F5}}|b_{\mathrm{F0}}\delta)$ and $(b_{\mathrm{F5}}|b_{\mathrm{F0}}\delta^2)$ as free parameters shows limited differences in the results. The differences are considered in the evaluation of overall systematic errors in binding energies, widths and cross sections arising from the uncertainties of these higher order aberrations.

3.3.6 Summary of deduced transfer matrix

The analysis of matrix elements explained above are repeated iteratively until all analysis become consistent. The deduced matrix elements are summarized in Table 3.1. The values written in bold font are used in the following analysis. In the analysis, the a_{F0} is limited within ± 15 mrad to suppress the optical effect on the x_{F5}. The errors on the excitation energies caused by $(x_{\mathrm{F5}}|a^2_{\mathrm{F0}})$ and $(x_{\mathrm{F5}}|a^2_{\mathrm{F0}}\delta)$ reach to 30 keV and 25 keV, respectively at the outside of the limitation[11]. These values are more than twice as large as the total error inside the limitation.

---

[9] The code GICOSY [37] calculates transfer matrices up to fifth order based on the optical systems such as dipoles and quadrupoles. In the calculation, the fringing fields are also taken into account. We use GICOSY instead of COSY, because GICOSY creates matrix files that can be used in MOCADI. We confirm the calculated results of COSY and GICOSY are consistent with sufficient accuracy.

[10] The MOCADI [38] is a Monte-Carlo code for transport of ions through matter within ion-optical system. The code simulate particles position and angles in ion systems based on the ion transfer matrices, geometrical aperture of magnets and beam pipes, and interaction with materials such as detectors, vacuum windows and so on.

[11] These values are obtained at a point with $\delta = 0.3\%$, $a_{\mathrm{F0}} = 20$ mrad and $b_{\mathrm{F0}} = 20$ mrad. 0.3% corresponds to the difference between pionic states in $1s$ orbit and $2p$ orbit.

matrix element	deduced values from exp. data	calculated values
$(x_{\mathrm{F5}}\|a_{\mathrm{F0}})$ [mm/mrad]	**$(+2.75 \pm 0.2) \times 10^{-1}$**	$+1.93 \times 10^{-1}$
$(x_{\mathrm{F5}}\|a^2_{\mathrm{F0}})$ [mm/mrad^2]	**$(-9.44 \pm 8.0) \times 10^{-4}$**	-1.37×10^{-3}
$(x_{\mathrm{F5}}\|a^3_{\mathrm{F0}})$ [mm/mrad^3]	**$(-4.41 \pm 0.9) \times 10^{-4}$**	-7.10×10^{-4}
$(x_{\mathrm{F5}}\|b_{\mathrm{F0}})$ [mm/mrad]	**$(+4.87 \pm 6.1) \times 10^{-3}$**	0.00
$(x_{\mathrm{F5}}\|b^2_{\mathrm{F0}})$ [mm/mrad^2]	**$(-8.45 \pm 4.0) \times 10^{-4}$**	-2.15×10^{-4}
$(x_{\mathrm{F5}}\|a_{\mathrm{F0}}b^2_{\mathrm{F0}})$ [mm/mrad^3]	**$(-2.53 \pm 0.5) \times 10^{-4}$**	-3.01×10^{-4}
$(x_{\mathrm{F5}}\|a_{\mathrm{F0}}\delta)$ [mm/mrad/%]	**$(+7.83 \pm 0.2) \times 10^{-1}$**	8.27×10^{-1}
$(x_{\mathrm{F5}}\|a^2_{\mathrm{F0}}\delta)$ [mm/mrad^2/%]	**$(+6.74 \pm 1.9) \times 10^{-3}$**	$+1.28 \times 10^{-3}$
$(x_{\mathrm{F5}}\|\delta)$ [mm/%]	**$+62.42 \pm 0.27$**	$+61.20$
$(x_{\mathrm{F5}}\|\delta^2)$ [mm/%^{2}]	**$(-7.84 \pm 4.7) \times 10^{-1}$**	-8.34×10^{-1}
$(a_{\mathrm{F5}}\|a_{\mathrm{F0}})$[mrad/mrad]	**$(-5.19 \pm 0.5) \times 10^{-1}$**	-5.48×10^{-1}
$(b_{\mathrm{F5}}\|b_{\mathrm{F0}})$[mrad/mrad]	**$(-5.40 \pm 0.5) \times 10^{-1}$**	-6.39×10^{-1}
$(a_{\mathrm{F5}}\|a_{\mathrm{F0}}\delta)$[mrad/mrad/%]	–	**-3.72×10^{-2}**
$(b_{\mathrm{F5}}\|b_{\mathrm{F0}}\delta)$[mrad/mrad/%]	–	**-6.79×10^{-2}**
$(b_{\mathrm{F5}}\|b_{\mathrm{F0}}\delta^2)$[mrad/mrad/%^{2}]	–	**$+5.29 \times 10^{-2}$**

TABLE 3.1: Optical transfer matrix elements used in the transformation of the measured trajectories of ^{3}He at F5 focal plane (x_{F5}, a_{F5}, and b_{F5}) to (δ, a_{F0} in Eq. (3.2)–(3.6). The values written in bold font are used in the following analysis.

3.4 Deduction of excitation energies

So far we have deduced δ, the relative momenta of ^{3}He to the central momenta of the spectrometer from the experimental data. Here, we calibrate the central momenta by energy calibration described in Sect. 3.4.1, and deduce the excitation energy in Sect. 3.4.2.

3.4.1 Energy calibration by $p(d, {}^3\mathrm{He})\pi^0$ reaction

The ^{3}He energy of the central trajectory $E^0_{^3\mathrm{He}}$ is calibrated by using again the $p(d, {}^3\mathrm{He})\pi^0$ reaction on the polyethylene target. The detailed comparison, which is described in the previous section 3.3.4 between the experimental data and the data of Monte-Carlo simulation, also serves as a calibration of the system. Right panels in Fig. 3.29 show plots of δ vs reaction angle in the experimental data and in the simulation. We define χ^2 between two 2D histograms as Eq. (3.8).

To determine $E^0_{^3\mathrm{He}}$, χ^2 is calculated by changing $E^0_{^3\mathrm{He}}$. The determined value of $E^0_{^3\mathrm{He}}$ is

$$E^0_{^3\mathrm{He}} = 362.416 \pm 0.003\ (\text{stat.})^{+0.007}_{-0.0003}\ (\text{sys.})\ \text{MeV}. \tag{3.9}$$

To minimize the effect of the higher order aberration and acceptance correction, the reaction angles of the events used in the analysis is limited to be < 5 mrad. The systematic errors of the determination of the calibration point are discussed in Sect. 4.2.1.

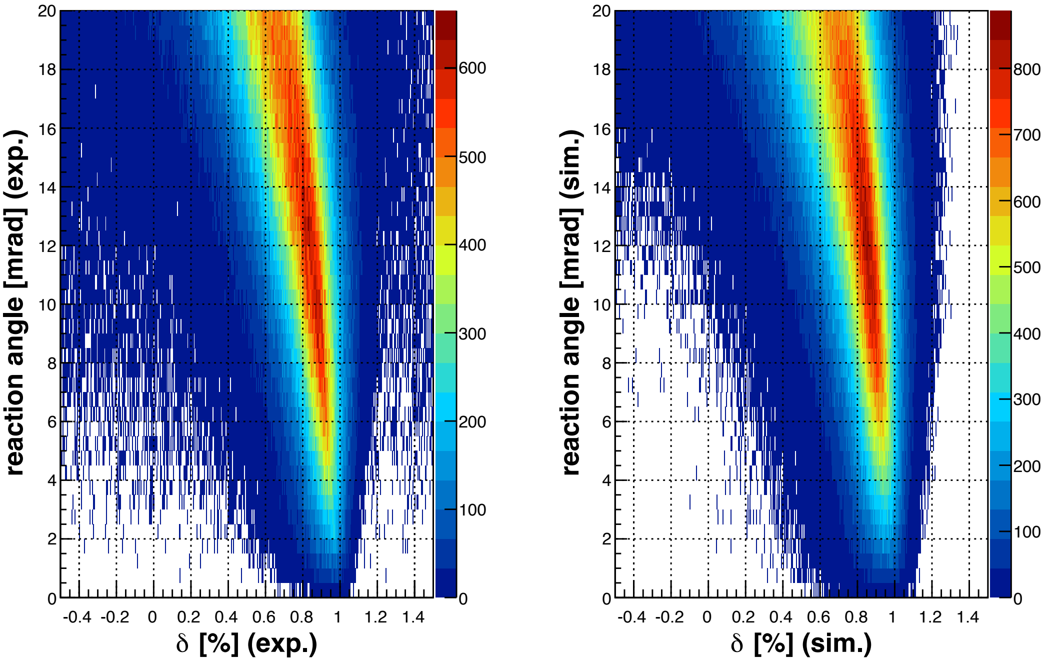

FIGURE 3.29: δ-reaction angle plot from the $p(d,{}^3\text{He})$ reaction. Left figure shows the experimental data and right figure shows the simulation data.

3.4.2 Deduction of excitation energy

To compare the experimental data with the theoretical spectrum, Q value and excitation energy of ^{121,116}Sn are calculated from the kinetic energy of ^{3}He as below.

First, the energy of the ^{3}He in the center-of-mass (CM) frame, $E^{\text{CM}}_{{}^3\text{He}}$, and a Mandelstam variable 's', the square of the total energy in the CM frame of this reaction, are calculated from the momentum, energy of the ^{3}He, and reaction angle in lab. frame: $P^{\text{lab}}_{{}^3\text{He}}$, $E^{\text{lab}}_{{}^3\text{He}}$ and θ^{lab}, as

$$E^{\text{CM}}_{{}^3\text{He}} = \beta E^{\text{lab}}_{{}^3\text{He}} - \beta\gamma P^{\text{lab}}_{{}^3\text{He}} \cos\theta^{\text{lab}}, \tag{3.10}$$

$$s = (M_d + M_{{}^{122,117}\text{Sn}})^2 + 2M_{{}^{122,117}\text{Sn}} T^{\text{lab}}_d. \tag{3.11}$$

Here, M_d, $M_{{}^{122,117}\text{Sn}}$ and T^{lab}_d are mass of deuteron, mass of target ^{122,117}Sn, and the kinetic energy of the primary deuteron beam in lab. frame, respectively. β is the velocity of the CM frame and γ is $1/\sqrt{1-\beta^2}$. From these values, the missing mass M_{X}, Q value,

Q, and excitation energy, $E_{\rm ex}$, are calculated as the followings,

$$\begin{aligned} M_{\rm X} = & \sqrt{s + M_{^3{\rm He}}^2 - 2\sqrt{s}E_{^3{\rm He}}^{\rm CM}}. & (3.12) \\ Q = & (M_{\rm X} + M_{^3{\rm He}}) - (M_d + M_{\rm target}) & (3.13) \\ E_{\rm ex} = & M_{\rm X} - M_{^{121,116}{\rm Sn}}. & (3.14) \end{aligned}$$

$M_{^3{\rm He}}$ and $M_{^{121,116}{\rm Sn}}$ are mass of ^{3}He and mass of ^{121,116}Sn. Here, the mass of ^{121}Sn is calculated as mass of ^{122}Sn − (mass of neutron − minimum neutron separation energy). In the description above the energy loss in the target is omitted. In the analysis, the energy loss are taken account for the particle reacting at the middle of the target.

3.5 Deduction of reaction cross section

The double-differential cross section $d^2\sigma/d\Omega dE_{\rm ex}$ is calculated from the following equation,

$$N_{^3{\rm He}} = \frac{d^2\sigma}{d\Omega dE_{\rm ex}} \times N_d \times \rho_{N_{\rm target}} \times \Delta\Omega \times \Delta E_{\rm ex} \times Acc \times \alpha, \tag{3.15}$$

where $N_{^3{\rm He}}$, N_d and $\rho_{N_{\rm target}}$ are the number of measured ^{3}He particle, the number of primary deuteron beam hitting the target, and the number of target nuclei (^{122,117}Sn) per unit area. $\Delta\Omega$ and $\Delta E_{\rm ex}$ are the solid angle and the range of the excitation energy of the corresponding data. Acc is the effect of the acceptance. α is the analysis efficiency coming from the hardware trigger efficiency, the particle identification, tracking, and DAQ.

3.5.1 Luminosity

As explained in Sect. 2.3, the intensity of the primary deuteron beam is monitored by coincidence signals of three scintillators in upstream of the target. From the comparison with a current of the Faraday cup, 1 count of coincidence signals corresponds to 2.5×10^8 particle when the wide ^{122}Sn target (12.2 mg/cm^2) is used. The numbers of coincidence signals in the production run are 1.35×10^8 count for ^{122}Sn target (12.5 mg/cm^2) and 4.88×10^8 count for ^{117}Sn target (9.9 mg/cm^2), which correspond to 3.4×10^{16} particles and 1.5×10^{16} particles, respectively.

3.5.2 Acceptance

In this section, we evaluate the probability that an incident particle at a specified momentum and angle passes through the spectrometer and reaches the focal plane after interaction with matters in-between. We define the probability as "acceptance". The acceptance is estimated based on MOCADI simulation using the calculated transfer matrix elements[12]. As mentioned above, the simulation code reproduces the experimental conditions fairly well. As shown in the Table 3.1, the influential elements such as angular magnifications or dispersion are well reproduced by the calculation. Furthermore, the effect of the acceptance correction on the binding energies and widths of peak structures are sufficiently small as discussed below. Therefore we can safely rely on the result from MOCADI.

For each a_{F0} and b_{F0}, the ratio between the number of input particles and the number of particles reaching F7 focal plane are compared in a histogram as a function of δ. Figure 3.30 shows the example of the histogram in $|a_{\mathrm{F0}}| < 3$ mrad, $|b_{\mathrm{F0}}| < 3$ mrad and in $-6 < a_{\mathrm{F0}} < -3$ mrad, $3 < b_{\mathrm{F0}} < 6$ mrad. The histograms are fitted by 1st – 5th order polynomial functions. The fitting starts with the 1st order, and if the reduced χ^2 is far from 1, a higher order function is used. The histograms and functions are prepared for every 3 mrad. For the intermediate angles, interpolated values are used as the acceptance. Note that even for the central trajectory of the beam line, the acceptance is about 0.9, because about 10% of the particles are lost between the F5 and F7 focal planes by multiple scattering in the thick scintillators and degraders at the F5 focal plane($\approx$ 16 mm). As shown in the figure, the acceptance distribution are well approximated by the linear function in small region of the relative momentum $\delta = -0.5\%$ to 1.0%, where bound structures of pionic atoms and the calibration peak are included. As a result, the effect of the acceptance correction on the analysis of the binding energies and widths of pionic states are negligibly small. The effect on the analysis of cross section from the acceptance correction is estimated later.

Table 3.2 summarizes factors for calculation of the double-differential cross section. The number density of the target nuclei, hardware trigger efficiency, pID efficiency, tracking efficiency, and DAQ efficiency are also listed.

---

[12] The calculated matrices are used for the simulation, because the simulation of the acceptance requires all matrices between each focal plane (F0 to F1, F1 to F2,$\cdots$, F6 to F7), while the analysis in the previous section deduce only the matrix between F0 to F5.

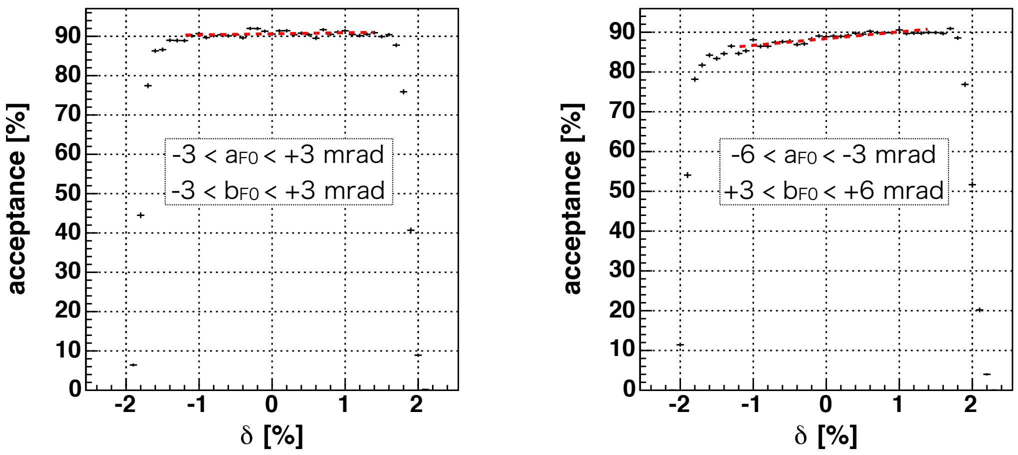

FIGURE 3.30: The acceptance simulated by MOCADI. (left) The acceptance shape in $|a_{\rm F0}| < 3$ mrad / $|b_{\rm F0}| < 3$ mrad. (right) The acceptance shape in $-6 < a_{\rm F0} < -3$ mrad / $3 < b_{\rm F0} < 6$ mrad. The red line represents fitting result by polynomial functions. The fit results are used to correct the acceptance.

Factor	^{122}Sn	^{117}Sn
Number of deuteron ($\times\ 10^{16}$ particle)	3.4 ± 0.7	1.5 ± 0.3
number density of the target nuclei ($\times 10^{19}$) [1/cm^2]	6.05 ± 0.24	5.10 ± 0.26
hardware trigger efficiency%	98.0 ± 0.5	98.0 ± 0.5
pID efficiency%	> 98.5	> 98.5
tracking efficiency%	98.8 ± 0.4	98.8 ± 0.4
DAQ efficiency%	83.7 ± 0.05	87.1 ± 0.1

TABLE 3.2: Summary of the factors for the cross section determination. The pID efficiency is evaluated for each position as shown in Fig. 3.19. The position dependence is also taken into account.

3.6 Excitation spectra of ^{121,116}Sn

The obtained excitation spectra of ^{121,116}Sn are shown in Fig. 3.31. The top and bottom figures show the excitation spectrum of ^{121}Sn and that of ^{116}Sn in $\theta_{\rm reaction} < 2^\circ$, respectively. Here, $\theta_{\rm reaction}$ is defined as $\sqrt{a_{\rm F0}^2 + b_{\rm F0}^2}$. The vertical axes are the double-differential cross section. These excitation spectra are deduced only in the region of $127 < E_{\rm ex} < 145$ MeV for ^{121}Sn and $129 < E_{\rm ex} < 147$ MeV for ^{116}Sn, because the outside of the regions the particle trajectories are too close to edges of the beam line and acceptance estimated by MOCADI simulation are not reliable in the regions. The red dashed vertical lines correspond to the π^- production threshold, which is exactly same as the mass of π^-.

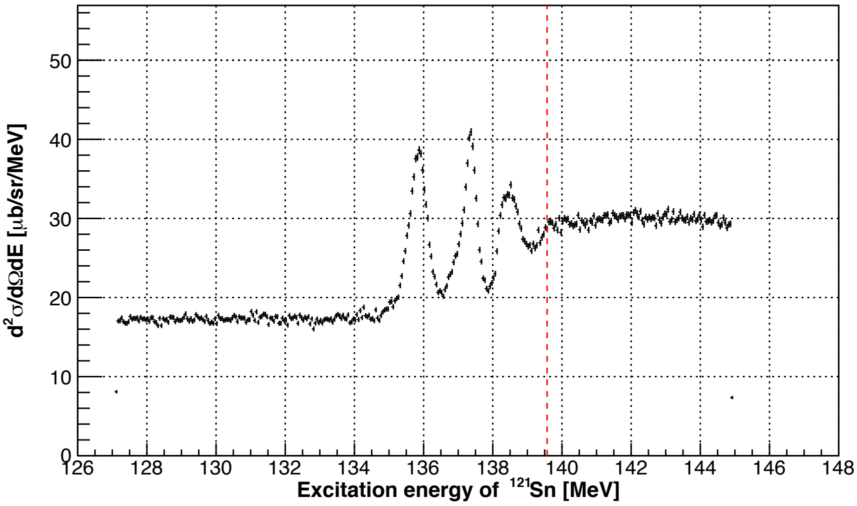

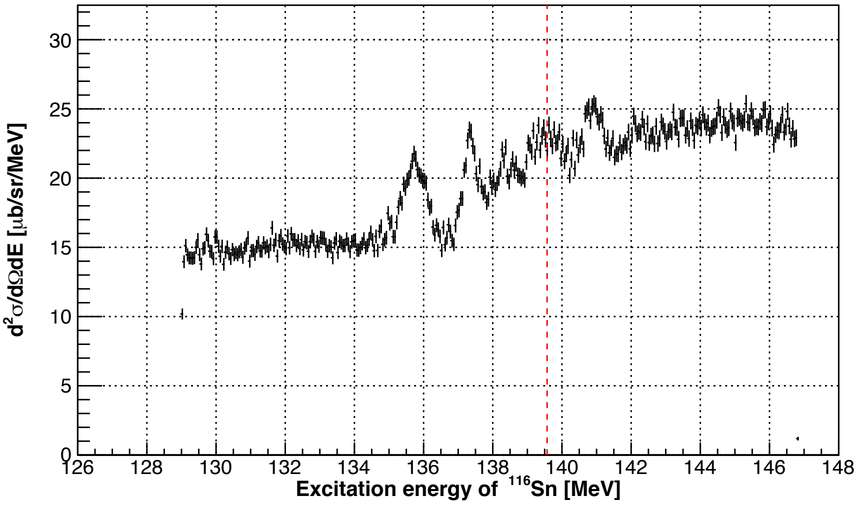

FIGURE 3.31: (Top) E_{ex} spectrum of ^{121}Sn in $0^\circ < \theta < 2^\circ$. (Bottom) E_{ex} spectrum of ^{116}Sn in $0^\circ < \theta < 2^\circ$. The red dashed vertical lines correspond to the quasi-free π^- production threshold energy. These excitation spectra are deduced in the region of $127 < E_{\mathrm{ex}} < 145$ MeV for ^{121}Sn and $129 < E_{\mathrm{ex}} < 147$ MeV for ^{116}Sn.

3.7 Experimental energy resolution

In this section the experimental resolution is described, which is estimated based on a Monte Carlo simulation. The resolution is dominated by three contributions: (i) the momentum spread of the primary beam, (ii) multiple scattering at the stainless steel windows at the ends of vacuum pipes and (iii) uncertainty of the reaction point in the target. In Sect. 3.7.1 to 3.7.3 analysis of the contributions in combination with the ion optical transfer matrices are explained. In Sect. 3.7.4, details of the Monte Carlo simulation, including the multiple scattering of other materials and detectors resolution, are summarized.

3.7.1 Momentum spread and emittance of primary beam

One of the major sources of experimental resolution is the momentum spread of the primary beam ($\delta p_{\mathrm{primary}}$). As explained in Sect. 2.5.5, the applied dispersion of the beam transfer line was measured to be 28 mm/%, which is significantly smaller than the designed value to achieve the dispersion matching conditions. The effect on the resolution can not be fully eliminated, and the resultant effect is evaluated using the first order transfer matrix to be

$$\left(C + (x_{\mathrm{F5}}|x_{\mathrm{F0}})\frac{(x_{\mathrm{F0}}|\delta)}{(x_{\mathrm{F5}}|\delta)}\right)\delta p_{\mathrm{primary}} = \left(1.31 - 1.92 \times \tfrac{28}{62.42}\right)\delta p_{\mathrm{primary}} \tag{3.16}$$

$$\simeq 0.45 \times \delta p_{\mathrm{primary}}\%. \tag{3.17}$$

The value of $(x_{\mathrm{F5}}|x_{\mathrm{F0}})$ is calculated as $1/(a_{\mathrm{F5}}|a_{\mathrm{F0}})$, because $(x_{\mathrm{F5}}|x_{\mathrm{F0}}) \times (a_{\mathrm{F5}}|a_{\mathrm{F0}}) = 1$ from the Liouville's theorem. The momentum spread is estimated to be 0.03 %(RMS) as mentioned in Sect. 2.3. Thus estimated contribution to the experimental resolution is $\approx$ 220 keV (FWHM).

3.7.2 Multiple scattering at vacuum windows

Uncertainties of measured angles also contribute to the energy resolution, mainly through the fact that the focal plane at F5 is largely tilted by about 87 degrees in a horizontal plane. One of the largest sources of the uncertainties is the multiple scattering, σ_θ, at the 50 μm thick stainless steel window located at the exit of the vacuum pipe of the upstream of the F5 chamber. The magnitude of σ_θ is estimated to be 2.2 mrad by a simulation code ATIMA[13]. The resultant contribution to the resolution from the angular uncertainty through the tilted focal plane expressed by the finite value of matrix element $(x_{\mathrm{F5}}|a_{\mathrm{F0}}\delta)$ is evaluated to be

---

[13] ATIMA is a program developed at GSI which calculates various physical quantities characterizing the slowing down of protons and heavy ions in matter for specific kinetic energies ranging from 1 keV/u to 450 GeV/u.

$$\left|\frac{(x_{\mathrm{F5}}|a_{\mathrm{F0}}) + (x_{\mathrm{F5}}|a_{\mathrm{F0}}\delta)\delta}{(a_{\mathrm{F5}}|a_{\mathrm{F0}})} - 0.127\right| \sigma_\theta = |0.66 + 1.5\delta| \times 2.2 \tag{3.18}$$

$$= 3.3 \times |0.44 + \delta|\,[mm], \tag{3.19}$$

which is equivalent to the energy dependent resolution of 360 × $|0.44 + \delta|$ keV (FWHM). The term within the absolute-value sign in the l.h.s. represents the distance between the stainless steel window and focal plane as a function of δ.

Above equation is showing that the best resolution is achieved at the point $\delta = -0.44\%$, which corresponds to $E_{\mathrm{ex}} = 139.7$ MeV for ^{121}Sn and $E_{\mathrm{ex}} = 141.6$ MeV for ^{116}Sn. The dependencies are reconfirmed in the following simulation with more realistic conditions including the multiple scattering by the air and the materials in the MWDCs.

3.7.3 Reaction point distribution in the target

The reaction point in the target along the beam direction is not measured and is also one of the main contributions for the resolution, because the energy loss of the deuteron and that of the ^{3}He are different by about factor 6, which comes from difference of charge (1 : 4) and velocity β (0.61 : 0.46). As a result, the contribution of the uncertainty of the reaction point becomes about 100 keV (FWHM).

3.7.4 Resolution estimation by Monte Carlo simulation

In order to study more in detail the expected experimental resolution, we performed a Monte Carlo simulation. In the simulation, resolution is estimated for its dependence on the excitation energy E_{ex}. Overall simulation procedure is the same as that for Sect. 3.3.4. The procedures are briefly described as follows.

(a) Simulation of the ^{122,117}Sn$(d, ^3\mathrm{He})$ reaction at F0

Simulate the ^{122,117}Sn$(d, ^3\mathrm{He})$ reaction at the F0 target. Input values are the beam properties (Sect. 2.3), the dispersion of the beam transfer line (Sect. 2.5.5), and the size of the target (Sect. 2.3.2). Emitted ^{3}He momentum is calculated by assuming an excitation energy in the reaction E_{ex} as input parameter ($\equiv E_{\mathrm{ex}}^{\mathrm{input}}$), and the reaction angle $\theta_{\mathrm{reaction}}$ observing the relation in Sect. 3.4.2. Theoretically calculated reaction angle dependence of the production cross section [20] is taken into account for pionic s and p states.

(b) Transportation from F0 to F5

The emitted ^{3}He in the reactions are transported to F5. The parameters at F0 (δ, a_{F0} and b_{F0}) are transformed to parameters at F5 (x_{F5}, a_{F5} and b_{F5}) according to Eq. 3.4–3.6. The transmission probability (Sect. 3.5.2), the energy loss, the multiple scattering in the target and the F5 materials (stainless steel window, air, and MWDCs), and the smearing effect of the MWDC analysis are taken into account.

(c) Comparison of deduced E_{ex} and deduction of resolution

We analyze the simulated data in the same manner as for the experimental data and deduce E_{ex} and θ. Here, to secure same condition as for the experimental data, we require a_{F0} to be less than 15 mrad. The obtained distribution of E_{ex} are compared with $E_{\mathrm{ex}}^{\mathrm{input}}$ to evaluate the experimental resolution. In comparison, we consider the resolution dependencies on the deduced excitation energies E_{ex} and the reaction angles θ.

Figure 3.32 shows a sample histogram of difference between the deduced excitation energies and given input $E_{\mathrm{ex}} - E_{\mathrm{ex}}^{\mathrm{input}}$ for a range of $0 < \theta < 1.5^\circ$ at the excitation energies of $E_{\mathrm{ex}} = 139$ (red) and $E_{\mathrm{ex}} = 136$ (blue). Similar histograms are created for different ranges of reaction angles and excitation energies to achieve the dependencies.

3.7.5 Estimated experimental resolution

The simulation results are shown in Fig. 3.33. The resolution is estimated for different excitation energies E_{ex} and different angular ranges as plotted.

As described, the resolution is dominantly contributed from the primary beam momentum spread σ_δ and the multiple scattering σ_θ. So, their precision directly influences the resolution estimation. The estimated σ_δ has a relative error of $\pm$ 20% as shown in Sect. 2.3.2, and this error is properly evaluated in the resolution estimation by repeating the above procedure with variations of the values within the error as described below. For the multiple scattering σ_θ, we assumed a relative error of 10% to safely cover the error of the estimated values and the accuracy of the material thickness. The values are estimated by ATIMA code which interpolates experimentally known values and is known to reproduce experimental values within an error of a few percent.

The influences on the experimental resolution are estimated by repeating the simulation with two conditions, "σ_δ : +20%, σ_θ : +10%" and "σ_δ : −20%, σ_θ : −10%" as shown in Fig. 3.34. The resolution varies by $\simeq \pm 20$ keV in whole range, and this variation is considered as a part of the systematic errors of the resolution.

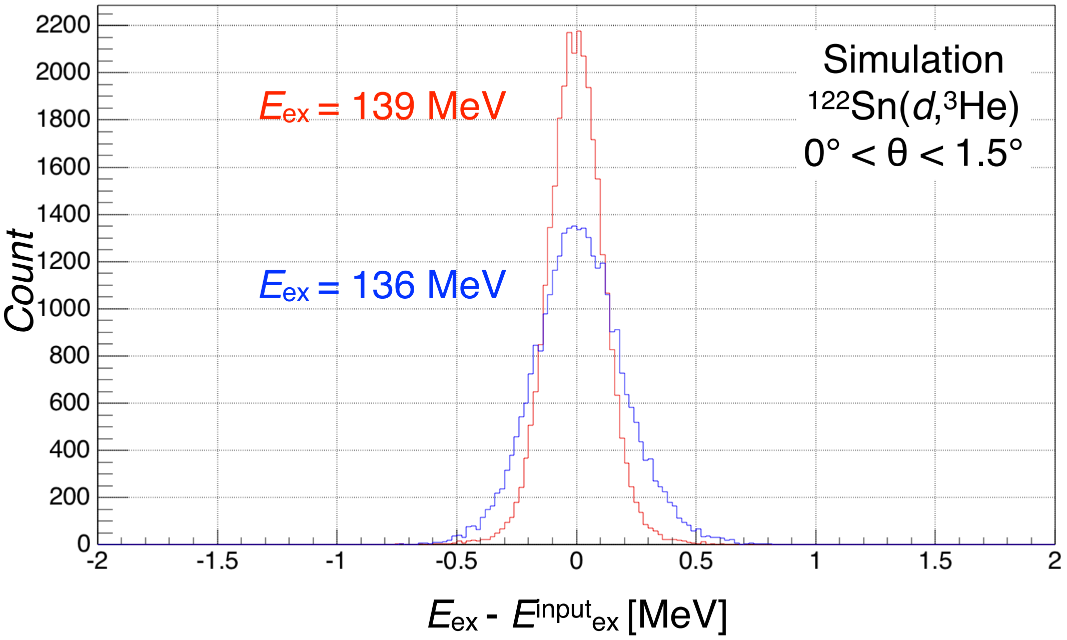

FIGURE 3.32: Histograms of $E_{\mathrm{ex}} - E_{\mathrm{ex}}^{\mathrm{input}}$ of s state in ^{121}Sn for range of $0 < \theta < 1.5°$ and for $E_{\mathrm{ex}} = 139$ (red) / $E_{\mathrm{ex}} = 136$ (blue) in the simulation. The widths of the distributions depend on the E_{ex}.

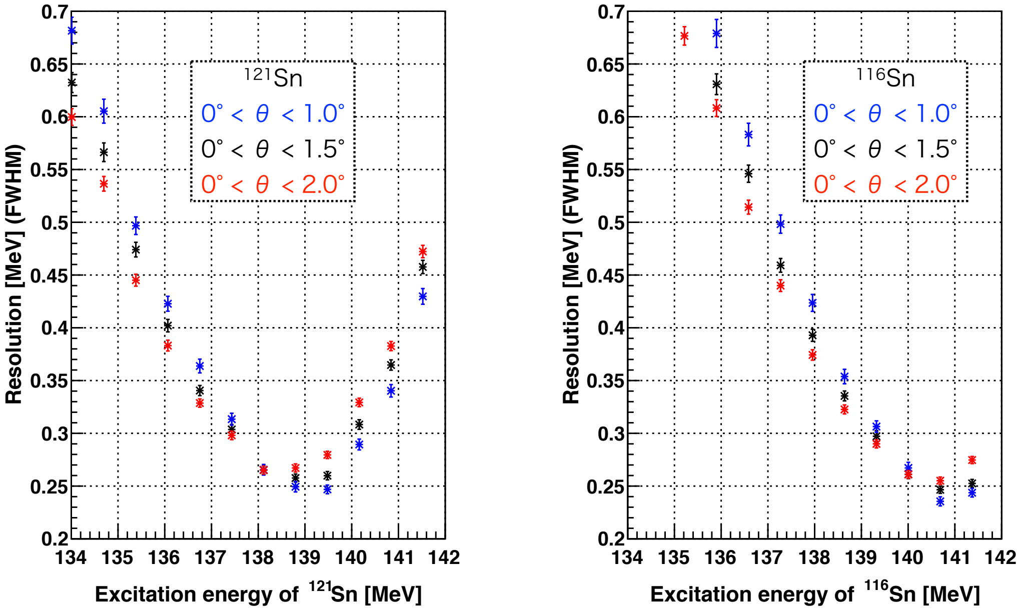

FIGURE 3.33: (Left) Resolution for E_{ex} of ^{121}Sn in $0° < \theta < 1.5°$ (Right) Resolution for E_{ex} of ^{116}Sn in $0° < \theta < 1.5°$. The minimized points correspond to the position of the stainless steel window for the vacuum pipes in the upstream of F5 chamber.

In the Monte-Carlo simulation, time dependence of the detector properties, such as position or angular resolution are not considered, because (i) the contribution of the detector properties are negligibly small compared with the those from the primary beam momentum spread and the multiple scattering. (ii) this experiment was performed in underground where the environment, such as the humidity or the temperature, are stable.

In Appendix B, the reproducibility of spectral peak structure width with different angle and position are demonstrated. As described in the appendix, measured 1*s* peak width of ^{121}Sn strongly depends on the measured positions and angles. Analysis based on above estimated position and angle dependent spectral resolution yielded the deduced width staying almost constant and showing a slight shift at a deviated position and a deviated angle. The shifts are confirmed to be consistent with the statistical and systematic errors, which are discussed in the subsequent analysis.

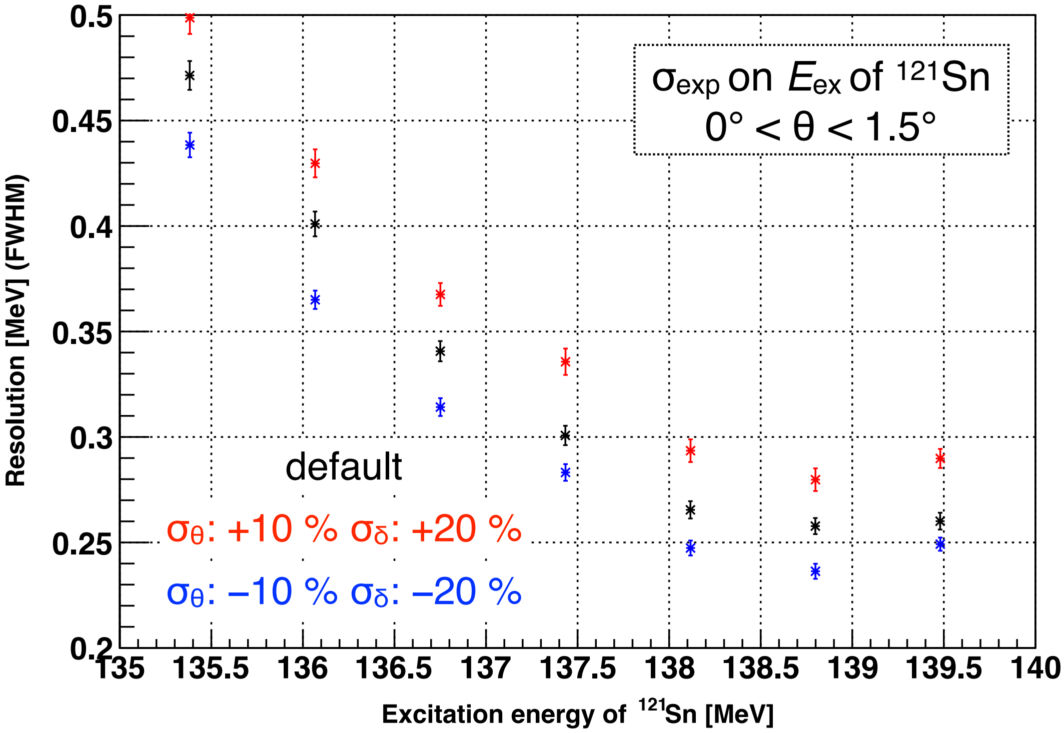

FIGURE 3.34: The simulated resolution with (i) the calculated multiple scattering and measured momentum spread (default) (ii) 10% larger multiple scattering and 20% larger momentum spread (red) (iii) 10% smaller multiple scattering and 20% smaller momentum spread. These result are used for the estimation of the systematic errors.

Chapter 4

Results and Discussion

In this chapter, we discuss the obtained spectra and physical results. In Sect. 4.1, the excitation spectra are decomposed to contributions from different configurations of the pionic states and neutron holes states by elaborate fitting of the spectra, and the binding energy and the width of each pionic state are deduced. Systematic errors and methods to attain much better accuracy is also discussed in Sect. 4.2. In Sect. 4.3, the excitation spectra in different reaction angles are presented and the reaction angular dependences of the formation cross section are deduced. Finally, we discuss experimentally achieved constraints on the pion-nucleus interaction and accomplished knowledge on the in-medium partial restoration of chiral symmetry.

4.1 Deduction of binding energies and widths

The achieved excitation spectra are composed of spectral functions of several different configurations of pionic states and neutron holes states. In order to deduce the binding energies and widths, the excitation spectra are decomposed by fitting with theoretically calculated spectral functions [11, 20] explained in the following section.

4.1.1 Fitting function

The fitting function consists of a background function and signal components and is represented in the equation,

$$F_{\mathrm{all}}(E_{\mathrm{ex}}) = F_{\mathrm{bg}}(E_{\mathrm{ex}}) + \Sigma_{nl} F_{nl}(E_{\mathrm{ex}} - B_{nl}, \Gamma_{nl}, \theta), \tag{4.1}$$

where F_{bg} and F_{nl} are the function of the background and the double-differential formation cross section of the pionic atoms, respectively; B_{nl} and Γ_{nl} are the binding energies and widths of the pionic (n_π, l_π) states in the fitting such as (1,s) and (2,p); E_{ex} and θ are the excitation energy of daughter nuclei and reaction angle at the laboratory frame. The background is assumed to be linear. Note that the quasi-free components are not included in the function, which start to contribute around E_{ex} = mass of charged pion (139.57 MeV). To avoid the contamination from the quasi-free components, the fit range is set to be $<$ 139 MeV. Because the resolution around 139 MeV is estimated to be 250 keV (FWHM) (See Sect. 3.7), the distance of 600 keV is enough to separate the fitting range from the contribution of quasi-free components. The spectral functions F_{nl} for each (n_π, l_π) are given as

$$\mathrm{F}_{nl}(E_{\mathrm{ex}} - B_{nl}, \Gamma_{nl}, \theta) = A_{nl} \times \Sigma_{j_n} N_{\mathrm{eff}}^{(nl\otimes j_n)}(\theta) \mathrm{Voigt}(E_{\mathrm{ex}} - B_{nl} - \Delta S_{j_n}^{n}, \Gamma_{nl}, \sigma_{\mathrm{exp}}). \tag{4.2}$$

Here, A_{nl} represents the magnitude of formation cross section of each pionic state, j_n a quantum number of neutron hole state such as $3s_{1/2}$, $N_{\mathrm{eff}}^{(nl\otimes j_n)}(\theta)$ an effective neutron number for a combination of a pionic state (n_π, l_π) and a neutron hole state j_n at reaction angles θ, $\Delta S_{j_n}^{n}$ a separation energy difference of j_n neutron hole state from that of the ground state of ^{121}Sn, and σ_{exp} experimental spectral resolution described in Sect. 3.7. The shape of the double-differential formation cross section distribution of each configuration is represented by Voigt function. In the fitting, we considered the contributions of pionic $1s$, $2p$ and $2s$ states, which are dominant in the region of interest. The contribution of $3p$ and $3s$ states are also taken into account to reproduce the structure around π^- emission threshold.

In the fitting, A_{nl}, B_{nl} and Γ_{nl} are the fitting parameters as described below. The spectral response function from each pionic state reflects contributions of different neutron hole states as $N_{\mathrm{eff}}^{(nl\otimes j_n)}(\theta)$. Here, the $N_{\mathrm{eff}}^{(nl\otimes j_n)}(\theta)$ are calculated based on the relative strength of the $^{122,117}\mathrm{Sn}(d,t)$ reaction cross sections [39, 40]. Some of $N_{\mathrm{eff}}^{(nl\otimes j_n)}(\theta)$ are treated as free parameters in the fittings to determine the binding energies accurately, while other insensitive $N_{\mathrm{eff}}^{(nl\otimes j_n)}(\theta)$ are fixed to the calculated values. The calculated values of $N_{\mathrm{eff}}^{(nl\otimes j_n)}(\theta)$, $\Delta S_{j_n}^{n}$ and experimental resolutions are summarized in Appendix C.

4.1.2 Fitting results of ^{121}Sn excitation spectrum

The binding energies and widths of pionic states are deduced in the fitting of the spectrum in $0° < \theta < 1.5°$. The data in $1.5° < \theta$ are excluded in the analysis to suppress the effect of optical higher order aberration. Figure 4.1a shows the fitted excitation spectrum of ^{121}Sn for the reaction angles of $0° < \theta < 1.5°$. The fitting range is shown by the vertical dashed lines at (133, 139) MeV. The π^- emission threshold is shown by the red dashed line. The light-green solid curve is the fitting curve. The contribution of each pionic state is represented with differently colored dashed curve.

Each contribution of a pionic state has subcomponents of six neutron hole states. Table 4.1 shows the N_{eff} and $\Delta S^n_{j_n}$ of neutron holes used in the fitting function of the pionic $1s$ state. As shown in the table, $(3s_{1/2})_n^{-1}$ and two $(2d_{5/2})_n^{-1}$ states are dominant for the $1s$ contribution. The subcomponent of $1s$ state around $E_{\text{ex}} = 137$ MeV shown in the red dashed curve in Fig. 4.1a is consist of two $(2d_{5/2})_n^{-1}$ states and a $(1g_{7/2})_n^{-1}$ state, which are overlapped by the main contribution of the $2p$ pionic state. To determine the binding energies of $2p$ state precisely, the N_{eff} of these three neutron hole states are treated as fitting parameters. N_{eff} of other neutron hole states are fixed to the theoretically calculated values. We also fix the width of pionic $2s$ state and the binding energies and widths of of $3s$ and $3p$ states to the theoretical values in Table 1.5, because these values are insensitive to the fitting result.

The numerical fitting results for the pionic ^{121}Sn are summarized in Table 4.2. In the table, magnitude of differential formation cross sections for each pionic state are deduced by integrating the contribution of each neutron hole state. The errors in the table include only statistical errors. The systematic errors are discussed in Sect. 4.2.1. In the subsequent analysis for binding energies and widths, we deal only with $1s$ and $2p$ states, because $2s$ and other states are not resolved.

As discussed later, parameters in the pion-nucleus optical potential are deduced from B_{1s} and Γ_{1s}. In addition to these values, the B_{2p} are also utilized to suppress the systematic errors. As shown in Sect. 4.2.1, major part of systematic errors arise from the determination of the absolute energies. By taking an energy difference between two states, we can safely suppress the systematic errors and achieve much accurate values. Note that the correlation coefficients in the fitting among the deduced values of B_{1s}, B_{2p} and Γ_{1s} are confirmed to be sufficiently small.

configuration $(nl)_\pi \otimes (j_n)_n^{-1}$	N^*_{eff} $0^\circ < \theta < 1.5^\circ$	$\Delta S^n_{j_n}$ [MeV]
$(1s)_\pi \otimes (3s_{1/2})_n^{-1}$	1	0.060
$(1s)_\pi \otimes (2d_{3/2})_n^{-1}$	0.081	0.000
$(1s)_\pi \otimes (2d_{5/2})_n^{-1}$	0.107	1.121
$(1s)_\pi \otimes (2d_{5/2})_n^{-1}$	0.059	1.403
$(1s)_\pi \otimes (1g_{7/2})_n^{-1}$	0.002	0.926
$(1s)_\pi \otimes (1h_{11/2})_n^{-1}$	0.0004	0.006

TABLE 4.1: N^*_{eff} and separation energy of each neutron hole state in the contribution of $1s$ pionic states. The N^*_{eff} is defined as the normalized values to $N_{\text{eff}}^{(1s)_\pi \otimes (3s_{1/2})_n^{-1}}$.

pionic states $(nl)_\pi$ in ^{121}Sn	B_{nl} [MeV]	Γ_{nl} [MeV]	$(\mathrm{d}\sigma/\mathrm{d}\Omega)_{nl}$ [μb/sr] in $0^\circ < \theta < 1.5^\circ$
$1s$	3.773 ± 0.003 (stat.)	0.292 ± 0.011 (stat.)	22.54 ± 0.42 (stat.)
$2p$	2.225 ± 0.004 (stat.)	0.183 ± 0.016 (stat.)	15.05 ± 0.68 (stat.)
$2s$	1.369 ± 0.007 (stat.)	0.078 (fixed)	3.99 ± 0.15 (stat.)

TABLE 4.2: Fitting result of ^{121}Sn excitation energy spectrum in $0^\circ < \theta < 1.5^\circ$.

4.1.3 Fitting results of ^{116}Sn excitation spectrum

The fitting result of the excitation spectrum of ^{116}Sn for the reaction angles in $0° < \theta < 1.5°$ is shown in Fig. 4.1b. The distinct structure at $\sim$ 136 MeV is due to the configuration of $(1s)_\pi \otimes (3d_{1/2})_n$, a valence neutron pick up contribution. The daughter nucleus has a close shell and the peak is energetically isolated.

For each pionic state, couplings with 53 neutron hole states are taken into account. The number of considered neutron hole states is much larger than that for ^{121}Sn. All couplings are contributing to the structures > 136.5 MeV, because the configuration of pionic states and neutron hole states become complicated in the case that a neutron is picked up from the core nucleus, not from the valence neutron. In contrast, the structure become clearly isolated from other contributions when a valence neutron is picked up.

Here, the width of $1s$, $2p$ and $2s$ states are fixed to the theoretically calculated values because the experimental resolution is much larger than these values by factor 2 – 4 (See Appendix C). All of N_{eff} is also fixed for ^{116}Sn. The results are summarized in Table 4.3. In the subsequent analysis for binding energies and widths, we deal only with $1s$ state, because $2p$, $2s$ and other states are not resolved clearly as with the $2s$ state in ^{121}Sn.

pionic states $(nl)_\pi$ in ^{116}Sn	B_{nl} [MeV]	Γ_{nl} [MeV]	$(\mathrm{d}\sigma/\mathrm{d}\Omega)_{nl}$ [μb/sr] in $0° < \theta < 1.5°$
$1s$	3.817 ± 0.012 (stat.)	0.357 (fixed)	19.10 ± 0.53 (stat.)
$2p$	2.230 ± 0.014 (stat.)	0.123 (fixed)	17.80 ± 1.22 (stat.)
$2s$	1.346 ± 0.025 (stat.)	0.092 (fixed)	3.96 ± 0.41 (stat.)

Table 4.3: Fitting result of ^{116}Sn excitation energy spectrum in $0° < \theta < 1.5°$.

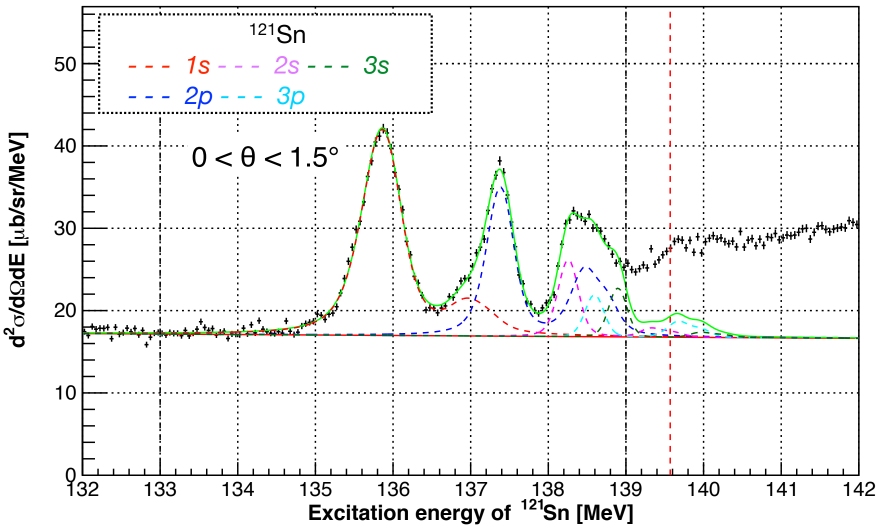

(A) Excitation spectrum of ^{121}Sn for $0° < \theta < 1°$ and the fitting results.

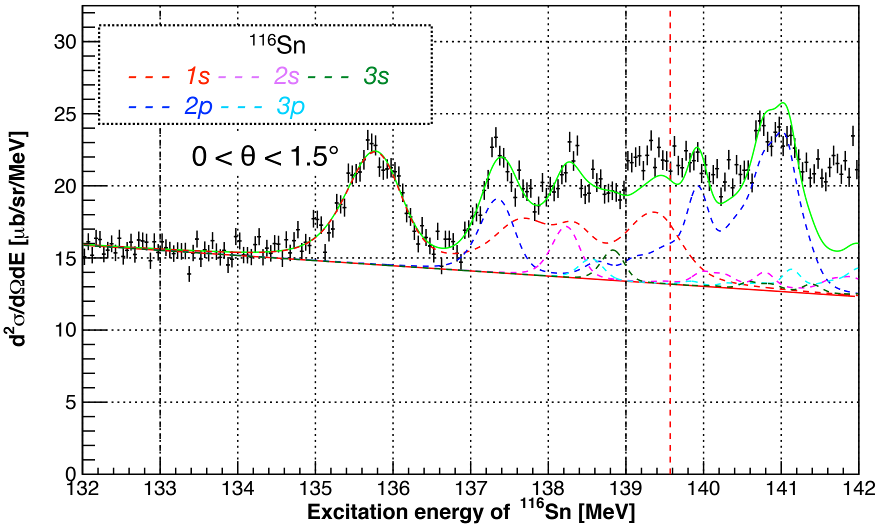

(B) Excitation spectrum of ^{116}Sn for $0° < \theta < 1.5°$ and the fitting results.

FIGURE 4.1: Excitation spectrum of ^{121,116}Sn for forward angular regions and the fitting results. The range of the reaction angles are $0° < \theta < 1.5°$. The green solid line is the sum of contributions of the pionic states. The other colored dashed lines correspond to each contribution of the pionic state as shown in the figures. The fitting are performed between the vertical black dashed lines (133–139 MeV). The red vertical dashed lines correspond to the quasi-free π^- emission threshold. The χ^2/ndf of the fitting are 192.1/119 and 161.0/119, respectively.

4.2 Evaluation of systematic errors

4.2.1 Systematic errors of binding energies

Following five factors are considered in the evaluation of the systematic errors of the binding energies: (i) fitting range of E_{ex} and θ_{reaction}, (ii) energy calibration, (iii) target thickness, (iv) energy uncertainty of the primary beam and (v) uncertainties of transfer matrix elements. Contributions of other factors such as energy resolution or acceptance correction are evaluated to be negligibly small.

(i) Fitting range

The upper and lower edge of fitting range in E_{ex} spectra are changed from 138 to 139 MeV and 132 to 133, respectively. The range of θ is also changed from $0 < \theta < 1^\circ$ to $0 < \theta < 2^\circ$. Both affect the binding energies by less than 2 keV.

(ii) Energy calibration

The energy calibration in the $p(d, {}^3\text{He})\pi^0$ reaction contributes ± 3 (stat.)$^{+0.3}_{-7.0}$ (sys.) keV as discussed in Sect. 3.4.1. Both statistical and systematic errors in the energy calibration are combined as a systematic error for absolute energy scale.

(iii) Target thickness

The target thicknesses are 12.5 ± 0.5 mg/cm^2 for the target ^{122}Sn and 9.9 ± 0.5 mg/cm^2 for the target ^{117}Sn. The systematic error arising from the target thickness is evaluated to be 4 keV for the both of the targets.

(iv) Primary beam energy

The primary beam energy is measured by NMR in dipoles in BigRIPS by adjusting the rigidity of BigRIPS to the primary beam. To evaluate the accuracy of NMR, we compared the momentum of ^{3}He measured by NMR and that determined by $p(d, {}^3\text{He})\pi^0$ on polyethylene target. As a result we found a difference of about 200 keV. This value is treated as uncertainty of the primary beam energy. Note that the effect of the primary beam energy uncertainty is indirect to the excitation energy. Taking a relative position to the calibration peak measured by $p(d, {}^3\text{He})\pi^0$ reactions, a factor 1/10 must be multiplied because of the similarity of the kinematical conditions. As a result, the systematic error coming from the primary beam energy is about 20 keV.

(v) Uncertainties of transfer matrix elements

To evaluate the systematic errors arising from the transfer matrix, we slightly change the value of each transfer matrix element within the error listed in Table 3.1 and repeat the three procedures committed by the transfer matrix:(a) conversion of the F5 parameters x_{F5}, a_{F5}, b_{F5} to δ, a_{F0} and b_{F0}, (b) excitation energy calibration, and (c) resolution estimation. After these procedures the binding energies are deduced by the decomposition of the excitation spectra, and the evaluated deviation of the binding energies are taken into account as systematic errors arising from the uncertainties of transfer matrix elements. The systematic errors originating from the calculated optical elements, $(a_{\mathrm{F5}}|a_{\mathrm{F0}}\delta)$, $(b_{\mathrm{F5}}|b_{\mathrm{F0}}\delta)$ and $(b_{\mathrm{F5}}|b_{\mathrm{F0}}\delta^2)$, are evaluated by the analysis in wider range as discussed in Sect. 3.3.5. The resulting systematic errors in the binding energies are summarized in Table 4.4. The correlations among the elements are sufficiently small, except for these pairs: $(x_{\mathrm{F5}}|a_{\mathrm{F0}})$, $(x_{\mathrm{F5}}|a^3_{\mathrm{F0}})$ and $(x_{\mathrm{F5}}|\delta)$, $(x_{\mathrm{F5}}|\delta^2)$. The errors from these pairs are calculated based on the correlation coefficients. The results are also shown in the tables. The dominant errors in each value are represented in bold font. As shown, the effect from $(x_{\mathrm{F5}}|\delta)$ and $(x_{\mathrm{F5}}|\delta^2)$ has a major contribution for the determination of binding energies through the energy calibration.

4.2.2 Systematic errors of binding energy difference

To suppress the systematic errors, we take the energy difference of $1s$ and $2p$ states. Taking difference between binding energies of different pionic states, many of the sources of the systematic errors are compensated and we achieve a much accurate value. The subtraction leads to suppression of the systematic errors mainly from the calibration peak, the primary beam energy uncertainty and target thickness uncertainty. The errors from uncertainties of transfer matrix elements, especially from $(x_{\mathrm{F5}}|\delta)$ and $(x_{\mathrm{F5}}|\delta^2)$, also become much smaller. It is because the uncertainties of these elements affect mainly though the determination of the calibration peak position. As shown in the Table 4.4, the systematic errors caused by $(x_{\mathrm{F5}}|\delta)$ and $(x_{\mathrm{F5}}|\delta^2)$ are about 10 keV for the energy difference of $1s$ and $2p$ states in ^{121}Sn, while about 60 keV or more for the absolute binding energies of $1s$ or $2p$ states.

elements	^{121}Sn						^{116}Sn	
	ΔB$_{1s}$		ΔB$_{2p}$		Δ(B$_{1s}$ - B$_{2p}$)		ΔB$_{1s}$	
$(x_{\mathrm{F5}}\|a^2_{\mathrm{F0}})$	+4	−9	+4	−9	<1	>-1	+4	−8
$(x_{\mathrm{F5}}\|b_{\mathrm{F0}})$	<1	−2	<1	−2	<1	>-1	<1	−2
$(x_{\mathrm{F5}}\|b^2_{\mathrm{F0}})$	+3	−2	+3	−2	<1	>-1	+5	−1
$(x_{\mathrm{F5}}\|a_{\mathrm{F0}}b^2_{\mathrm{F0}})$	+3	−3	+2	>-1	<1	−3	+2	−2
$(x_{\mathrm{F5}}\|a_{\mathrm{F0}}\delta)$	<1	−11	<1	−11	<1	−1	+3	−11
$(x_{\mathrm{F5}}\|a^2_{\mathrm{F0}}\delta)$	<1	−6	<1	−9	+3	−4	<1	−6
$(a_{\mathrm{F5}}\|a_{\mathrm{F0}})$	<1	−7	<1	−8	+1	>-1	+3	−2
$(b_{\mathrm{F5}}\|b_{\mathrm{F0}})$	+2	−11	+3	−11	<1	>-1	+1	−9
$(x_{\mathrm{F5}}\|a_{\mathrm{F0}})$, $(x_{\mathrm{F5}}\|a^3_{\mathrm{F0}})$	<1	−13	+2	−14	+1	−4	<1	−13
$(x_{\mathrm{F5}}\|\delta)$, $(x_{\mathrm{F5}}\|\delta^2)$	**+59**	**−65**	**+66**	**−77**	**+12**	**−8**	**+48**	**−49**
$(a_{\mathrm{F5}}\|a_{\mathrm{F0}}\delta)$	± 2		± 4		± 2		± 2	
$(b_{\mathrm{F5}}\|b_{\mathrm{F0}}\delta)$								
$(b_{\mathrm{F5}}\|b_{\mathrm{F0}}\delta^2)$								

TABLE 4.4: The systematic errors of binding energies of pionic states from transfer matrix elements. The values written in bold font are dominant for the error of each binding energy.

4.2.3 Systematic errors of natural widths

For the determination of the natural widths, following 2 factors are considered in the evaluation of the systematic errors: (i) uncertainties of the transfer matrix elements, as explained for the binding energies and (ii) the ambiguity of the resolution from the uncertainty of the magnitude of multiple scattering and beam momentum spread.

(i) Uncertainties of transfer matrix elements

The systematic errors arising out of the uncertainties of the transfer matrix elements are evaluated with the same method explained in (v) of Sect. 4.2.1. The results are summarized in Table 4.5. The contribution of $(x_{\mathrm{F5}}|a_{\mathrm{F0}})$ and $(x_{\mathrm{F5}}|a^3_{\mathrm{F0}})$ is as large as that from $(x_{\mathrm{F5}}|\delta)$ and $(x_{\mathrm{F5}}|\delta^2)$ for Γ_{1s}, while the contribution of the higher order elements $(a_{\mathrm{F5}}|a_{\mathrm{F0}}\delta)$, $(b_{\mathrm{F5}}|b_{\mathrm{F0}}\delta)$ and $(b_{\mathrm{F5}}|b_{\mathrm{F0}}\delta^2)$ is also large for error of Γ_{2p}. This is because (a) the pionic $2p$ state is enhanced in the larger angular region as shown in the following section, where the effects of higher order optical elements become significant (b) the value of Γ_{2p} is relatively small compared with the resolution; therefore the effect of these elements on the resolution cause a large error of Γ_{2p}.

(ii) Uncertainties of multiple scattering and beam momentum spread

The ambiguity of the resolution from the uncertainties of the magnitude of multiple scattering and beam momentum spread are also taken into account, which is described in Sect. 3.7.5. The systematic errors from this ambiguity is evaluated from the fitting with two cases shown in Fig. 3.34. The evaluated systematic errors on natural widths are +34 −27 keV for Γ_{1s} and +17 −31 keV for Γ_{2p}.

elements	^{121}Sn			
	$\Delta\Gamma_{\mathrm{1s}}$		$\Delta\Gamma_{\mathrm{2p}}$	
$(x_{\mathrm{F5}}\|a^2_{\mathrm{F0}})$	$+4$	>-1	$+3$	>-1
$(x_{\mathrm{F5}}\|b_{\mathrm{F0}})$	<1	-4	<1	-3
$(x_{\mathrm{F5}}\|b^2_{\mathrm{F0}})$	<1	>-1	<1	-3
$(x_{\mathrm{F5}}\|a_{\mathrm{F0}}b^2_{\mathrm{F0}})$	$+6$	-4	$+5$	-3
$(x_{\mathrm{F5}}\|a_{\mathrm{F0}}\delta)$	$+2$	-4	<1	-3
$(x_{\mathrm{F5}}\|a^2_{\mathrm{F0}}\delta)$	$+4$	>-1	$+2$	-1
$(a_{\mathrm{F5}}\|a_{\mathrm{F0}})$	$+8$	-4	$+2$	-6
$(b_{\mathrm{F5}}\|b_{\mathrm{F0}})$	<1	-5	<1	-9
$(x_{\mathrm{F5}}\|a_{\mathrm{F0}})$, $(x_{\mathrm{F5}}\|a^3_{\mathrm{F0}})$	**+9**	**−12**	**+6**	>-1
$(x_{\mathrm{F5}}\|\delta)$, $(x_{\mathrm{F5}}\|\delta^2)$	**+15**	**−21**	**+9**	**−28**
$(a_{\mathrm{F5}}\|a_{\mathrm{F0}}\delta)$	±4		**±30**	
$(b_{\mathrm{F5}}\|b_{\mathrm{F0}}\delta)$				
$(b_{\mathrm{F5}}\|b_{\mathrm{F0}}\delta^2)$				

Table 4.5: The systematic errors of natural widths of pionic states in ^{121}Sn from uncertainties of the transfer matrix elements. The values written in bold font are dominant for the error of each binding energy.

4.2.4 Binding energy, natural width, and binding energy difference

The deduced binding energies, binding energy differences and natural widths are summarized in Table 4.6. The theoretical values based on the calculation explained in Sect. 1.5 are also listed in the table. In these calculations, adopted optical potential parameters are based on the unified analysis of pionic atom with light nuclei and low-energy pion nucleus scattering[21]. In principle experimental data agree with theoretical values, and the largest discrepancy is found for Γ_{2p} in ^{121}Sn to the 1.5 σ, which is not statistically significant. In the further analysis B_{1s}, Γ_{1s} and $B_{1s} - B_{2p}$ are utilized for the determination of optical parameters in Sect. 4.4.3, taking into consideration the correlation between the evaluated systematic errors.

	fit result of experimental data	theoretical prediction
B_{1s} (^{121}Sn) [MeV]	$+3.773 \pm 0.003$(stat.) $^{+0.063}_{-0.073}$(sys.)	$+3.787$
B_{2p} (^{121}Sn) [MeV]	$+2.225 \pm 0.004$(stat.) $^{+0.070}_{-0.085}$(sys.)	$+2.257$
B_{1s} (^{116}Sn) [MeV]	$+3.817 \pm 0.012$(stat.) $^{+0.053}_{-0.058}$(sys.)	$+3.884$
B_{1s} - B_{2p} (^{121}Sn) [MeV]	$+1.547 \pm 0.005$(stat.) $^{+0.013}_{-0.010}$(sys.)	$+1.531$
B_{2s} - B_{2p} (^{121}Sn) [MeV]	-0.856 ± 0.008(stat.) $^{+0.019}_{-0.010}$(sys.)	-0.848
Γ_{1s} (^{121}Sn) [MeV]	0.292 ± 0.011(stat.)$^{+0.042}_{-0.035}$(sys.)	$+0.306$
Γ_{2p} (^{121}Sn) [MeV]	0.183 ± 0.016(stat.)$^{+0.048}_{-0.046}$(sys.)	$+0.110$

Table 4.6: Summary of deduced energies, energy differences and natural widths of pionic ^{121,116}Sn.

4.3 Deduction of formation cross section

4.3.1 Formation cross section of pionic 1*s* and 2*p* states

The differential formation cross sections of pionic states are deduced by integrating the fitted contributions of each configuration of a pion and a neutron hole. Angular dependent cross sections are also deduced after the decomposition.

The excitation spectra of ^{121}Sn are divided to four reaction angle regions, $0.0° < \theta < 0.5°$, $0.5° < \theta < 1.0°$, $1.0° < \theta < 1.5°$ and $1.5° < \theta < 2.0°$ as shown in Fig. 4.2. The excitation spectra of ^{116}Sn are divided to three reaction angle regions, $0.0° < \theta < 1.0°$, $1.0° < \theta < 1.5°$ and $1.5° < \theta < 2.0°$[1] as shown in Fig. 4.3. The definition of each colored lines are same as for Fig. 4.1a. The fitting results are also shown in the figure. After integration of pionic components, reaction angle dependent formation cross sections of pionic states are deduced as tabulated in Table 4.7. Note that in the angular region of $1.5° < \theta < 2.0°$, the fitting functions do not reproduce the experimental spectra as good as in the smaller angular region. This is because the effect of uncertainties of the transfer matrix elements is much stronger than in the smaller angular region[2], and the distortion of the spectral shape becomes not negligible. Therefore the experimental data from this region are treated just for reference in the subsequent analysis.

---

[1] The region $0.0° < \theta < 0.5°$ and $0.5° < \theta < 1.0°$ are combined, because the number of events are too small.

[2] i.e. ΔB_{2p} from $(x_{\mathrm{F5}}|b^2_{\mathrm{F0}})$ in Table 4.4 is increased from 2 keV in $0° < \theta < 1.5°$ to 10 keV in $1.5° < \theta < 2.0°$.

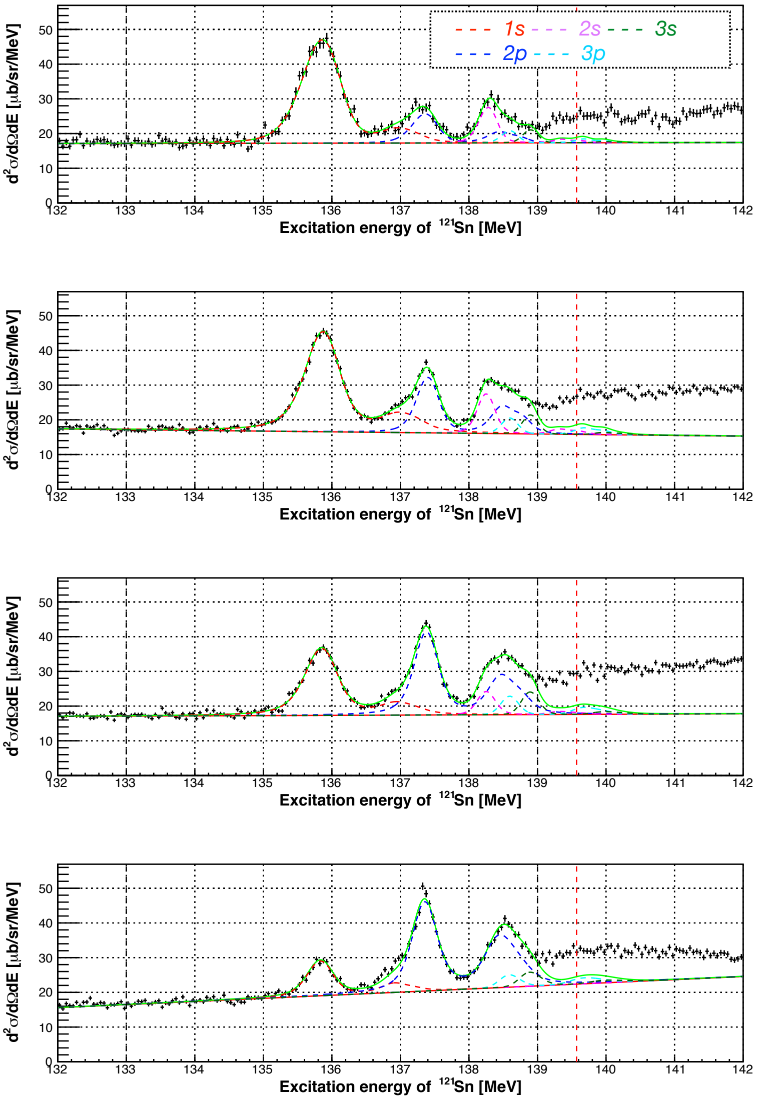

FIGURE 4.2: Excitation spectrum of ^{121}Sn and the fitting results for the different reaction angles.
(Top) 0° $< \theta <$ 0.5° (Second from the top) 0.5° $< \theta <$ 1.0° (Third from the top) 1.0° $< \theta <$ 1.5° (Bottom) 1.5° $< \theta <$ 2.0°. The blue solid line is the sum of contributions of pionic states. The red, pink and green dashed lines represent the contribution of $1s$, $2s$ and $3s$ states. The blue and sky-blue dashed lines represent the contribution of $2p$ and $3p$ states. The fitting are performed between the vertical black dashed lines. The red vertical dashed lines correspond to the quasi-free π^- emission threshold.

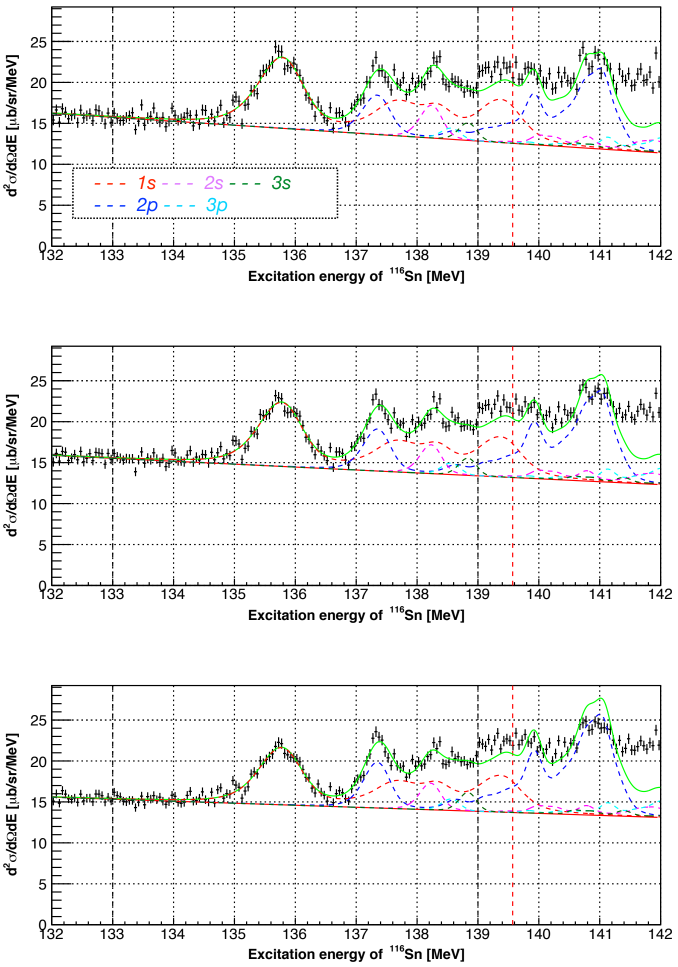

FIGURE 4.3: Excitation spectrum of ^{116}Sn and the fitting results for the different reaction angles.
(top) $0° < \theta < 1.0°$ (middle) $1.0° < \theta < 1.5°$ (bottom) $1.5° < \theta < 2.0°$. The blue solid line is the sum of contributions of pionic states. The red, pink and green dashed lines represent the contribution of $1s$, $2s$ and $3s$ states. The blue and sky-blue dashed lines represent the contribution of $2p$ and $3p$ states. The fitting are performed between the vertical black dashed lines. The red vertical dashed lines correspond to the quasi-free π^- emission threshold.

pionic states	$(\mathrm{d}\sigma/\mathrm{d}\Omega)_{nl}$ [μb/sr]			
$(nl)_\pi(^A\mathrm{Sn})$	$0.0° < \theta < 0.5°$	$0.5° < \theta < 1.0°$	$1.0° < \theta < 1.5°$	$1.5° < \theta < 2.0°$
$1s(^{121}\mathrm{Sn})$	26.37 ± 1.05	26.73 ± 0.63	16.67 ± 0.63	7.30 ± 0.54
$2p(^{121}\mathrm{Sn})$	6.35 ± 1.39	12.68 ± 0.73	20.77 ± 1.11	25.75 ± 1.01
$2s(^{121}\mathrm{Sn})$	4.32 ± 0.37	4.91 ± 0.20	2.93 ± 0.27	0.00 + 0.01
$1s(^{116}\mathrm{Sn})$	23.81 ± 0.93		12.45 ± 1.03	7.47 ± 1.14
$2p(^{116}\mathrm{Sn})$	15.29 ± 1.51		20.67 ± 1.90	30.72 ± 2.16
$2s(^{116}\mathrm{Sn})$	5.49 ± 0.58		2.15 ± 0.61	2.35 ± 0.69

TABLE 4.7: Experimentally deduced differential cross sections for different reaction angle regions. Only the statistical errors are shown. The systematic errors are discussed later.

4.3.2 Systematic errors of double-differential cross section

The main sources of the systematic errors arise in (i) the primary beam intensity, (ii) the target thickness (iii) uncertainties of the transfer matrix elements, and (iv) the acceptance correction. In the analysis, the systematic errors of the data in the angular region of $1.5° < \theta < 2.0°$ are not evaluated, because these data are treated as just for reference as mentioned above.

(i) Primary beam intensity

The error of primary beam intensity comes from the ambiguity of the relation between the beam intensity and the count of back scattered particles, which is estimated to be 20%. This error is common for the both of ^{122}Sn and ^{117}Sn targets and all reaction angles.

(ii) Target thickness

The target thicknesses are 12.5 ± 0.5 mg/cm^2 for the target ^{122}Sn and 9.9 ± 0.5 mg/cm^2 for the target ^{117}Sn as mentioned before. The uncertainties correspond to the systematic error of the double-differential cross section of 4% for ^{122}Sn and 5% for ^{116}Sn, respectively. This error is common for the same target and all reaction angles.

(iii) Uncertainties of transfer matrix elements

The systematic errors from the uncertainties of the transfer matrix elements are estimated as the same manner for binding energies and widths. The total contribution are 10 to 20 % in the forward region, while in the larger angular region the contribution becomes larger. The root sum square of all contribution of matrix elements are summarized in Table below. Note that the listed systematic errors are strongly correlated among all of the pionic states and reaction angles.

pionic states	systematic errors from the transfer matrix elements on $(\mathrm{d}\sigma/\mathrm{d}\Omega)_{nl}$ [μb/sr]		
$(nl)_\pi(^{A}\mathrm{Sn})$	$0.0° < \theta < 0.5°$	$0.5° < \theta < 1.0°$	$1.0° < \theta < 1.5°$
$1s(^{121}\mathrm{Sn})$	$+3.88$ -3.46	$+2.39$ -2.17	$+0.58$ -1.20
$2p(^{121}\mathrm{Sn})$	$+2.89$ -2.17	$+2.95$ -2.30	$+2.81$ -3.41
$2s(^{121}\mathrm{Sn})$	$+2.09$ -0.67	$+0.64$ -0.66	$+0.31$ -0.40
$1s(^{116}\mathrm{Sn})$	$+1.16$ -1.70		$+0.72$ -1.38
$2p(^{116}\mathrm{Sn})$	$+1.87$ -3.05		$+2.73$ -1.47
$2s(^{116}\mathrm{Sn})$	$+1.10$ -0.88		$+0.66$ -0.45

TABLE 4.8: The systematic errors on differential cross sections from uncertainties of transfer matrix elements.

(iv) Acceptance

The acceptance, which is defined in Sect. 3.5.2, changes as a function of ^{3}He momenta and ranges within 70–90% in the region of interest. We assume relatively large errors of 70±15 – 90±5% according to the estimated central values. This factor is common for the both of ^{122}Sn and ^{117}Sn targets, while the errors of the factor for the each reaction angle are independent. It is found that the energy dependence of the acceptance is almost linear and the difference of the correction for each bound state is within a few %. Therefore the systematic error of relative acceptance correction for each state is negligible.

4.3.3 Reaction angle dependence of pionic states

Top and bottom graphs of Fig. 4.4 show experimentally determined reaction angle dependences of differential cross sections of $1s$ (red), $2p$ (pink), and $2s$ (blue) states in ^{121}Sn and in ^{116}Sn, respectively. Each line shows theoretically calculated dependence. In order to compare the relative change of the differential cross sections on the reaction angles, the magnitudes of the theoretical calculations are normalized to the experimental data at the leftmost point. The errors independently associated with each reaction angle arising from statistical errors and acceptance corrections are shown by the error bars. The total errors represented by the square brackets are calculated as the root sum square of all errors explained in the previous section and statistical errors. The errors on the reaction angles are also indicated by the brackets, which are caused by the uncertainties of the angular magnifications: $(a_{\mathrm{F5}}|a_{\mathrm{F0}})$ and $(b_{\mathrm{F5}}|b_{\mathrm{F0}})$. The errors in the angular region of $1.5^\circ < \theta < 2.0^\circ$ are not evaluated as mentioned in the previous section.

The measured angular dependence is explained by the theoretical calculations qualitatively. It proposes the assignment of the pionic states in excitation spectra is correct. The difference of angular dependence between s states and p states can be understood from the angular momentum transfer dependence near the recoilless condition. Around $\theta \simeq 0$, the angular momentum transfer is small and the configurations without angular momentum transfer are selectively populated, such as $(1s)_\pi \otimes (3s_{1/2})_n^{-1}$. Meanwhile, with large θ the angular momentum transfer become larger and the configurations with finite angular momentum transfer gradually populated, such as $(2p)_\pi \otimes (3s_{1/2})_n^{-1}$. In the meantime, some data points and theoretical lines show discrepancy such as $2p$ state in ^{116}Sn. We discuss these discrepancies later.

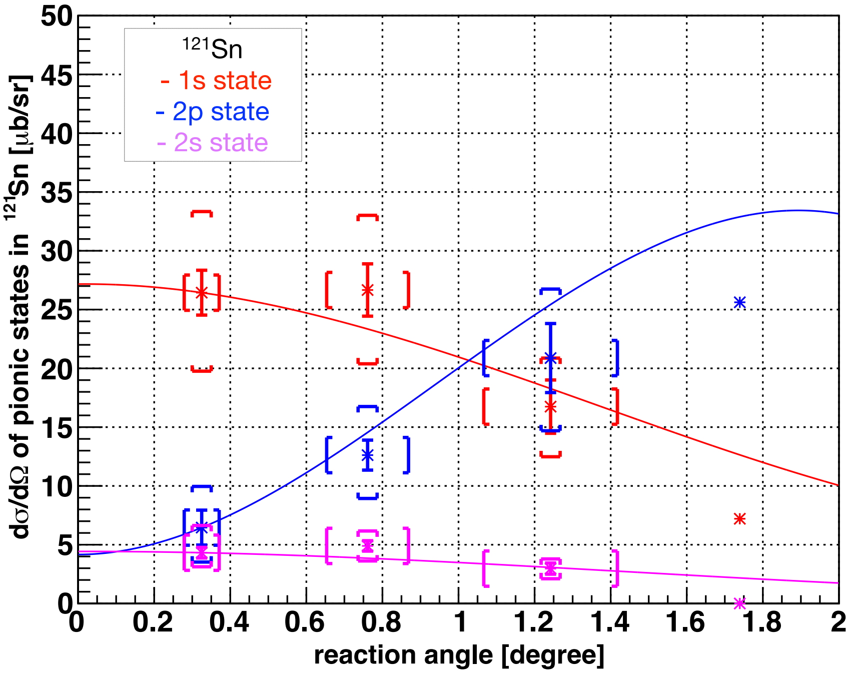

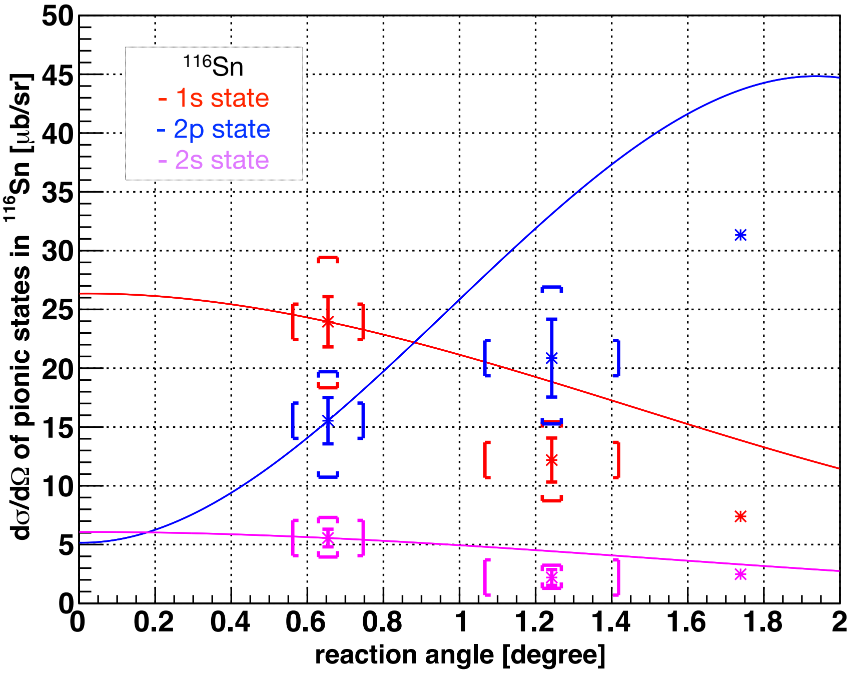

FIGURE 4.4: Reaction angle dependence of the differential formation cross sections of pionic states in ^{121}Sn (Top) and in ^{116}Sn (Bottom). The points represent the measured values in the experiment. Each line shows theoretically calculated reaction angle dependence of the pionic state formation differential cross section presented in the same color as in the experimental data. The errors independently associated with each reaction angle are shown by the error bars, and the total errors by the square brackets. The definition of these errors are written in the text.

4.3.4 Relative strength of 2p and 2s states

Relative magnitudes of the differential cross sections of the 2p and the 2s pionic states to that of the 1s state are tabulated in Table 4.9. By taking the ratio with same target and angle, the systematic errors listed in Sect. 4.3.2 can be omitted except the contribution of (iv) the uncertainties of matrix elements, which is represented as systematic errors in the table. Table 4.10 shows the same values taken from the theoretical prediction. As in the tables, the differential cross section ratio between 2s and 1s states agree with theoretical prediction within factor of 1.5. In contrast, ratio between 2p and 1s states are larger than the theoretical prediction by more than factor 5 in all angular regions in both of ^{121,116}Sn.

pionic states	$(\mathrm{d}\sigma/\mathrm{d}\Omega)_{nl}$ / $(\mathrm{d}\sigma/\mathrm{d}\Omega)_{1s}$ (Experimental values)			
$(nl)_\pi(^A\mathrm{Sn})$	$0.0° < \theta < 0.5°$	$0.5° < \theta < 1.0°$	$1.0° < \theta < 1.5°$	$1.5° < \theta < 2.0°$
$2p(^{121}\mathrm{Sn})$	$0.24 \pm 0.05(\mathrm{stat.})^{+0.08}_{-0.06}(\mathrm{sys.})$	$0.47 \pm 0.03(\mathrm{stat.})^{+0.07}_{-0.06}(\mathrm{sys.})$	$1.25 \pm 0.08(\mathrm{stat.}) \pm 0.18(\mathrm{sys.})$	$3.53 \pm 0.30(\mathrm{stat.})$
$2s(^{121}\mathrm{Sn})$	$0.16 \pm 0.02(\mathrm{stat.})^{+0.71}_{-0.01}(\mathrm{sys.})$	$0.18 \pm 0.01(\mathrm{stat.})^{+0.01}_{-0.02}(\mathrm{sys.})$	$0.18 \pm 0.02(\mathrm{stat.}) \pm 0.02(\mathrm{sys.})$	–
$2p(^{116}\mathrm{Sn})$	$0.64 \pm 0.07(\mathrm{stat.})^{+0.06}_{-0.09}(\mathrm{sys.})$		$1.66 \pm 0.21(\mathrm{stat.})^{+0.31}_{-0.28}(\mathrm{sys.})$	$4.11 \pm 0.69(\mathrm{stat.})$
$2s(^{116}\mathrm{Sn})$	$0.23 \pm 0.03(\mathrm{stat.})^{+0.05}_{-0.03}(\mathrm{sys.})$		$0.17 \pm 0.05(\mathrm{stat.})^{+0.04}_{-0.03}(\mathrm{sys.})$	$0.31 \pm 0.10(\mathrm{stat.})$

Table 4.9: Experimentally deduced relative magnitudes of the differential cross sections of 2p and 2s pionic states to that of the 1s state for each target. The errors represent statistical errors.

pionic states	$(\mathrm{d}\sigma/\mathrm{d}\Omega)_{nl}$ / $(\mathrm{d}\sigma/\mathrm{d}\Omega)_{1s}$ (Theoretical values)			
$(nl)_\pi(^A\mathrm{Sn})$	$0.0° < \theta < 0.5°$	$0.5° < \theta < 1.0°$	$1.0° < \theta < 1.5°$	$1.5° < \theta < 2.0°$
$2p(^{121}\mathrm{Sn})$	0.03	0.09	0.19	0.36
$2s(^{121}\mathrm{Sn})$	0.18	0.19	0.19	0.19
$2p(^{116}\mathrm{Sn})$	0.09		0.25	0.44
$2s(^{116}\mathrm{Sn})$	0.18		0.19	0.19

Table 4.10: Theoretically calculated relative magnitudes of the differential cross sections of 2p and 2s pionic states to that of the 1s state for each target.

4.3.5 Summary of the cross section analysis

As discussed in this section, we observe the angular dependences of the formation cross sections of pionic states in the $(d, ^3\mathrm{He})$ reaction. The angular dependences are explained by the theoretical calculations qualitatively, which proposes the assignments of the pionic states in the decomposition of the excitation spectra are correct. Meanwhile, the angular dependences of the 2p state and the cross section ratio between the 2p and 1s states show discrepancies from the theoretical predictions. These results may suggest limitations of the cross section calculation, which is based on the eikonal approximation and the effective number approach. Note that these methods are used only in the calculation of the cross section based on the independently calculated wave functions in the Klein-Gordon equation.

4.4 Deduction of optical potential parameters

In this section we study the pion-nucleus interaction based on the obtained experimental data. So far the binding energies, widths and cross sections of pionic states in ^{121,116}Sn are evaluated. We deduce optical potential parameters b_1 and ImB_0 by using the $1s$ and $2p$ binding energies ($B_{1s},\ B_{2p}$) and $1s$ width (Γ_{1s}) in ^{121}Sn.

The analysis is performed by solving the Klein-Gordon equation,

$$[-\nabla^2 + \mu^2 + 2\mu U_{\text{opt}}(r)] = [E - V_{\text{coul}}(r)]^2 \phi(\mathbf{r}), \tag{4.3}$$

where r denotes radius measured from the center of nucleus, μ the reduced mass of π and the nucleus. $U_{\text{opt}}(r)$ and $V_{\text{coul}}(r)$ denote the optical potential and finite coulomb potential for pion-nucleus interactions, respectively. To solve the equation, the nuclear density function is assumed based on the 2-parameter Fermi distribution (Sect. 4.4.1). The employed optical parameters except for b_1 and ImB_0 in the $U_{\text{opt}}(r)$ are explained in Sect. 4.4.2. In the last of the section, the b_1 and ImB_0 are evaluated from the experimental data of ^{121}Sn.

4.4.1 Nuclear density distribution

For the precise determination of s-wave potential parameters, knowledge of proton and neutron density distribution is important. In our analysis, 2-parameter Fermi distribution,

$$\rho(r) = \rho_0 \left[1 + \exp \frac{r - c}{a}\right]^{-1} \tag{4.4}$$

is adopted. Here, c is the half-density radius and a is the diffuseness parameter. The proton density parameters, a_{proton} and c_{proton} are evaluated based on the experimental data of muonic atoms [41, 42]. As in the reference, a_{proton} is fixed to be 0.523 fm. c_{proton} parameter is calculated as the averaged values of that of both side of the isotopes, because ^{121}Sn is not stable. For the neutron density function parameters, a_{neutron} and c_{neutron} are estimated as the followings. The differences between neutron matter rms radii and charge radii (Δr_{np}) in stable nuclei are determined from a x-ray spectroscopy of antiprotonic atoms [43]. In the antiproton experiment they deduced the relation between Δr_{np} and nuclear asymmetry parameter $(N - Z)/A$, as

$$\Delta r_{np} = (1.01 \pm 0.15)\frac{N - Z}{A} + (-0.04 \pm 0.03)\text{fm}. \tag{4.5}$$

From the equation and charge radii taken from the muonic atoms experiment, the neutron matter rms radii is deduced. In this thesis, we take the a_{neutron} as the averaged value of two models, "neutron skin"($a_{\mathrm{proton}} = a_{\mathrm{neutron}}$, $c_{\mathrm{proton}} \neq c_{\mathrm{neutron}}$) and "neutron halo" ($a_{\mathrm{proton}} \neq a_{\mathrm{neutron}}$, $c_{\mathrm{proton}} = c_{\mathrm{neutron}}$). In these models the unfixed one of the two parameters is chosen to reproduce the neutron matter rms radii. After taking the averaged a_{neutron}, c_{neutron} is calculated again to reproduce the neutron matter rms radii with the averaged a_{neutron}. The adopted values are summarized in Table 4.11.

c_{proton}	5.4675 [fm]
a_{proton}	0.523 [fm]
c_{neutron}	5.5676 [fm]
a_{neutron}	0.5640 [fm]

TABLE 4.11: Radial parameters of ^{121}Sn for 2-parameter Fermi distribution.

4.4.2 Optical potential parameters

Non-local part of the potential: $V_p(r)$

A non-local part of the potential in a conventional Ericson-Ericson type optical potential, $V_p(r)$ is represented as

$$V_p(r) = \frac{1}{2\mu}\nabla\cdot\left(\alpha(r)/\left[1+\frac{1}{3}\xi\alpha(r)\right]\right)\cdot\nabla \tag{4.6}$$

$$\alpha(r) = v(r)+iw(r) \tag{4.7}$$

$$v(r) = -\frac{2\pi}{m_\pi}\left[\epsilon_1^{-1}\{c_0\rho(r)+c_1\delta\rho(r)\}+\epsilon_2^{-1}\mathrm{Re}C_0\rho(r)^2\right], \tag{4.8}$$

$$w(r) = -\frac{2\pi}{m_\pi}\epsilon_2^{-1}\mathrm{Im}C_0\rho(r)^2, \tag{4.9}$$

$$\tag{4.10}$$

where ρ denotes nucleon density distributions, $\delta\rho$ density difference between neutron and proton distributions. The symbols ϵ_1 and ϵ_2 are $1 + m_\pi/M_{\mathrm{nucleon}} = 1.147$ and $m_\pi/2M_{\mathrm{nucleon}} = 1.073$, respectively. The symbol ξ represents a short range interaction correlation effects. In the following analysis, the optical parameters in non-local part are safely fixed to the result of global-fit analysis[44], because the binding energy difference of $1s$ and $2p$ is in principle insensitive to the non-local part of the potential. The fixed values are summarized in Table 4.12.

c_0	$0.261\ m_\pi^{-3}$
c_1	$0.104\ m_\pi^{-3}$
$\mathrm{Re}C_0$	$-0.25\ m_\pi^{-6}$
$\mathrm{Im}C_0$	$0.059\ m_\pi^{-6}$
ξ	0

TABLE 4.12: The parameters in non-local part of the optical potential for pion-nucleus interaction. The values are obtained from the global fit of the data of pionic atoms [44].

Local part of the potential: $U_s(r)$

The local part of the pion-nucleus interaction is represented with real part, $V_s(r)$ and imaginary part, $W_s(r)$ as the followings,

$$U_s(r) = V_s(r)+iW_s(r), \tag{4.11}$$

$$V_s(r) = -\frac{2\pi}{\mu}[\epsilon_1\{b_0\rho(r)+b_1\delta\rho(r)\}+\epsilon_2\mathrm{Re}B_0\rho(r)^2], \tag{4.12}$$

$$W_s(r) = -\frac{2\pi}{\mu}\epsilon_2\mathrm{Im}B_0\rho(r)^2, \tag{4.13}$$

The term $W_s(r)$ represents the two nucleon absorption of the π^-. In the following, we express b_0, b_1 in the conventional unit of m_π^{-1} and real and imaginary part of B_0 in m_π^{-4}. In spite that the local density dependent potential regards the b_1 as a function of density, it is pointed out that the pionic states are localized at the effective nuclear density of $0.6\rho_0$ [45], nearly independent of mass number, thus we can safely treat b_1 as a constant parameter in the following analysis.

The parameters b_0 and ReB_0 are fixed to the values obtained in the preceding experiment [17] as summarized in Table 4.13. In the preceding experiment, these parameters were evaluated from the $1s$ pionic states in light and symmetric nuclei of ^{16}O, ^{20}Ne and ^{28}Si, in which the condition $\rho_n(r) = \rho_p(r)$ is satisfied. The data of these nuclei are sensitive only to the isoscalar term. A simultaneous fitting of B_{1s} and Γ_{1s} of three Sn isotopes together with these light nuclei data is performed leaving b_0, b_1, ReB_0 and ImB_0 as the free parameters. In the fitting, the parameters in non-local part are fixed as explained above. As a result, the values summarized in the below table are obtained. In the present analysis, the values in the table are used for b_0 and ReB_0.

b_0	$-0.0233\ m_\pi^{-1}$
b_1	$-0.1149\ m_\pi^{-1}$
ReB_0	$-0.019\ m_\pi^{-4}$
ImB_0	$0.0472\ m_\pi^{-4}$

Table 4.13: The parameters in local part of the optical potential for pion-nucleus interaction. The values are obtained from the simultaneous fitting of the data of pionic atoms in Sn isotopes and light symmetric nucleus. The result is obtained from the Ref. [17].

4.4.3 Deduction of b_1 and ImB_0

We deduce b_1 and ImB_0 based on the experimentally obtained values of B_{1s} and Γ_{1s} of ^{121}Sn. The analysis based on ΔB and Γ_{1s}, and combined analysis based on B_{1s}, Γ_{1s} and ΔB are also performed, where ΔB is defined as $B_{1s} - B_{2p}$. In order to perform the analysis properly by taking into consideration the correlation between experimentally obtained values, we define likelihood as a function of the optical parameters. The likelihood is calculated as the probability that the discrepancies between the calculated values and experimental values are accounted for by the experimental errors of B_{1s}, ΔB and Γ_{1s}. The experimental errors are classified into two: "independent error" and "common error", as summarized in table 4.14. As shown, independent errors are originated in different sources for each of B_{1s}, ΔB and Γ_{1s}, without causing correlation. Meanwhile, the common errors are arising from a same source, causing strong correlation. In the calculation, Gaussian distributions are applied as the probability distribution of errors. The standard deviation of the distribution depends on the sign of the errors as shown in the table. We then calculate the likelihood for each b_1 and ImB_0 in a large area on (b_1, ImB_0) plane.

		error [keV]		main source
Independent error	B_{1s}	+22	−33	Primary beam energy, $(x_{\mathrm{F5}}\|a_{\mathrm{F5}})$ and $(x_{\mathrm{F5}}\|a^3_{\mathrm{F5}})$
	ΔB ($B_{1s} - B_{2p}$)	+8	−7	statistical error, $(x_{\mathrm{F5}}\|a^2_{\mathrm{F5}}\delta)$
	Γ_{1s}	+40	−32	multiple scattering / beam momentum spread
Common error	B_{1s}	−65	+59	$(x_{\mathrm{F5}}\|\delta)$ and $(x_{\mathrm{F5}}\|\delta^2)$
	ΔB ($B_{1s} - B_{2p}$)	+12	−8	$(x_{\mathrm{F5}}\|\delta)$ and $(x_{\mathrm{F5}}\|\delta^2)$
	Γ_{1s}	+17	−18	$(x_{\mathrm{F5}}\|\delta)$ and $(x_{\mathrm{F5}}\|\delta^2)$

Table 4.14: Errors of experimental values utilized for the deduction of b_1 and ImB_0.

Figure 4.5 shows the final result of the analysis. The ellipses correspond to "one σ" contour, where the likelihood is equal to $\exp(-\frac{1}{2}) \times$ the maximum likelihood[3]. The cross mark in each ellipse stands for the point with maximum likelihood. The left blue ellipse represents the result of the analysis with (B_{1s}, Γ_{1s}), and the right blue one with (ΔB, Γ_{1s}). The red ellipse is obtained from the analysis using B_{1s}, ΔB and Γ_{1s}. The other black three ellipses are deduced based on the binding energy and width of ^{115,119,123}Sn obtained in the experiment at GSI with the same analysis procedure. The value of b_1 in vacuum is represented as the hatched region [6–8]. The obtained b_1 and ImB_0 are summarized in Table 4.15. The errors are defined as the "one σ" contour.

---

[3] The definition is same as the preceding experiment at GSI.

As shown, the result with B_{1s} and Γ_{1s} has large uncertainty on the value of b_1, which is mainly caused by the systematic error of B_{1s}. Meanwhile, using ΔB, the value of b_1 is determined as precise as the preceding result, because of the small error of ΔB. The precision is further improved by using all of B_{1s}, ΔB and Γ_{1s} by suppressing the error contributed from the common errors. As a result, we succeed in the determination of b_1 in medium most precisely. The deduced b_1 is consistent with that in the preceding experiment, while the smaller value of ImB_0 is suggested [4]. The obtained value of b_1 indicates the partial restoration of chiral symmetry breaking in the finite density.

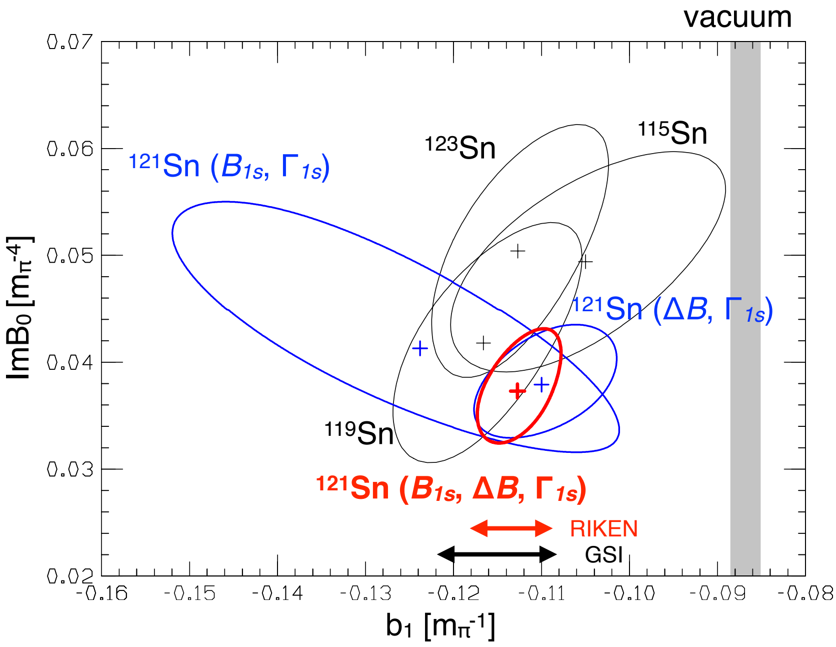

FIGURE 4.5: One σ contour plots of the fitting result of b_1 and ImB_0. The blue and red ellipses correspond to the result of this experiment, and the black ellipses correspond to the preceding experiment at GSI. The hatched region represents the b_1 in vacuum.

	b_1 $[m_\pi^{-1}]$	ImB_0 $[m_\pi^{-4}]$
this experiment (B_{1s}, Γ_{1s} in ^{121}Sn)	$-0.124\ ^{+0.0228}_{-0.0279}$	$0.0413\ ^{+0.0137}_{-0.0097}$
this experiment (ΔB, Γ_{1s} in ^{121}Sn)	$-0.110\ ^{+0.0081}_{-0.0079}$	$0.0379\ ^{+0.0055}_{-0.0050}$
this experiment (B_{1s}, ΔB, Γ_{1s} in ^{121}Sn)	$-0.114\ ^{+0.0049}_{-0.0045}$	$0.0373\ ^{+0.0057}_{-0.0048}$
experiment at GSI [17]	-0.115 ± 0.007	0.0472 ± 0.0013

TABLE 4.15: Deduced b_1 and ImB_0 in this experiment and in the preceding experiment

---

[4] The final results of the preceding experiment are obtained from simultaneous fitting of 1s pionic states in ^{16}O, ^{20}Ne and ^{28}Si in addition to Sn isotopes. The additional data of light nuclei contributed to reduce the uncertainty of ImB_0, while these data are insensitive to the isovector term.

Chapter 5

Conclusion and future outlook

5.1 Conclusion

We performed precision spectroscopy of deeply bound pionic states in ^{121,116}Sn at RIKEN, RIBF, to determine the π-nucleus isovector potential parameter b_1 precisely. As a result of the improved experimental conditions, we succeed in the most precise evaluation of b_1 in medium.

The spectra are fairly well reproduced by the theoretically calculated functions and we made fitting by altering the binding energies, widths and strengths of each pionic state. By the fitting, we obtained the binding energies and natural widths of pionic $1s$, $2p$ states in ^{121}Sn and a $1s$ state in ^{116}Sn. For the binding energies, systematic errors are dramatically reduced by using the information of two states. As a result, we obtained binding energies, natural widths, and energy differences as follows,

$$\begin{aligned}
B_{1s}(^{121}\mathrm{Sn}) &= \ +3.773 \pm 0.003(\mathrm{stat.})^{+0.063}_{-0.073}(\mathrm{sys.})[\mathrm{MeV}],\\
B_{2p}(^{121}\mathrm{Sn}) &= \ +2.225 \pm 0.004(\mathrm{stat.})^{+0.070}_{-0.085}(\mathrm{sys.})[\mathrm{MeV}],\\
B_{1s}(^{121}\mathrm{Sn}) &= \ +3.817 \pm 0.012(\mathrm{stat.})^{+0.053}_{-0.058}(\mathrm{sys.})[\mathrm{MeV}],\\
B_{1s}(^{121}\mathrm{Sn}) - B_{2p}(^{121}\mathrm{Sn}) &= \ +1.547 \pm 0.005(\mathrm{stat.})^{+0.013}_{-0.010}(\mathrm{sys.})[\mathrm{MeV}],\\
B_{2s}(^{121}\mathrm{Sn}) - B_{2p}(^{121}\mathrm{Sn}) &= \ -0.856 \pm 0.008(\mathrm{stat.})^{+0.019}_{-0.010}(\mathrm{sys.})[\mathrm{MeV}],\\
\Gamma_{1s}(^{121}\mathrm{Sn}) &= \ 0.292 \pm +0.011(\mathrm{stat.})^{+0.042}_{-0.035}(\mathrm{sys.})[\mathrm{MeV}],\\
\Gamma_{2p}(^{121}\mathrm{Sn}) &= \ 0.183 \pm +0.016(\mathrm{stat.})^{+0.048}_{-0.046}(\mathrm{sys.})[\mathrm{MeV}].
\end{aligned}$$

We also observed the angular dependence of the formation cross section of pionic states in the $(d, ^3\mathrm{He})$ reaction, and compared with the theoretical prediction based on the eikonal approximation and the effective number approach [46]. The tendency of angular dependence of the cross section is explained by the theoretical calculations qualitatively, which proposes the assignments of the pionic states performed by the decomposition of excitation spectra are correct. Meanwhile, the obtained angular dependence shows the deviations from the theoretical prediction beyond the experimental errors. We also found that the ratios of $2p$ to $1s$ in both $^{121,116}\mathrm{Sn}$ show significant discrepancies from the theoretically calculated values. These results may suggest limitations of the cross section calculation associated with the reaction dynamics.

Based on the obtained experimental data, the pion-nucleus interaction are studied. We evaluated optical potential parameters b_1 and $\mathrm{Im}B_0$ based on the above determined binding energies of $1s$ and $2p$ states, and the $1s$ width in $^{121}\mathrm{Sn}$. The deduced values are

$$b_1 = -0.114^{+0.0049}_{-0.0045}\ m_\pi^{-1} \tag{5.1}$$

$$\mathrm{Im}B_0 = 0.0373^{+0.0057}_{-0.0048}\ m_\pi^{-4}. \tag{5.2}$$

The value of b_1 is determined most precisely. The obtained value of b_1 is consistent with that in the preceding experiment at GSI, which provides a further evidence that the chiral symmetry breaking is partially restored at finite densities.

5.2 Future outlook

This experiment placed an important milestone in an experimental project to measure deeply bound pionic atoms systematically. We achieved unprecedented experimental resolution and determined the b_1 parameter most precisely. However, we expect further improvements of the experimental precision on binding energies and widths are possible. The systematic errors are dominated by the uncertainties of the transfer matrix elements, which can be determined more precisely by, i.e., increase the measurements with different scaling factors of the BigRIPS. For the widths, one of the main source of the systematic error is the position dependence of the resolution caused by the multiple scattering at F5 focal plane, and we are ready to reduce the error. With these improvement on excitation spectra, we expect that the systematic pionic atom spectroscopy at RIKEN will provide better information of b_1 to understand even the density dependence in the near future.

Acknowledgment

First I would like to express my greatest appreciation to my supervisor Prof. R. S. Hayano. He taught me the interest of the experiments of the particle physics and gave me a lot of great opportunities to study experimentally and theoretically. He also gave me a chance to join the so interesting experiment.

I also would like to show special gratitude to Prof. Masahiko Iwasaki. Thanks for him, I could concentrate the research in great environment at RIKEN. I also grateful to him for accepting me as a trainee for five years.

My deepest appreciation goes to Dr. K. Itahashi, who discovered the deeply bound pionic atoms and is the spokes person of this experiment. I spent the longest time with him from the start of the Ph.D course in Univ. of Tokyo. I learned most of the basics as a experimental physicist from the daily works with him. I also learned a lot from his sincere and enthusiastic attitude toward physics. His sharp insight in the discussion always so stimulate my curiosity.

One of my seniors S. Itoh also give me a great help in my first stage as a researcher. He developed the new optics with dispersion matching method, which was one of the key component of the experiment. His analysis of the pilot experiment was also so good reference of the analysis. I'm so grateful to him.

I would like to express special thanks to Dr. Hiroyuki Fujioka, Yoshiki K. Tanaka, Yuni N. Watanabe and Hiroki Yamakami. A lot of incisive comments from them in the analysis meeting always proceed the analysis. So important and deep indication about tracking by MWDCs comes from Yoshiki and Yuni. Yoshiki, Yuni and Hiroki also works so hard for the DAQ system and online analysis program. Without their great effort, the experiment does not become successful. I am also deeply grateful to Dr. Ken Suzuki, who works especially for F5 detectors. He also give me many valuable advice based on the experience of the previous experiment at GSI.

I'm deeply indebted to all of the members of the piAF collaborators. I am deeply grateful to the collaborators from GSI, Prof. Hans Geissel, Prof. Helmut Weick and Dr. Emma Haettner. They especially helped about the design and tuning of the ion optics.

I also would like to express my gratitude to Prof. Georg P.A. Berg, who worked hard for

tuning the beam transfer line optics and gave me a lot of valuable comments especially about dispersion matching optics.

My deep appreciation goes to the BigRIPS team. Prof. Toshimitu Kubo kindly took a lot of time for discussion with me about the optics in BigRIPS in his busy schedules. Dr. Naoto Inabe, Dr. Koichi Yoshida, Dr. Hiroyuki Takeda, Dr. Daisuke Kameda and Dr. Hiroshi Suzuki always taught me about the general information for experiments using BigRIPS, including the information of nominal detectors in BigRIPS, NMR probes, and so on. Hiroshi especially gave a lot of technical advice even after the experiment, which is so helpful to write up the thesis. They also worked to operate and tuning the BigRIPS in the experiment. Especially Hiroshi, Dr. DeukSoon Ahn and Dr. Daichi Murai worked hard even in the midnight and gave me advice during the experiment. Dr. Yoshiyuki Yanagisawa especially gave me a lot of advice about the design of the target ladder and installed the target. Dr. Kensuke Kusaka give me valuable advice about the optics from the inside of SRC to the F0 focal plane.

I would like to offer my special thanks to the collaborators from CNS group. Dr. Shinsuke Ota constructed DAQ system connecting the detectors at the F3 and the F5 focal planes. Dr. Masafumi Matsushita, Dr. Keichi Kisamori and Yu Kiyokawa operated the detectors at the F3 focal plane. These system and detectors were essential components to tune the optics of beam transfer line. Dr. Shin'ichiro Michimasa and Motonobu Takaki helped me a lot about the design and tuning the optics.

I would like to show my great appreciation to Prof. Nobuhisa Fukunishi, Prof. Naruhiko Sakamoto and all of staffs of accelerators. Without their great technique to improve the primary beam property, we could never reach the remarkable resolution.

I am deeply grateful to Prof. Kimiko Sekiguchi and other collaborators from Tohoku Univ. They prepared targets and detectors at BigDpol, which was indispensable for tuning the primary beam and optics in the beam transfer line.

I also would like to express the appreciation to Dr. Masanori Dozono, Dr. Tadashi Hashimoto, Go Mishima and Hiroshi Horii. Masanori worked especially for the tuning the primary beam properties. Tadashi improved the online analysis programs and gave me a lot of advice during and after the experiment. Go worked so energetically before and during the experiment, especially about MWDCs, nevertheless he usually works as a theorist of particle physics. Note that Go also gave so important indication about the particle identification by time over threshold of signals from MWDC with Koji Ichikawa when they joined the analysis of the pilot experiment. Hiroshi worked especially for F5 detectors hard, even it was the first experiment for him.

I owe a very important debt to Prof. Satoru Hirenzaki and Dr. Natsumi Ikeno. Without their huge amount of work about the deeply bound pionic atoms and discussion with them, the experiment could not be realized.

I would like to acknowledge Dr. Megumi Niikura for a sharp-eyed criticism for the

proposal of the experiment, which improved the proposal so much. He also gave me a lot of advice, from the nuclear structures to the attitude for writing Doctor thesis. All of the advice helped me to write up the thesis so much. I also would like to offer my special thanks to all members of Hayano Lab., Sakurai Lab. and Iwasaki Lab. Talk with Pazu circle members was almost unique time I feel relaxed. A lot of drinks presented by Pakurikon always gave me special powers. Yuki Nozawa and other members encouraged me and helped to keep positive attitude. The clerical staffs of Hayano and Iwasaki Lab., Miwa Sugawara, Yoko Fujita, Mitsue Yamamoto and Tomoko Iwanami supported my research strongly for long time. The three staffs in Iwasaki Lab. also encouraged me again and again to finish this thesis. Thank you for Kanazawa curry!!

A lot of friends also gave me power to modify my thesis during my depression. I would like to represent my appreciation especially for Hiroyasu Tajima, Sho Nakosai, Daiki Shibata, Yasukiman and Sohei. Talk on skype with Kenko Endo was precious time for me to continue writing and modifying the thesis.

I would like to add the special thanks for all of referees. Their suggestive comments helped me so much to improve this thesis, especially comments about the correlation of systematic errors.

Finally, I'm greatly appreciate my parents and grand parents, Hiroshi, Sumie, Nobukatsu and Tomoe for long-long mental and financial support, and understanding and continuous encouragement for my way as a researcher.

Appendix A

Simulation of MWDC and comb-like structures

As shown in Sec. 3.2.6, comb-like structures are observed in the reconstructed position distribution by MWDCs. In this appendix, we discuss the origin of the structures based on a simulation. As a result, we found that the singularities in close proximity to wires cause the structures.

In ref. [36], it is confirmed by a simplified simulation that the structures appear as long as the drift-time to drift-length conversion function is estimated by the method which is applied in our analysis. We also study the analysis of the tracking using a simulation. To simplify the simulation, we consider only one vertical wire with a cell from -2.5 to 2.5 mm in a plane. Input trajectories are generated with a uniform spacial distribution in $0 \leq x \leq 2.5$ mm, right side of the wire. Angles of the trajectories are set to be zero. From the horizontal position on a plane, the drift times are generated as the following equation,

$$t = 20 \text{ ns/mm} \times \ x_{\text{input}} \ + \ (\text{Gaussian resolution with } \sigma \ = \ 2.5 \text{ ns}), \tag{A.1}$$

where t and x_{input} denotes drift time and drift length, respectively. The top panel of Fig. A.1 shows the generated drift length and time. The conversion function is determined to reproduce the uniform distribution from the obtained drift time as the followings,

$$x_{\text{est}}(t) = 2.5 \times \frac{\int_{t\text{min}}^{t} \rho(t)dt}{\int_{t\text{min}}^{t\text{max}} \rho(t)dt}. \tag{A.2}$$

x_{est} represents the estimated drift length as a function of drift time t. t_{max}, t_{min} are maximum and minimum drift time. The estimated conversion function is shown as a red line in the figure. The estimated drift length by the conversion function is shown in the bottom panel of Fig. A.1, which reproduce uniform distribution as expected.

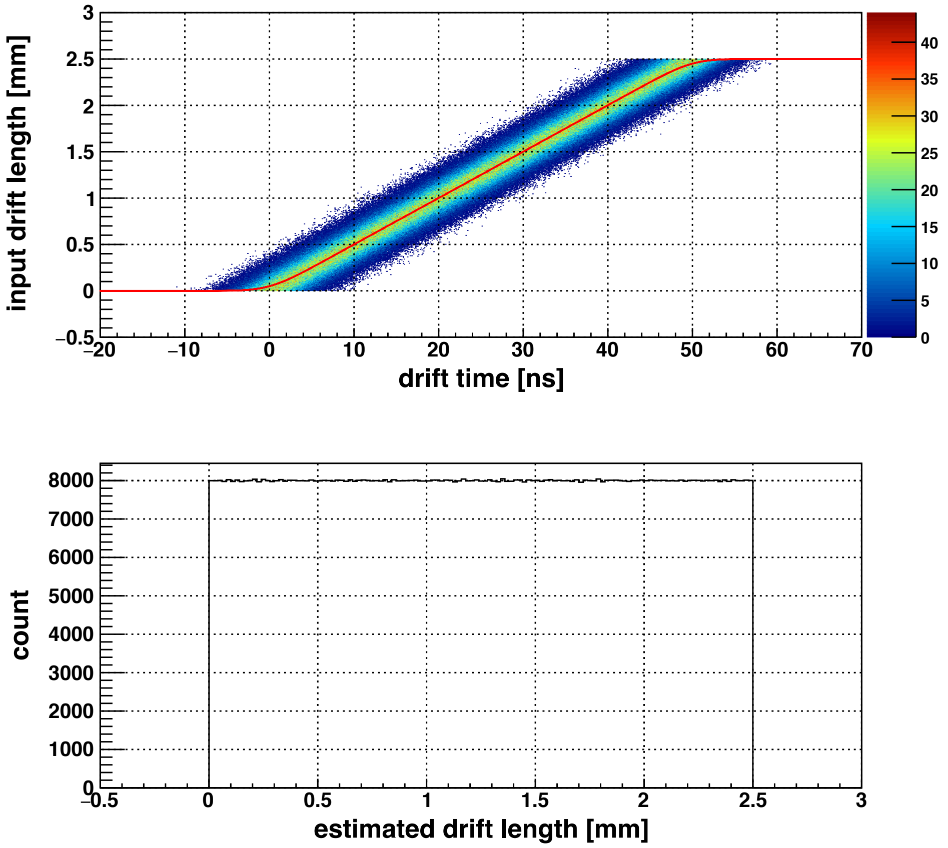

FIGURE A.1: (Top) Contour plot of generated drift time and length. The red line represents estimated conversion function.
(Bottom) Estimated drift length from the drift time and the conversion function.

To reconstruct trajectories, we prepare 10 planes with the same alignment at every 2.5 mm along beam direction. The trajectories are reconstructed from the estimated drift length on each plane. The reconstructed position is almost same with the average of estimated drift lengths, since the input angle is zero. The position distribution of reconstructed trajectory on the first plane is shown in the top panel of Fig. A.2. In the distribution, dips appear around $x = 0.0$, 2.5 mm, as seen in the experimental position distribution. The origin of the structures is asymmetric distribution of estimated drift length in these region. The bottom panel of Fig. A.2 shows the distribution of the estimated drift length in 3 regions: input drift length = 0.00 – 0.05 mm (left), 1.225 – 1.275 mm (middle) and 2.45 – 2.50 mm (right). Because the estimated drift length is defined between 0.0 to 2.5 mm, the estimated drift length fluctuates only inward around 0.0 and 2.5 mm. As a result, the reconstructed position is shifted inward around the wire and the edge of cells. This phenomenon occurs as long as the estimated drift length is limited between 0.0 to 2.5 mm. This is an explanation of why the comb structure are seen in the position distribution reconstructed by MWDCs.

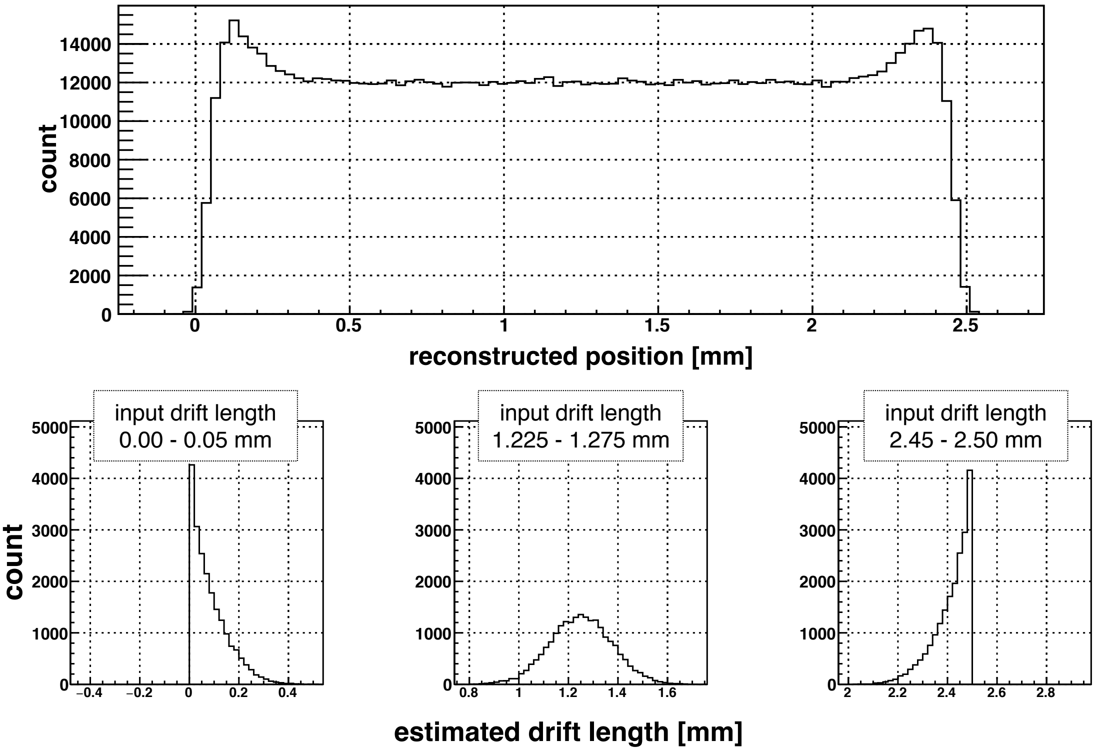

FIGURE A.2: (Top) Reconstructed position histogram on the first plane. (Bottom) Estimated drift length in 3 regions: input drift length = 0.00 – 0.05 mm (left), 1.225 – 1.275 mm (middle) and 2.45 – 2.50 mm (right).

Appendix B

Study of simulated energy resolution

In Sect. 3.7, the experimental resolution are estimated from the Monte Carlo simulation, and utilized for the subsequent analysis. In this appendix, the stability of the deduced natural widths for the angles and δ are studied to demonstrate the reliability of the estimated resolution.

(i) Angle dependence of deduced $\mathbf{\Gamma_{1s}}$

The left panel of Fig. B.1 shows the dependencies of three variables on the angular ranges of the analyzed data: the experimental resolution, deduced Γ_{1s}, and total $1s$ peak width. The analysis is performed in the angular ranges of 0 to 1°, 0 to 1.25°, 0 to 1.5° and so on. The total $1s$ peak width is calculated as root sum square of experimental resolution and Γ_{1s}, corresponding to the width of peak structure in excitation spectrum. In the figure, the statistical errors of the three values are also represented, while the errors of estimated resolutions are negligibly small. These statistical errors are correlated with each other, because the analyzed data in each angular range are not independent. The systematic errors of resolutions arising from the uncertainty of the multiple scattering and momentum spread are discussed in Sect. 3.7.5. Looking into the change of the points in the panel of Fig. B.1, one notice that the $1s$ peak widths and experimental resolution vary relatively rapidly with the analyzed range. However, the deduced Γ_{1s} stay almost constant, confirming the correctness of the angular dependent resolution estimation. The small deviation of each deduced Γ_{1s} is understood as the effect of optical aberration correction. For example, the deviation between the Γ_{1s} from the analysis in $0° < \theta < 1.5°$ and in $0° < \theta < 2.0°$ is about 7 keV. This value is smaller than the possible deviation caused by the incompleteness of the optical aberration correction of $(x_{\mathrm{F5}}|a_{\mathrm{F0}}b_{\mathrm{F0}}^2)$: $+20$ to -10, which is calculated from the difference of angular regions and Table 4.5.

(ii) δ dependence of deduced Γ_{1s}

The right panel of Fig. B.1 shows the dependencies of three variables on the angular ranges as in the left panel, with the different scaling factor of the central momenta of the BigRIPS. Comparison of the left and right panels leads to δ dependence of the deduced Γ_{1s}. The $1s$ peak widths differ largely reflecting the δ, or position dependent resolution. However, the deduced Γ_{1s} stay almost constant, and the discrepancies in different δ are within the statistical errors. It confirms the correctness of the δ dependent resolution estimation.

From the study of (i) and (ii), we can safely rely on the estimated resolution.

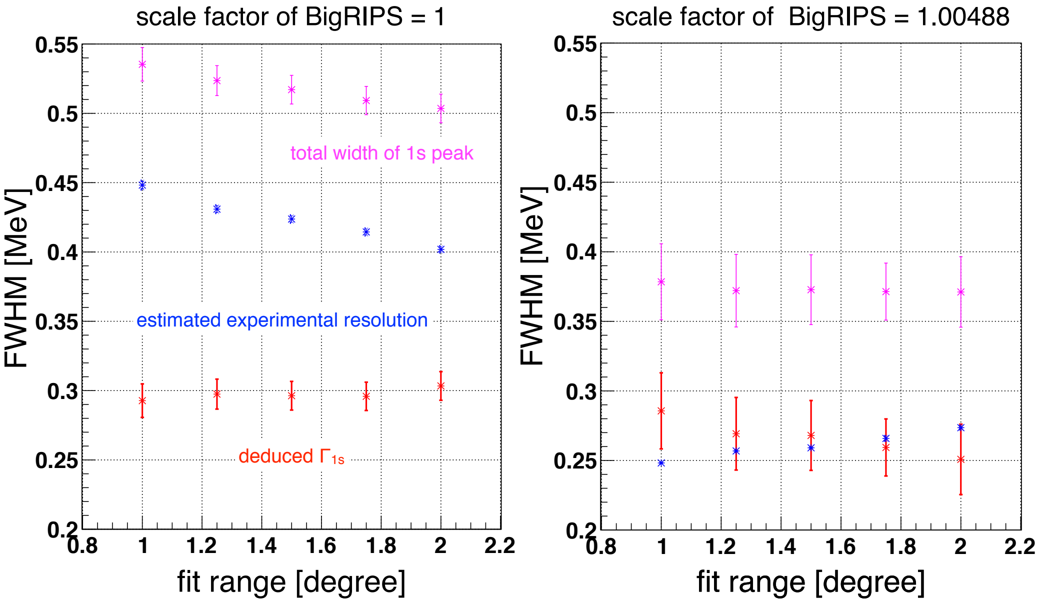

FIGURE B.1: The dependencies of three variables, total $1s$ peak width, the experimental resolution and the deduced $1s$ ntural widths, on the angular ranges of the analyzed data for two scaling factors of the central momenta of the spectrometer.

Appendix C

Parameters for decomposition

C.1 Effective number, neutron separation energy and experimental resolution of each configuration

Table C.1, C.2 shows the $N_{\text{eff}}^{(nl\otimes j_n)}$ used for the fitting to deduce the binding energies and widths in ^{121,116}Sn (Sect 4.1.2, 4.1.3)[1]. In the tables, there are several lines for one configuration. It is because the configurations of pionic state and neutron hole state of parent nucleus are not the eigenstate of the produced pionic atom. Therefore the configurations are separated into several different states with different excitation energies of daughter nucleus. $N_{\text{eff}}^{(nl\otimes j_n)}$ are calculated with a step of 0.1° [45, 46] based on the spectroscopic factors taken from the reference [39, 40]. In the analysis, the weighted average of the calculated values are used. In the tables, $\Delta S_{j_n}^{n}$, a separation energy difference of j_n neutron hole state from that of the ground state of ^{121,116}Sn, and experimental resolution are also listed. $\Delta S_{j_n}^{n}$ are taken from the reference [40, 47]. The experimental resolution is evaluated at the center of each Voigt function according to the simulation as described in Sect. 3.7.

---

[1] For ^{116}Sn, only the data of dominant configurations are listed.

configuration	N_{eff}	$\Delta S^n_{j_n}$ [MeV]	Experimental resolution (FWHM) [MeV]
$(nl)_\pi \otimes (j_n)_n^{-1}$	$0^\circ < \theta < 1.5^\circ$		
$(1s)_\pi \otimes (3s_{1/2})_n^{-1}$	4.99×10^{-2}	0.060	0.42
$(1s)_\pi \otimes (2d_{3/2})_n^{-1}$	4.03×10^{-3}	0.000	0.43
$(1s)_\pi \otimes (2d_{5/2})_n^{-1}$	5.36×10^{-3}	1.121	0.33
$(1s)_\pi \otimes (2d_{5/2})_n^{-1}$	2.92×10^{-3}	1.403	0.31
$(1s)_\pi \otimes (1g_{7/2})_n^{-1}$	8.84×10^{-5}	0.926	0.34
$(1s)_\pi \otimes (1h_{11/2})_n^{-1}$	2.03×10^{-5}	0.006	0.43
$(2p)_\pi \otimes (3s_{1/2})_n^{-1}$	8.78×10^{-4}	0.060	0.30
$(2p)_\pi \otimes (2d_{3/2})_n^{-1}$	5.09×10^{-4}	0.000	0.30
$(2p)_\pi \otimes (2d_{5/2})_n^{-1}$	4.83×10^{-4}	1.121	0.26
$(2p)_\pi \otimes (2d_{5/2})_n^{-1}$	2.53×10^{-4}	1.403	0.25
$(2p)_\pi \otimes (1g_{7/2})_n^{-1}$	6.87×10^{-5}	0.926	0.26
$(2p)_\pi \otimes (1h_{11/2})_n^{-1}$	8.87×10^{-5}	0.006	0.30
$(2s)_\pi \otimes (3s_{1/2})_n^{-1}$	9.05×10^{-3}	0.060	0.26
$(2s)_\pi \otimes (2d_{3/2})_n^{-1}$	7.47×10^{-4}	0.000	0.26
$(2s)_\pi \otimes (2d_{5/2})_n^{-1}$	1.02×10^{-3}	1.121	0.26
$(2s)_\pi \otimes (2d_{5/2})_n^{-1}$	5.54×10^{-4}	1.403	0.27
$(2s)_\pi \otimes (1g_{7/2})_n^{-1}$	1.77×10^{-5}	0.926	0.26
$(2s)_\pi \otimes (1h_{11/2})_n^{-1}$	2.82×10^{-6}	0.006	0.26
$(3p)_\pi \otimes (3s_{1/2})_n^{-1}$	1.91×10^{-4}	0.060	0.25
$(3p)_\pi \otimes (2d_{3/2})_n^{-1}$	1.13×10^{-4}	0.000	0.26
$(3p)_\pi \otimes (2d_{5/2})_n^{-1}$	1.14×10^{-4}	1.121	0.28
$(3p)_\pi \otimes (2d_{5/2})_n^{-1}$	6.03×10^{-5}	1.403	0.29
$(3p)_\pi \otimes (1g_{7/2})_n^{-1}$	1.72×10^{-5}	0.926	0.27
$(3p)_\pi \otimes (1h_{11/2})_n^{-1}$	2.69×10^{-5}	0.006	0.26
$(3s)_\pi \otimes (3s_{1/2})_n^{-1}$	3.15×10^{-3}	0.060	0.26
$(3s)_\pi \otimes (2d_{3/2})_n^{-1}$	2.63×10^{-4}	0.000	0.26
$(3s)_\pi \otimes (2d_{5/2})_n^{-1}$	3.60×10^{-4}	1.121	0.29
$(3s)_\pi \otimes (2d_{5/2})_n^{-1}$	1.96×10^{-4}	1.403	0.31
$(3s)_\pi \otimes (1g_{7/2})_n^{-1}$	6.48×10^{-6}	0.926	0.28
$(3s)_\pi \otimes (1h_{11/2})_n^{-1}$	9.31×10^{-7}	0.006	0.26

TABLE C.1: Effective number, neutron separation energy and experimental resolution of each configuration in ^{121}Sn.

configuration	N_{eff}	$\Delta S^n_{j_n}$ [MeV]	Experimental resolution (FWHM) [MeV]
$(nl)_\pi \otimes (j_n)_n^{-1}$	$0^\circ < \theta < 1.5^\circ$		
$(1s)_\pi \otimes (3s_{1/2})_n^{-1}$	8.88×10^{-3}	0.000	0.52
$(1s)_\pi \otimes (3s_{1/2})_n^{-1}$	1.74×10^{-3}	1.757	0.38
$(1s)_\pi \otimes (3s_{1/2})_n^{-1}$	1.46×10^{-3}	2.027	0.36
$(1s)_\pi \otimes (3s_{1/2})_n^{-1}$	1.18×10^{-3}	2.545	0.33
$(1s)_\pi \otimes (2d_{3/2})_n^{-1}$	1.18×10^{-3}	2.587	0.33
$(1s)_\pi \otimes (2d_{5/2})_n^{-1}$	1.38×10^{-3}	3.709	0.30
$(2p)_\pi \otimes (3s_{1/2})_n^{-1}$	6.12×10^{-4}	0.000	0.39
$(2p)_\pi \otimes (3s_{1/2})_n^{-1}$	1.06×10^{-4}	1.757	0.30
$(2p)_\pi \otimes (3s_{1/2})_n^{-1}$	8.70×10^{-5}	2.027	0.30
$(2p)_\pi \otimes (3s_{1/2})_n^{-1}$	6.81×10^{-5}	2.545	0.29
$(2p)_\pi \otimes (2d_{3/2})_n^{-1}$	4.15×10^{-4}	2.587	0.29
$(2p)_\pi \otimes (2d_{3/2})_n^{-1}$	6.79×10^{-5}	2.225	0.29
$(2p)_\pi \otimes (2d_{3/2})_n^{-1}$	6.53×10^{-5}	3.228	0.30
$(2p)_\pi \otimes (2d_{3/2})_n^{-1}$	6.49×10^{-5}	3.371	0.30
$(2p)_\pi \otimes (2d_{3/2})_n^{-1}$	7.28×10^{-5}	3.470	0.31
$(2p)_\pi \otimes (2d_{3/2})_n^{-1}$	9.95×10^{-5}	3.589	0.31
$(2p)_\pi \otimes (2d_{3/2})_n^{-1}$	1.01×10^{-4}	3.772	0.32
$(2p)_\pi \otimes (2d_{3/2})_n^{-1}$	9.02×10^{-5}	3.950	0.32
$(2p)_\pi \otimes (2d_{5/2})_n^{-1}$	2.57×10^{-4}	3.416	0.30
$(2p)_\pi \otimes (2d_{5/2})_n^{-1}$	4.05×10^{-4}	3.709	0.31
$(2p)_\pi \otimes (2d_{5/2})_n^{-1}$	6.78×10^{-5}	3.589	0.31
$(2p)_\pi \otimes (2d_{5/2})_n^{-1}$	6.74×10^{-5}	3.772	0.32
$(2p)_\pi \otimes (2d_{5/2})_n^{-1}$	6.48×10^{-5}	3.950	0.32
$(2p)_\pi \otimes (1g_{7/2})_n^{-1}$	8.62×10^{-5}	3.096	0.30
$(2s)_\pi \otimes (3s_{1/2})_n^{-1}$	1.63×10^{-3}	0.000	0.34
$(2s)_\pi \otimes (3s_{1/2})_n^{-1}$	3.14×10^{-4}	1.757	0.29
$(2s)_\pi \otimes (3s_{1/2})_n^{-1}$	2.62×10^{-4}	2.027	0.29
$(2s)_\pi \otimes (3s_{1/2})_n^{-1}$	2.11×10^{-4}	2.545	0.30
$(2s)_\pi \otimes (2d_{3/2})_n^{-1}$	2.10×10^{-4}	2.587	0.31
$(2s)_\pi \otimes (2d_{5/2})_n^{-1}$	2.53×10^{-4}	3.709	0.37
$(3p)_\pi \otimes (3s_{1/2})_n^{-1}$	1.57×10^{-4}	0.000	0.32
$(3p)_\pi \otimes (3s_{1/2})_n^{-1}$	2.73×10^{-5}	1.757	0.30
$(3p)_\pi \otimes (3s_{1/2})_n^{-1}$	2.26×10^{-5}	2.027	0.30
$(3p)_\pi \otimes (3s_{1/2})_n^{-1}$	1.77×10^{-5}	2.545	0.32
$(3p)_\pi \otimes (2d_{3/2})_n^{-1}$	1.10×10^{-4}	2.587	0.32
$(3p)_\pi \otimes (2d_{3/2})_n^{-1}$	1.80×10^{-5}	2.225	0.31
$(3p)_\pi \otimes (2d_{3/2})_n^{-1}$	1.74×10^{-5}	3.228	0.35
$(3p)_\pi \otimes (2d_{3/2})_n^{-1}$	1.74×10^{-5}	3.371	0.37
$(3p)_\pi \otimes (2d_{3/2})_n^{-1}$	1.95×10^{-5}	3.470	0.37
$(3p)_\pi \otimes (2d_{3/2})_n^{-1}$	2.67×10^{-5}	3.589	0.38
$(3p)_\pi \otimes (2d_{3/2})_n^{-1}$	2.73×10^{-5}	3.772	0.40
$(3p)_\pi \otimes (2d_{3/2})_n^{-1}$	2.43×10^{-5}	3.950	0.42
$(3p)_\pi \otimes (2d_{5/2})_n^{-1}$	7.00×10^{-5}	3.416	0.37
$(3p)_\pi \otimes (2d_{5/2})_n^{-1}$	1.11×10^{-4}	3.709	0.39
$(3p)_\pi \otimes (2d_{5/2})_n^{-1}$	1.85×10^{-5}	3.589	0.38
$(3p)_\pi \otimes (2d_{5/2})_n^{-1}$	1.85×10^{-5}	3.772	0.40
$(3p)_\pi \otimes (2d_{5/2})_n^{-1}$	1.78×10^{-5}	3.950	0.42
$(3p)_\pi \otimes (1g_{7/2})_n^{-1}$	1.68×10^{-5}	3.180	0.35
$(3p)_\pi \otimes (1g_{7/2})_n^{-1}$	2.43×10^{-5}	3.096	0.35
$(3s)_\pi \otimes (3s_{1/2})_n^{-1}$	5.69×10^{-4}	0.000	0.31
$(3s)_\pi \otimes (3s_{1/2})_n^{-1}$	1.09×10^{-4}	1.757	0.30
$(3s)_\pi \otimes (3s_{1/2})_n^{-1}$	9.10×10^{-5}	2.027	0.31
$(3s)_\pi \otimes (3s_{1/2})_n^{-1}$	7.31×10^{-5}	2.545	0.33
$(3s)_\pi \otimes (2d_{3/2})_n^{-1}$	7.31×10^{-5}	2.587	0.33
$(3s)_\pi \otimes (2d_{5/2})_n^{-1}$	8.84×10^{-5}	3.709	0.42

TABLE C.2: Effective number, neutron separation energy and experimental resolution of each configuration in ^{116}Sn.

C.2 Effective numbers of finite angles

Table C.3, C.4 shows the $N_{\mathrm{eff}}^{(nl\otimes j_n)}$ in each reaction angle calculated based on the existing experimental results of the relative strength of the $^{122,117}\mathrm{Sn}(d,t)$ reaction cross sections [39, 40].

configuration	N_{eff}			
$(nl)_\pi \otimes (j_n)_n^{-1}$	$0° < \theta < 0.5°$	$0.5° < \theta < 1.0°$	$1.0° < \theta < 1.5°$	$1.5° < \theta < 2.0°$
$(1s)_\pi \otimes (3s_{1/2})_n^{-1}$	4.99×10^{-2}	4.35×10^{-2}	3.46×10^{-2}	2.25×10^{-2}
$(1s)_\pi \otimes (2d_{3/2})_n^{-1}$	4.03×10^{-3}	4.02×10^{-3}	3.95×10^{-3}	3.66×10^{-3}
$(1s)_\pi \otimes (2d_{5/2})_n^{-1}$	5.36×10^{-3}	5.31×10^{-3}	5.18×10^{-3}	4.79×10^{-3}
$(1s)_\pi \otimes (2d_{5/2})_n^{-1}$	2.92×10^{-3}	2.90×10^{-3}	2.83×10^{-3}	2.61×10^{-3}
$(1s)_\pi \otimes (1g_{7/2})_n^{-1}$	8.84×10^{-5}	1.27×10^{-4}	1.94×10^{-4}	3.21×10^{-4}
$(1s)_\pi \otimes (1h_{11/2})_n^{-1}$	2.03×10^{-5}	4.77×10^{-5}	1.03×10^{-4}	2.29×10^{-4}
$(2p)_\pi \otimes (3s_{1/2})_n^{-1}$	8.78×10^{-4}	1.88×10^{-3}	3.01×10^{-3}	3.80×10^{-3}
$(2p)_\pi \otimes (2d_{3/2})_n^{-1}$	5.09×10^{-4}	1.11×10^{-3}	1.86×10^{-3}	2.58×10^{-3}
$(2p)_\pi \otimes (2d_{5/2})_n^{-1}$	4.83×10^{-4}	1.17×10^{-3}	2.06×10^{-3}	2.98×10^{-3}
$(2p)_\pi \otimes (2d_{5/2})_n^{-1}$	2.53×10^{-4}	6.29×10^{-4}	1.12×10^{-3}	1.62×10^{-3}
$(2p)_\pi \otimes (1g_{7/2})_n^{-1}$	6.87×10^{-5}	1.61×10^{-4}	2.98×10^{-4}	4.90×10^{-4}
$(2p)_\pi \otimes (1h_{11/2})_n^{-1}$	8.87×10^{-5}	1.34×10^{-4}	2.19×10^{-4}	3.93×10^{-4}
$(2s)_\pi \otimes (3s_{1/2})_n^{-1}$	9.05×10^{-3}	8.01×10^{-3}	6.50×10^{-3}	4.40×10^{-3}
$(2s)_\pi \otimes (2d_{3/2})_n^{-1}$	7.47×10^{-4}	7.39×10^{-4}	7.21×10^{-4}	6.67×10^{-4}
$(2s)_\pi \otimes (2d_{5/2})_n^{-1}$	1.02×10^{-3}	1.00×10^{-3}	9.71×10^{-4}	8.94×10^{-4}
$(2s)_\pi \otimes (2d_{5/2})_n^{-1}$	5.54×10^{-4}	5.46×10^{-4}	5.29×10^{-4}	4.88×10^{-4}
$(2s)_\pi \otimes (1g_{7/2})_n^{-1}$	1.77×10^{-5}	2.46×10^{-5}	3.67×10^{-5}	5.90×10^{-5}
$(2s)_\pi \otimes (1h_{11/2})_n^{-1}$	2.82×10^{-6}	8.26×10^{-6}	1.88×10^{-5}	4.19×10^{-5}
$(3p)_\pi \otimes (3s_{1/2})_n^{-1}$	1.91×10^{-4}	4.72×10^{-4}	7.99×10^{-4}	1.05×10^{-3}
$(3p)_\pi \otimes (2d_{3/2})_n^{-1}$	1.13×10^{-4}	2.84×10^{-4}	5.01×10^{-4}	7.20×10^{-4}
$(3p)_\pi \otimes (2d_{5/2})_n^{-1}$	1.14×10^{-4}	3.11×10^{-4}	5.69×10^{-4}	8.45×10^{-4}
$(3p)_\pi \otimes (2d_{5/2})_n^{-1}$	6.03×10^{-5}	1.68×10^{-4}	3.09×10^{-4}	4.60×10^{-4}
$(3p)_\pi \otimes (1g_{7/2})_n^{-1}$	1.72×10^{-5}	4.45×10^{-5}	8.49×10^{-5}	1.42×10^{-4}
$(3p)_\pi \otimes (1h_{11/2})_n^{-1}$	2.69×10^{-5}	4.00×10^{-5}	6.45×10^{-5}	1.15×10^{-4}
$(3s)_\pi \otimes (3s_{1/2})_n^{-1}$	3.15×10^{-3}	2.80×10^{-3}	2.29×10^{-3}	1.56×10^{-3}
$(3s)_\pi \otimes (2d_{3/2})_n^{-1}$	2.63×10^{-4}	2.60×10^{-4}	2.53×10^{-4}	2.34×10^{-4}
$(3s)_\pi \otimes (2d_{5/2})_n^{-1}$	3.60×10^{-4}	3.55×10^{-4}	3.43×10^{-4}	3.15×10^{-4}
$(3s)_\pi \otimes (2d_{5/2})_n^{-1}$	1.96×10^{-4}	1.93×10^{-4}	1.87×10^{-4}	1.72×10^{-4}
$(3s)_\pi \otimes (1g_{7/2})_n^{-1}$	6.48×10^{-6}	8.91×10^{-6}	1.31×10^{-5}	2.09×10^{-5}
$(3s)_\pi \otimes (1h_{11/2})_n^{-1}$	9.31×10^{-7}	2.90×10^{-6}	6.67×10^{-6}	1.48×10^{-5}

TABLE C.3: Effective number of each reaction angle and each configuration in ^{121}Sn.

configuration		N_{eff}	
$(nl)_\pi \otimes (j_n)_n^{-1}$	$0^\circ < \theta < 1.0^\circ$	$1.0^\circ < \theta < 1.5^\circ$	$1.5^\circ < \theta < 2.0^\circ$
$(1s)_\pi \otimes (3s_{1/2})_n^{-1}$	1.03×10^{-2}	7.93×10^{-3}	5.22×10^{-3}
$(1s)_\pi \otimes (3s_{1/2})_n^{-1}$	2.01×10^{-3}	1.55×10^{-3}	1.02×10^{-3}
$(1s)_\pi \otimes (3s_{1/2})_n^{-1}$	1.68×10^{-3}	1.30×10^{-3}	8.57×10^{-4}
$(1s)_\pi \otimes (3s_{1/2})_n^{-1}$	1.36×10^{-3}	1.05×10^{-3}	6.93×10^{-4}
$(1s)_\pi \otimes (2d_{3/2})_n^{-1}$	1.19×10^{-3}	1.17×10^{-3}	1.09×10^{-3}
$(1s)_\pi \otimes (2d_{5/2})_n^{-1}$	1.40×10^{-3}	1.37×10^{-3}	1.27×10^{-3}
$(2p)_\pi \otimes (3s_{1/2})_n^{-1}$	4.48×10^{-4}	7.37×10^{-4}	9.01×10^{-4}
$(2p)_\pi \otimes (3s_{1/2})_n^{-1}$	7.20×10^{-5}	1.31×10^{-4}	1.67×10^{-4}
$(2p)_\pi \otimes (3s_{1/2})_n^{-1}$	5.87×10^{-5}	1.08×10^{-4}	1.39×10^{-4}
$(2p)_\pi \otimes (3s_{1/2})_n^{-1}$	4.50×10^{-5}	8.55×10^{-5}	1.10×10^{-4}
$(2p)_\pi \otimes (2d_{3/2})_n^{-1}$	2.63×10^{-4}	5.25×10^{-4}	7.44×10^{-4}
$(2p)_\pi \otimes (2d_{3/2})_n^{-1}$	6.09×10^{-5}	1.27×10^{-4}	1.83×10^{-4}
$(2p)_\pi \otimes (2d_{3/2})_n^{-1}$	6.17×10^{-5}	1.30×10^{-4}	1.88×10^{-4}
$(2p)_\pi \otimes (2d_{3/2})_n^{-1}$	5.46×10^{-5}	1.16×10^{-4}	1.68×10^{-4}
$(2p)_\pi \otimes (2d_{5/2})_n^{-1}$	1.57×10^{-4}	3.27×10^{-4}	4.80×10^{-4}
$(2p)_\pi \otimes (2d_{5/2})_n^{-1}$	2.47×10^{-4}	5.19×10^{-4}	7.63×10^{-4}
$(2p)_\pi \otimes (1g_{7/2})_n^{-1}$	5.09×10^{-5}	1.10×10^{-4}	1.83×10^{-4}
$(2s)_\pi \otimes (3s_{1/2})_n^{-1}$	1.86×10^{-3}	1.48×10^{-3}	1.01×10^{-3}
$(2s)_\pi \otimes (3s_{1/2})_n^{-1}$	3.58×10^{-4}	2.84×10^{-4}	1.94×10^{-4}
$(2s)_\pi \otimes (3s_{1/2})_n^{-1}$	2.99×10^{-4}	2.37×10^{-4}	1.62×10^{-4}
$(2s)_\pi \otimes (3s_{1/2})_n^{-1}$	2.41×10^{-4}	1.91×10^{-4}	1.31×10^{-4}
$(2s)_\pi \otimes (2d_{3/2})_n^{-1}$	2.14×10^{-4}	2.08×10^{-4}	1.93×10^{-4}
$(2s)_\pi \otimes (2d_{5/2})_n^{-1}$	2.58×10^{-4}	2.49×10^{-4}	2.30×10^{-4}
$(3p)_\pi \otimes (3s_{1/2})_n^{-1}$	1.08×10^{-4}	1.93×10^{-4}	2.48×10^{-4}
$(3p)_\pi \otimes (3s_{1/2})_n^{-1}$	1.76×10^{-5}	3.46×10^{-5}	4.58×10^{-5}
$(3p)_\pi \otimes (3s_{1/2})_n^{-1}$	1.44×10^{-5}	2.86×10^{-5}	3.81×10^{-5}
$(3p)_\pi \otimes (3s_{1/2})_n^{-1}$	1.12×10^{-5}	2.26×10^{-5}	3.04×10^{-5}
$(3p)_\pi \otimes (2d_{3/2})_n^{-1}$	6.66×10^{-5}	1.41×10^{-4}	2.07×10^{-4}
$(3p)_\pi \otimes (2d_{3/2})_n^{-1}$	1.10×10^{-5}	2.30×10^{-5}	3.34×10^{-5}
$(3p)_\pi \otimes (2d_{3/2})_n^{-1}$	1.15×10^{-5}	2.52×10^{-5}	3.72×10^{-5}
$(3p)_\pi \otimes (2d_{3/2})_n^{-1}$	1.57×10^{-5}	3.45×10^{-5}	5.10×10^{-5}
$(3p)_\pi \otimes (2d_{3/2})_n^{-1}$	1.60×10^{-5}	3.53×10^{-5}	5.23×10^{-5}
$(3p)_\pi \otimes (2d_{3/2})_n^{-1}$	1.42×10^{-5}	3.15×10^{-5}	4.67×10^{-5}
$(3p)_\pi \otimes (2d_{5/2})_n^{-1}$	4.14×10^{-5}	9.02×10^{-5}	1.35×10^{-4}
$(3p)_\pi \otimes (2d_{5/2})_n^{-1}$	6.53×10^{-5}	1.43×10^{-4}	2.16×10^{-4}
$(3p)_\pi \otimes (2d_{5/2})_n^{-1}$	1.09×10^{-5}	2.39×10^{-5}	3.59×10^{-5}
$(3p)_\pi \otimes (2d_{5/2})_n^{-1}$	1.09×10^{-5}	2.39×10^{-5}	3.59×10^{-5}
$(3p)_\pi \otimes (1g_{7/2})_n^{-1}$	1.39×10^{-5}	3.13×10^{-5}	5.27×10^{-5}
$(3s)_\pi \otimes (3s_{1/2})_n^{-1}$	6.47×10^{-4}	5.17×10^{-4}	3.57×10^{-4}
$(3s)_\pi \otimes (3s_{1/2})_n^{-1}$	1.24×10^{-4}	9.89×10^{-5}	6.83×10^{-5}
$(3s)_\pi \otimes (3s_{1/2})_n^{-1}$	1.03×10^{-4}	8.26×10^{-5}	5.71×10^{-5}
$(3s)_\pi \otimes (3s_{1/2})_n^{-1}$	8.30×10^{-5}	6.63×10^{-5}	4.59×10^{-5}
$(3s)_\pi \otimes (2d_{3/2})_n^{-1}$	7.45×10^{-5}	7.23×10^{-5}	6.70×10^{-5}
$(3s)_\pi \otimes (2d_{5/2})_n^{-1}$	9.04×10^{-5}	8.73×10^{-5}	8.04×10^{-5}

TABLE C.4: Effective number of each reaction angle and each configuration in ^{116}Sn.

Bibliography

[1] U. Vogl and W. Weise, Prog. Part. Nucl. Phys. **27**, 195 (1991).

[2] T. Hatsuda and T. Kunihiro, Phys. Rep. **247** (1994).

[3] E. Kolomeitsev, N. Kaiser, and W. Weise, Phys. Rev. Lett. **90**, 9 (2003).

[4] D. Jido, T. Hatsuda, and T. Kunihiro, Phys. Lett. B **670**, 109 (2008).

[5] N. Ikeno *et al.*, Prog. Theor. Phys. **126**, 483 (2011).

[6] H.-C. Schröder *et al.*, Phys. Lett. B **469**, 25 (1999).

[7] H.-C. Schröder *et al.*, Eur. Phys. J. C **21**, 473 (2001).

[8] D. Gotta *et al.*, Lecture Notes in Physics **745**, 165 (2008).

[9] E. Friedman and G. Soff, J. Phys. G **11**, L37 (1985).

[10] H. Toki and T. Yamazaki, Phys. Lett. B **213**, 129 (1988).

[11] N. Ikeno, H. Nagahiro, and S. Hirenzaki, Eur. Phys. J. A **47**, 161 (2011).

[12] T. Yamazaki *et al.*, Z. Phys. A **355**, 219 (1996).

[13] H. Gilg *et al.*, Phys. Rev. C **62**, 025201 (2000).

[14] K. Itahashi *et al.*, Phys. Rev. C **62**, 025202 (2000).

[15] H. Geissel *et al.*, Phys. Lett. B **549**, 64 (2002).

[16] H. Geissel *et al.*, Phys. Rev. Lett. **88**, 122301 (2002).

[17] K. Suzuki *et al.*, Phys. Rev. Lett. **92**, 072302 (2004).

[18] K. Itahashi *et al.*, RIBF proposal **NP0802**, RIBF54 (2008).

[19] S. Itoh, Doctoral Dissertation, Univ. of Tokyo (2011).

[20] N. Ikeno *et al.*, Prog. Theor. Exp. Phys. **2013**, 63D01 (2013).

[21] R. Seki and K. Masutani, Phys. Rev. C **27**, 2799 (1983).

[22] Y. Yano, Nucl. Inst. Meth. B **261**, 1009 (2007).

[23] "RIBF User Guide" on web page, http://www.nishina.riken.jp/RIBF.

[24] T. Kubo, Nucl. Instr. and Meth. B **204**, 97 (2003).

[25] S. A. Martin *et al.*, Nucl. Instr. and Meth. B **214**, 281 (1983).

[26] T. Wakasa *et al.*, Nucl. Instr. and Meth. B **482**, 79 (2002).

[27] H. Fujita, Y. Fujita, and G. Berg, Nucl. Inst. and Meth. B **484**, 17 (2002).

[28] T. Nishi *et al.*, Nucl. Instr. and Meth. B **317**, 290 (2013).

[29] K. Makino and M. Berz, Nucl. Instr. and Meth. A **558**, 346 (2006).

[30] "COSY INFINITY" on web page, http://bt.pa.msu.edu/index.htm.

[31] H. Miya *et al.*, Nucl. Instr. and Meth. B **317**, 701 (2013).

[32] S. Osamu, ATLAS Internal Note "Amplifier-Shaper-Discriminator ICs and ASD Boads" on web page. http://www.gn-d.com/guest/asdprr.pdf.

[33] Y. Arai *et al.*, Nuclear Science, IEEE Transactions on **49**, 1164 (2002).

[34] H. Baba *et al.*, Nucl. Instr. and Meth. A **616**, 65 (2010).

[35] R. Carnegie *et al.*, Nucl. Instr. and Meth. A **538**, 372 (2005).

[36] T. Tanaka, Doctoral Dissertation, Univ. of Tokyo (2015), Appendix.

[37] "GICOSY" on web page, https://web-docs.gsi.de/ weick/gicosy/.

[38] N. Iwasa *et al.*, Nucl. Instr. Meth. B **126**, 284 (1997).

[39] E. J. Schneid, A. Prakash, and B. L. Cohen, Phys. Rev. **156**, 1316 (1967).

[40] J. Schippers *et al.*, Nuclear Physics A **510**, 70 (1990).

[41] G. Fricke *et al.*, At. Data Nucl. Data Tables **60**, 177 (1995).

[42] C. Piller *et al.*, Phys. Rev. C **42**, 182 (1990).

[43] A. Trzcińska *et al.*, Phys. Rev. Lett. **87**, 1 (2001).

[44] C. Batty, E. Friedman, and A. Gal, Phys. Rep. **287**, 385 (1997).

[45] N. Ikeno, Doctoral Dissertation, Nara Women's Univ. (2014).

[46] N. Ikeno, private comminucation.

[47] S. Ohya, Nucl. Data Sheets **111**, 1619 (2010).